ABSTRACT

Title of Dissertation:	PLASMA-PHOTORESIST INTERACTIONS FOR REALIZING ADVANCED PATTERN TRANSFER PROCESSES
	Adam Pranda, Doctor of Philosophy, 2020
Dissertation directed by:	Professor Gottlieb S. Oehrlein, Department of Materials Science and Engineering and Institute for Research in Electronics and Applied Physics

Photoresist (PR) materials undergo significant physical and chemical modification from the ions, vacuum ultraviolet (VUV) photons, and reactive species that comprise a plasma etch process. The modifications of these materials, which are an integral component in the manufacturing process of semiconductor devices, has key implications on the control of the etching and roughening behaviors that are vital for establishing selective pattern transfer processes that maintain feature fidelity at increasingly smaller feature sizes and pitches. In the initial chapters of this dissertation, we focus on establishing a fundamental understanding of the relationship between PR modification and the resulting etching behavior under an inert argon plasma process. To establish the key relationships, we utilize a combination of *in situ* ellipsometry supported by x-ray photoelectron spectroscopy (XPS) and attenuated total reflection Fourier transform infrared (ATR-FTIR) spectroscopy to develop an

ellipsometric model that interprets the correlation between the PR layer structure, which develops due to energetic ion bombardment in a plasma process, and the corresponding etching behavior. From this analysis, we find that energetic ion bombardment produces a dense amorphous carbon (DAC) layer on the PR surface that reduces the overall PR etch rate with increasing thickness. Secondary characterization via atomic force microscopy (AFM) also shows corresponding development of surface roughness. Expanding the scope to reactive plasma chemistries containing fluorocarbon (FC) species, we find that the FC species interact with the DAC layer to produce an FC-rich modified layer on the surface. In the latter part of this dissertation, we apply our findings regarding the PR surface modification to address an industrial need to improve the etch selectivity of silicon dioxide (SiO_2) to PR by minimizing the thickness loss of an extreme ultraviolet (EUV) PR under an atomic layer etching (ALE) process by systematically evaluating the ALE processing parameters. We find that cyclic ion bombardment of a deposited FC layer leads to the development of a modified layer that significantly reduces PR loss while simultaneously maintaining SiO_2 etching, thus producing a high SiO_2/PR etching selectivity. Lastly, we examine another industrial challenge concerning the extent of off-normal ions affecting the etching uniformity of PR samples.

PLASMA-PHOTORESIST INTERACTIONS FOR REALIZING ADVANCED PATTERN TRANSFER PROCESSES

by

Adam Pranda

Dissertation submitted to the Faculty of the Graduate School of the
University of Maryland, College Park, in partial fulfillment
of the requirements for the degree of
Doctor of Philosophy
2020

Advisory Committee:
Prof. Gottlieb S. Oehrlein, Department of Materials Science and Engineering, Chair
Prof. Robert M. Briber, Department of Materials Science and Engineering
Prof. Raymond J. Phaneuf, Department of Materials Science and Engineering
Dr. Sebastian Engelmann, IBM
Prof. John T. Fourkas, Department of Chemistry and Biochemistry

Dedication

I would like to dedicate this work to my family whose unwavering love and support has enabled me to pursue my personal and academic aspirations.

Acknowledgements

There are numerous individuals who I am immensely grateful for their contributions towards the success of my PhD research. First, I would like to thank my advisor Prof. Gottlieb Oehrlein, who reached out to me and gave me this opportunity to be in his research group when I did not have a clear direction in my graduate studies. Through his years of mentorship, I have learned the immeasurable value of structured and responsible research that is meaningful to the wider scientific community. I could have scarcely imagined that I would one day be presenting my work at numerous conferences with the interest and appreciation of some of the leading companies in the field. It has been a great privilege for me to have Prof. Oehrlein as my advisor, and I will always strive to uphold the personal and professional values that he instilled in me that have helped me to be successful.

I would like to thank my dissertation committee, Prof. Briber, Prof. Phaneuf, Prof. Fourkas, and Dr. Engelmann for their feedback on my PhD proposal, which has helped me to improve upon and present the work here.

I would also like to thank the U.S. National Science Foundation, U.S. Department of Energy, and the Semiconductor Research Corporation for financial support of my work.

I also would like to thank my colleagues and collaborators who worked with me on the three-color lithography project, which enabled my initial fundamental studies and gave me my initial exposure to the field of photolithography. Thank you to the UMD group of Prof. John Fourkas, Prof. Daniel Falvey, Prof. Amy Mullin, Sandra Gutierrrez Razo, Zuleykhan Tomova, Nikolaos Liaros, Daniel Jovinelli,

Matthew Hourwitz, Hannah Ogden, Steven Wolf, Matthew Thum and Dr. John Petersen from imec for the years of insightful discussions and comradery that gave me a positive outlook and a different perspective on my research, which I greatly appreciate.

I would also like to thank my collaborators from IBM, Dr. Sebastian Engelmann, Dr. Robert Bruce, Dr. Eric Joseph, and Dr. Dominik Metzler as well as members from Tokyo Electron, Dr. Angelique Raley and Dr. Andrew Metz for their support of my recent work, which allowed me to apply my research towards a useful application and pursue a career opportunity.

I would also like to thank my collaborators from other fundamental projects including Dr. Carles Corbella, Dr. Sabine Portal, and Dr. Youngsik Seo for their experience and knowledge in helping to apply my work in a broader context.

A significant portion of this work would not have been possible without the support of my colleagues in Prof. Oehrlein's lab who have become some of my best friends. Thank you to Dr. Elliot Bartis, Dr. Dominik Metzler, Dr. Andrew Knoll, Dr. Chen Li, and Dr. Pingshan Luan for welcoming me into the lab and giving me the confidence to get started in the field of plasma science. Thank you to Kang-Yi Lin for sharing your vast experience and knowledge with me daily to help direct my research. Thank you as well to Dr. Shiqiang Zhang, Yudong Li, and Sang-Jin Chung for sharing your lab experiences with me. I have made many fond memories with all of you during my time in the lab and I hope that we will work together again in the future.

I am also grateful for the experiences and contributions that I have received from the interns and undergraduate students who have worked with me over the years including Stephen Hong, Alex Jennion, Qixin Yang, and Eike Beyer.

Thank you to the many individuals in the Department of Materials Science and Engineering and IREAP for your support of all my academic needs. Thank you to Kathleen Hart, Kay Morris, Jenna Bishop, Ginette Villeneuve, Karin Shortino, Brian Quinn, Nolan Ballew, Dottie Brosius, William Schuster, and Thomas Weimar.

I would like to thank the many friends that I made over the course of my graduate studies who were there alongside me in our collective journey towards a doctoral degree. It has been a pleasure to be in your company over these years.

I owe a great amount of gratitude to my family, my mother Katarina, my father Pavol, and my sister Paula Pranda for their resolve when times were difficult and for being selfless in giving me the opportunities to succeed in my personal and academic pursuits. I could never say thank you enough!

I would also like to thank my parents and sister in-law, Irina, Alexander, and Victoria Shumakovich for their continued support.

Lastly, no amount of words could express my gratitude for my wife Marina Pranda, who has selflessly supported me in the more than nine years that we have spent together while earning both our Bachelors and PhD degrees. I would not be the successful person I am today were it not for the tireless dedication and numerous sacrifices that she has made in the interests of myself and our growing family.

Finally, I would like to acknowledge my son Emil. He is the biggest bundle of joy who brings me so much happiness every day. He motivates me to constantly give

my maximum effort and improve myself, and I will always strive to be the best that I can be for him and my family.

Table of Contents

List of Tables

List of Figures

Chapter 1: Introduction

Photoresist (PR) materials are an essential component in the patterning of features for semiconductor devices. In semiconductor device manufacturing, PR materials function as the intermediate medium that facilitates the fabrication of features into a substrate material.[1] Initially, the desired device features are patterned on the PR material by the process of photolithography, in which light is shown through a photomask that contains the pattern of the device features. The light that is transmitted through the photomask is of a specific wavelength such that when it impinges on the PR material, it results in a photochemical reaction to occur in the PR material that transfers the pattern from the photomask into the PR material.[2] After a cleaning step, the features present in the PR material are transferred into a substrate material by the use of a plasma etch process. In order to meet the etch requirements, the composition and structure of the PR material contains components that enable the preservation of the lithographically patterned features under a plasma etch process.[3–5] Specifically, the PR materials consist of a polymer backbone that undergoes crosslinking and bond scissioning reactions as a result of both the light exposure in the photolithographic process and the interaction with photon and ion species that are present in the plasma process.[6,7] Therefore, in order to preserve the fidelity of the features after lithography and after plasma exposure, characteristics of the PR such as an elemental composition with minimal oxygen content or a molecular structure with aromatic functional groups, are essential for improving etch resistance under a plasma exposure.[4,7,8] Previous works have established a good correlation between the net

etching behavior and the intrinsic chemical composition.[7,9–14] However, the interactions among the various species in the plasma and the components of the PR composition do not result in uniform etching throughout the process duration. The components of the plasma, namely the vacuum ultraviolet (VUV) photons, ions, and reactive species, induce additional modifications to the PR molecular structure in the form of photon-induced bond formation and scission, ion-induced scission of volatile species, and reactive-species-induced chemical transformation of the sample surface.[15–19] Each of these interactions has both a temporal and a spatial dependence, which results in the development of a depth-dependent PR layer structure that has significant implications on key PR properties such as the etching and surface roughening behavior.[20] Thus, although there is an established understanding of the mechanisms of the photon and ion species in the plasma that lead to crosslinking and scissioning of the PR molecular structure, the extent of correlation of these modifications to the PR etching and roughening behavior was not clear. Acquiring an understanding of the underlying mechanisms that result in the evolution of the PR etching behavior is beneficial for predicting PR behaviors under plasma etch processes, especially with the emergence of advanced processes such as atomic layer etching (ALE) that do not utilize a continuous process.[21] Furthermore, having the ability to follow and analyze the evolution of the PR behavior over the entire duration of a plasma process represents a significant advantage in the scope of industrial applications that typically only analyze the starting and ending states of the PR, thus lacking the intermediate data that contains the key information for determining the underpinnings of the PR response under a plasma process.[22]

1.1 Objectives

The first objective of this work is to establish a fundamental understanding of the relationships among the PR molecular structure, the developed plasma-induced modifications of the PR materials, and the corresponding PR behaviors such as the etch rate and developed magnitude of surface roughness. This initial work begins with a simplified plasma process to establish a framework for our analysis methodology of plasma-photoresist interactions, and then progresses to the evaluation of a more complex plasma composition that is more relevant in industrial applications. This work proceeds into the second objective, which is to apply the knowledge from the plasma-photoresist interaction study, to investigate several key challenges that are currently present in industrial etch applications. First, we seek to leverage the establishment of plasma-induced PR modification to provide a solution for an industrial motivation to improve the performance of pattern transfer applications. Second, we utilize a PR material to investigate the impacts of sample geometry on nonuniform etching as a result of plasma-sheath-induced variations in the incident ion angle. Our evaluation of these industrial challenges highlights the significance and applicability of understanding the underlying relationships between plasma processes and PR materials.

1.2 Description of PR Materials

For the first objective of this work, we utilized 200 nm thick blanket films of a 193 nm PR material that was thoroughly characterized in prior works.[23,20] The extensive prior characterization and the prominent use of this class of PR in industrial applications throughout the 2010s justified the use of this PR as the benchmark

material for our initial work. For the initial study in our second objective, which involved an industrial pattern transfer application, we transitioned to the use of a model extreme ultraviolet (EUV) PR material, as this class of PR materials is emerging as the next generation of PR materials for enabling fabrication processes with feature sizes smaller than ten nanometers. The model EUV PR was found to have a nearly identical etching behavior to that of a commercial EUV PR with a confidential proprietary formulation, and therefore the model EUV PR was used, as it allowed for supporting characterization of the impacts of the plasma process on the chemical composition and molecular structure. As part of this study, blanket samples of SiO_2 were also used to evaluate the etching performance of the plasma process and determine an overall SiO_2/model EUV PR etching selectivity. In the final work for our second objective, which involved the characterization of the influence of the incident ion angle on PR etching uniformity, we used a modern 193 nm PR with a proprietary formulation, as it provided a good visibility of the directional ion effects that were essential to interpreting the results.

1.3 Description of Plasma Processes

All the work was performed in a low-pressure inductively coupled plasma (ICP) reactor, which has the key ability to selectively control the plasma density and ion energy independently of one another. This type of plasma reactor is one of the technologies commonly used in industrial etch processes. The reactor was operated at a base pressure below 10^{-6} Torr, which ensures a clean operating condition that minimizes the presence of species that are not a part of the desired plasma composition. Additionally, the use of a load lock to transfer samples into the

processing chamber eliminates any atmospheric species from interfering with the process conditions. The ICP reactor consists of a spiral antenna on a quartz dielectric that is located 13 cm above a 12.5 cm diameter Si electrode. The plasma is created by excitation of the antenna at an RF frequency of 13.56 MHz. Additional control of the ion energy is provided by biasing the substrate at a radio frequency (RF) of 3.7 MHz. A consistent sample temperature of 10 °C was maintained by using water-cooling on the substrate backside.

In the first part of this work (Chapters 2-3), an inert argon continuous wave (CW) plasma with a constant substrate bias to accelerate ions was used for all experiments. The purpose of the constant bias was to increase the energy of the incoming ions such that it resulted in the formation of a prominent ion-modified dense amorphous carbon (DAC) layer on the PR surface.

For the experiments in Chapter 2, an energetic inert plasma condition was used to produce a constant thickness of the surface DAC layer for all experiments as the DAC layer was the focus for this initial study. Then, a pulse of oxygen gas of various durations was introduced into the chamber in order to deplete the DAC layer and track the corresponding impact on the etching behavior of the bulk PR material. The setup of this experiment was primarily used to understand the development and evolution of the DAC layer, as the use of an inert plasma condition is not viable for meaningfully etching substrate materials in a pattern transfer process.

In Chapter 3, different magnitudes of the constant substrate bias were used to produce DAC layers of varying thicknesses. However, for these experiments, a pulse of a fluorocarbon (FC) precursor, octafluorocyclobutane (C_4F_8), was used, as it is

more relevant to plasma etch applications.[4,24–26] Similarly to the first set of experiments, the impact on the PR etch behavior was explored along with the interaction of the FC species with the DAC layer. The use of a reactive plasma chemistry is more representative of a condition that is used in a pattern transfer process, however the sequential use of an energetic inert argon plasma followed by an FC pulse differs from a typical CW pattern transfer process where argon and a FC precursor are simultaneously present from the beginning of the plasma process.

In Chapter 4, we transitioned to the use of an atomic layer etching (ALE) process that consisted of a continuous argon plasma and cyclic injections of an FC precursor, either C_4F_8 or CHF_3, and periodic activation of substrate biasing. The systematic evaluation of the available components of the wide parameter space in an ALE process, including the ion energy magnitude, etch step length (ESL), and FC deposition thickness, ultimately realized improved SiO_2/PR etching selectivity compared to a CW process.[27–29] The conditions and setup of this experiment are fully representative of a commercial pattern transfer process, with the exception of the separate blanket PR and SiO_2 films that were used for surface characterization purposes.

The last set of experiments in Chapter 5 utilized a CW argon plasma with a fixed -100V substrate bias in order to produce surface morphology that allowed for the detection of off-normal ion effects. While a reactive plasma chemistry was not used, the magnitude of the off-normal ion effects under an inert plasma condition still provides a general guideline for the magnitude of off-normal ion effects that can be

expected to be present under the typical conditions used in a pattern transfer application.

1.4 Experimental Approach

The starting point for interpreting the behavior of the PR material was to implement previous knowledge of the modifications that occur to PR materials from plasma exposure into an approach that could relate these modifications to the etching behavior in a plasma process. Previous work developed a good understanding of the photoresist modifications that arise from both VUV irradiation and ion bombardment in a plasma process.[11,30] Specifically, at high ion energies, there is significant bond scissioning in the surface layers and depletion of oxygen, hydrogen, and volatile-product-forming species. This process results in the formation of a DAC layer with a thickness that is related by the ion penetration depth.[7,11,23] The findings from prior works, which observed that the physical properties of the DAC layer include a density and etch resistance that are significantly greater than those of native photoresist polymers, provided the motivation for us to focus on the development of the DAC layer in a plasma process.[3,31] In order to track the evolution of this layer in a plasma process, we extensively relied upon *in situ* ellipsometry as the centerpiece characterization method for providing real-time information on the evolution of the PR material. The raw data provided by ellipsometry contain the collective information of the entire PR thickness. Analysis of the data required the development of an ellipsometric model to clearly define and track the evolution of individual layers within the PR structure. Each of the layers in the ellipsometric model is defined by a thickness and a refractive index, thus allowing for tracking the real-time evolution of

the etching behavior and the developed surface modification via the refractive index. For example, the increase in density that corresponds with the formation of a DAC layer manifests itself as an increase in the refractive index. One of the key limitations of the ellipsometric setup, though, is that it does not provide any information about the chemical properties of the sample. Therefore, the use of secondary characterization and supplemental knowledge of the material system is vital for ensuring realism of the ellipsometric model. Thus, we utilized a combination of x-ray photoelectron spectroscopy (XPS) to justify the carbon-rich surface region that signifies the presence of the DAC layer and ion implantation simulations to define the DAC layer thickness based on the ion energy.

After defining our modeling approach for the first study, we decided upon an experimental approach in which a stable DAC layer of a set thickness was developed and then selectively depleted by oxygen species. Our justification for this approach was that the strong distinctiveness of the ellipsometric data during the DAC layer depletion, as further explained in Chapter 2, allowed for clear interpretation of the time-dependent thickness changes of both the DAC and bulk layers. The determination of these behaviors allowed us to realize the key finding of this work, which is the significance of single nanometer changes in the thickness of the DAC layer leading to up to an order of magnitude difference in the etch rate of the bulk PR material. This study established the fundamental importance of the ion-induced surface modification, the DAC layer, as a component of the etching behavior of a PR material.

In the second set of baseline experiments, described in Chapter 3, we utilized the setup from the first set of experiments involving the DAC layer, but with two main modifications. First, a FC precursor, C_4F_8, was used instead of oxygen to deplete the DAC layer, as this type of plasma chemistry is more relevant for applications such as pattern transfer. Second, we developed various thicknesses of the DAC layer to be representative of a wider range of conditions under which the DAC layer would be present. By utilizing similar secondary characterization via XPS analysis at various points in the process cycle, we augmented our initial ellipsometric model to interpret the interaction between FC species and the DAC layer. The key finding from this work emphasized that the FC species react with the DAC layer to produce an FC-rich modified layer that has intermediate properties of both the DAC layer and a native FC layer. However, this modified layer still enhances the etch resistance of the PR material.

For the application-focused part of this work, starting in Chapter 4, we explored solutions for an industrial objective which sought the improvement of pattern transfer performance in applications with increasingly smaller feature sizes of ten nanometers and below. In order for the research to be relevant in modern processes, this work necessitated the use of an EUV PR. However, a key limitation of EUV PRs is a smaller available starting thickness compared to 193 nm PRs. Although a pattern transfer process involves PR-defined features over a hard mask material, such as SiO_2, we instead decided to utilize blanket samples of both EUV PR and SiO_2 in order to maintain our capability to use *in situ* ellipsometry. Ellipsometry is an optical technique which requires flat, uniform surfaces to produce meaningful data

from the light reflected off the sample surface. Any surface structures would scatter the incoming light and reduce the signal integrity captured by the detector. We also decided to transition from a CW process to an ALE process, due to the previously demonstrated ability of an ALE process to control the etching behavior more precisely compared to a CW process as a result of greater flexibility in the processing parameters. Additionally, a CW process with reactive plasma species does not allow a prominent DAC layer to form, and thus there is no significant improvement in the PR etch resistance. The hypothesis of this work was that the ALE processing parameters could be systematically evaluated to find conditions in which the thickness loss of the EUV PR could be minimized through the development of characteristic surface modification. At the same time, the etching behavior of the SiO_2 would continue unimpeded due to the absence of the native carbon content, which forms a modified surface layer in the PR material. Utilizing our previous knowledge, we implemented an ALE setup that developed a prominent FC-rich modified layer from the interaction between energetic argon ions and a deposited FC layer that strongly inhibited the thickness loss of the EUV PR while maintaining an acceptable etching behavior on the SiO_2. Thus, we were able to develop a process with a good overall SiO_2/PR etching selectivity that has the potential to be applied in an industrial pattern transfer process.

The work done in Chapter 6 was focused on providing insights into the impacts of nonuniform PR etching as a result of variations in the incident ion angle that arise from the sample geometry. The variation in the incident angle occurs mainly at the sample edges, due to the geometry of the plasma sheath that surrounds

the sample. Ions are accelerated normal to the plasma sheath. Thus, areas where the sheath wraps around the sample, such as near the edges, experience ion bombardment that is not normal to the sample surface. As the incident angle moves farther away from normal, the etch yield increases, with a maximum occurring at 45°. Thus, a spatial ellipsometric scan across the sample surface can elucidate the enhanced thickness etched near the sample edges. Additionally, the variation in the incident ion angle can also be seen in the atomic force microscopy (AFM) analysis of the surface morphology with the presence of ripple features. We find that for that tested plasma condition, the extent of the directional ions extends approximately 1000 μm from the sample edge. The insights from this study provide an initial overview of the scope of the etching and morphological impacts near the edges of samples, which is essential for controlling sample uniformity in plasma etch processes.

1.5 Overview of Characterization Methods

Numerous characterization techniques were used to support the interpretation of the plasma-photoresist interactions. The following section describes an overview of the employed characterization techniques. Further details of each method that are specific to each of the main research objectives are discussed in their respective chapters.

1.5.1 Ellipsometry

In situ and line-scan spatial ellipsometry were used to interpret the layer structure of the PR materials via an optical model that translates the raw data, collected as the amplitude ratio (psi) and phase difference (delta) of the reflected light, into a thickness and refractive index for each defined layer. The ellipsometer,

model SOFIE STE70, was set up in the polarizer-rotating compensator-sample-analyzer configuration using a wavelength of 632.8 nm.

1.5.2 X-ray Photoelectron Spectroscopy (XPS)

XPS analysis was used to provide information about the surface chemistry, specifically the presence of specific chemical bonds, of the PR materials at various points in the plasma process. The analysis was performed using a Vacuum Generators ESCA Mk II surface analysis chamber with a non-monochromatized Al Kα X-ray source (1486.6 eV). The instrument was operated in a constant-energy analyzer mode with a 20 eV pass energy. Electron take-off angles of 20° and 90° were used to probe the chemical evolution of the PR surface. The probing depths of the 20° and 90° scan angles are approximately 2 nm and 8 nm, respectively. All plasma processed samples were delivered for XPS analysis using a vacuum transfer system to prevent any interaction with ambient atmospheric species.

1.5.3 Atomic Force Microscopy (AFM)

AFM analysis was used to provide information on the surface morphology of the PR samples. The analysis was performed using an Asylum Research MFP3D instrument in the tapping mode configuration with a fixed scan size of 10 μm × 10 μm. Surface roughness information from these scans was quantified by calculating the root mean square (RMS) roughness of the surface profile. Information on the surface roughness distribution and characteristic roughness wavelengths was also obtained via a power spectral density (PSD) analysis.

1.5.4 Attenuated Total Reflection Fourier Transform Infrared Spectroscopy (ATR-FTIR)

ATR-FTIR characterization was used to complement the XPS analysis by providing information on the impacts from the plasma process to specific functional groups within the PR composition. The FTIR setup consisted of a Shimadzu IRTracer-100 equipped with a HgCdTe (MCT) detector and variable angle single-reflection ATR accessory with a Ge crystal. The incident light angle at the Ge crystal was set to 60°. The use of an ATR accessory in combination with a Ge crystal probes the sample surface down to a depth of approximately 500 nm. A ZnSe polarizer was installed on the optical inlet of the ATR accessory to induce p-polarization of the incident IR light. IR spectra were acquired and averaged over 20 scans from 600 cm^{-1} to 3400 cm^{-1} with a resolution of 4 cm^{-1}.

1.6 Dissertation Outline

The goal of this work is to establish a fundamental understanding of the interactions between plasma species and PR materials and the corresponding implications on properties such as the etching and surface roughening behaviors. By developing a comprehensive understanding of the mechanisms that control the photoresist behaviors under a plasma exposure, we can explain not only how much a PR material is etched for a given plasma process, but also provide insight on the contributions of aspects such as the PR composition and layer structure on the time dependent evolution of the etching behavior. Ultimately, we can leverage the knowledge of plasma-photoresist interactions to establish a framework to tailor plasma processes and compatible PR materials that are relevant for and meet the

requirements for practical industrial applications. A visual depiction of the organization and flow of the thesis work is shown in Figure 1.1.

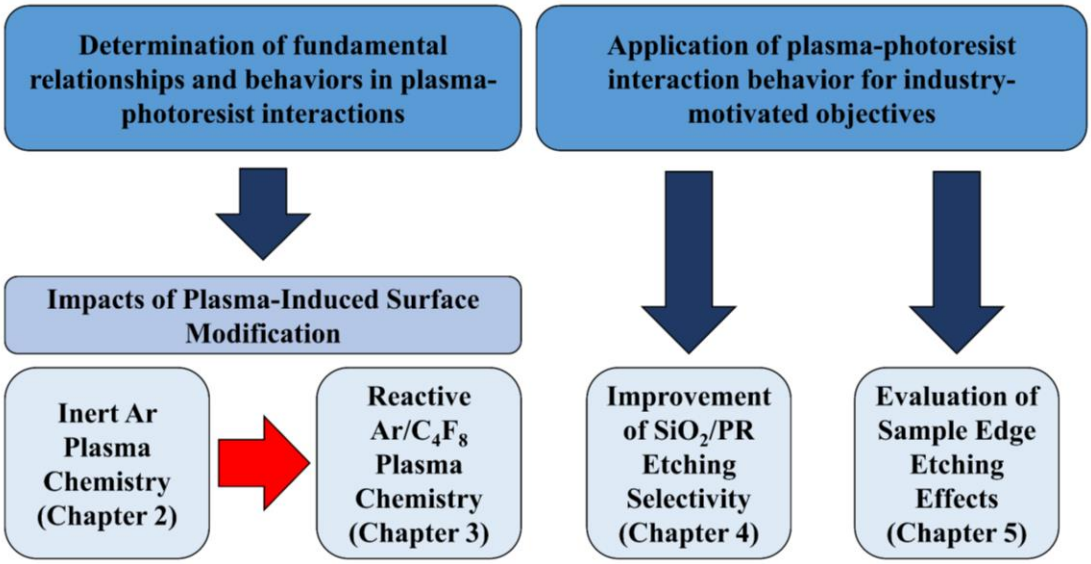

Figure 1.1. Outline of the experimental approach of the research presented in this dissertation.

In Chapter 2, we examine the etching behavior, surface roughness evolution, and surface chemistry evolution of the 193 nm PR material that is exposed under an energetic inert argon-only plasma process. We utilized the XPS characterization in combination with *in situ* ellipsometry to develop our initial ellipsometric model, which describes the development of a surface DAC layer as being a contributing factor towards the controlled etching of a PR material. This study emphasized the large variation in the overall PR etching behavior that occurs as a result of changes in the thickness of the DAC layer on the order of nanometers.

In Chapter 3, we expand upon our initial study of the 193 nm PR material to examine the impacts from a plasma process that contains a reactive C_4F_8-based gas chemistry, due to its relevance to industrial pattern transfer applications. A similar

approach as in the initial study in Chapter 2 allows us to develop a revised ellipsometric model that highlights a process by which the FC species in the plasma react with the DAC layer to produce a modified layer that has intermediate properties to those of a pristine DAC or FC layers. This study also shows the effect of FC species on reducing the magnitude of surface roughness which initially forms from ion bombardment.

In Chapter 4, we apply the knowledge from the previous chapters to address a current industrial challenge of enabling highly selective pattern transfer of features approaching dimensions of ten nanometers and smaller. For this work, we utilize a model EUV PR that is relevant for modern industrial processes. To enable a high degree of selectivity, a minimization of the PR thickness loss is required. We find that by incorporating an ALE process with a moderately energetic etching step, a prominent FC-rich modified layer develops on the PR surface that strongly mitigates the PR thickness loss even in the presence of reactive FC species. Furthermore, etching of SiO_2, which is necessary for a pattern transfer application, continues unimpeded by this approach, resulting in a high net SiO_2/PR etching selectivity.

In Chapter 5, we investigate another industrial challenge pertaining to maintaining thickness uniformity during an etch process. We utilize extensive AFM characterization with PSD analysis to elucidate the extent of varying directionality in the ion bombardment as a result of the interaction between the plasma sheath and sample geometry. We find that the areas near the edge of the sample within several Debye lengths exhibit elevated surface roughness with the formation of ripple features from shallower angle incident ions. This study provides useful insights on the

implications of local plasma-surface interactions for semiconductor manufacturing applications.

Lastly, Chapter 6 provides an overall summary of the thesis work and discusses the future direction of the research.

Chapter 2: The Role of the Dense Amorphous Carbon (DAC) Layer in Photoresist Etching

Adam Pranda[1], Sandra Abigail Gutierrez Razo[2], Zuleykhan Tomova[2],

John T. Fourkas[2,3,4], and Gottlieb S. Oehrlein[1]

[1]Department of Materials Science and Engineering and Institute for Research in Electronics and Applied Physics, University of Maryland, College Park, Maryland 20742

[2]Department of Chemistry and Biochemistry, University of Maryland, College Park, Maryland 20742

[3]Institute for Physical Science and Technology, University of Maryland, College Park, Maryland 20742

[4]Center for Nanophysics and Advanced Materials, University of Maryland, College Park, Maryland 20742

A. Pranda performed all the experimental work and analysis in this chapter. The other authors assisted with collaborative discussion of the supporting ideas behind the work in this chapter.

Reprinted with permission from A. Pranda, S.A. Gutierrez Razo, Z. Tomova, J.T. Fourkas, and G.S. Oehrlein, J. Vac. Sci. Technol. A Vacuum, Surfaces, Film. **36**, 021304 (2018).

Abstract

The development of new photoresists for semiconductor manufacturing applications requires an understanding of the material properties that control the plasma etching behavior. Ion bombardment at ion energies of the order 100s of eV is typical of plasma-based pattern-transfer processes and results in the formation of a dense amorphous carbon (DAC) layer on the surface of a photoresist, such as the PR193-type of photoresist that currently dominate the semiconductor industry. Prior studies have examined the physical properties of the DAC layer, but the correlation between these properties and the photoresist etching behavior had not been established. In this work, we studied the real-time evolution of a steady-state DAC layer as it is selectively depleted using an admixture of oxygen into an argon plasma. Observations of the depletion behavior for various DAC layer thicknesses motivate a new model of DAC layer depletion. This model also correlates the impact of the DAC layer thickness with the etch rate of the bulk photoresist. We find that up to a 40% depletion of the DAC layer thickness does not have a significant impact on the bulk photoresist etch rate. However, further depletion results in an exponential increase in the etch rate, which can be up to ten times greater at full depletion than for the fully formed DAC layer. Thus, with these trends we show that the photoresist etch rate is controlled by the thickness of the DAC layer. Furthermore, thickness loss of the DAC layer in an O_2-containing plasma coincides with a chemical modification of the layer into an oxygen-rich surface overlayer with properties that are intermediate between those of the DAC layer and the bulk photoresist. Support for this interpretation was provided via X-ray photoelectron spectroscopy characterization. Atomic force

microscopy was used to gauge the impact on surface roughness as the DAC layer is formed and depleted. The trends established in this work will provide a benchmark in our development of new photoresists, which will be suitable for pattern transfer processes that will ultimately be a part of enabling smaller semiconductor device feature sizes and pitches.

2.1 Introduction

A plasma-exposed photoresist can undergo modification due to processes that include vacuum ultraviolet (VUV) irradiation and ion bombardment.[11,30] These surface modifications are important for the understanding of the steady-state etching behavior in a plasma environment, because at high ion energies there is significant bond scissioning in the surface layers and depletion of oxygen, hydrogen, and volatile-product-forming species. These phenomena result in the formation of a dense amorphous carbon (DAC) layer with a thickness that is proportional to the ion penetration depth.[11,23,7] Previous work involving deposited amorphous carbon films has characterized the physical properties of these films as having a density and etch resistance that are significantly greater than those of photoresist polymers.[31,3] The properties of photoresist-derived DAC films are similar to those of deposited amorphous carbon films. The photoresist layer structure formed in a plasma environment consists of a DAC layer on top of a bulk photoresist layer. The DAC layer behaves as an energy-dissipating layer that is depleted of precursors of highly volatile species, and thus mediates the etching of the bulk. Similar behavior is observed for SiO_2 overlayers on Si-containing photoresists and fluorocarbon overlayers on Si or Si_3N_4.[27,32,33]

The main objective of the work presented here is to examine the etch-mediating behavior of the DAC layer by describing the quantitative relationship between the thickness of the DAC layer and the corresponding etch rate of the bulk photoresist. By selectively controlling the thickness of the developed DAC layer via oxygen addition to the plasma composition, we have identified the threshold DAC layer thickness required for maintaining a steady-state photoresist etch rate and have identified an exponentially increasing etch rate trend with decreasing DAC layer thickness below this threshold.

One of the secondary effects that we have observed by controlling the DAC layer thickness via oxygen injection is that thickness loss occurs concurrently with a chemical modification of the DAC layer. Based on evidence from X-ray photoelectron spectroscopy (XPS), depletion of the DAC layer coincides with the formation of an oxygen-rich overlayer on the DAC layer. The optical density of this overlayer is intermediate between those of the DAC layer and the bulk photoresist layer, which is consistent with amorphous carbon erosion mechanisms that have been explored for deposited films.[34–36] These observations provide insights into the sensitivity of the DAC layer to processing conditions, as a stable DAC layer is required for maintaining a stable and reproducible photoresist etch rate.

For pattern-transfer applications, a well-controlled photoresist surface roughness is as critical for reproducibility as is the etch rate. Although VUV irradiation plays a lesser role in the etching of a photoresist relative to ion bombardment, a synergistic effect between VUV irradiation and ion bombardment leads to a buckling instability in UV-sensitive photoresists, resulting in surface

roughening.[8–10,19] Attaining critical feature sizes requires the minimization of surface, line edge, and line width roughness to preserve feature fidelity.[37,38] Characterization of photoresist surfaces by atomic force microscopy (AFM) can be used to correlate the impact of the DAC layer thickness and structure on the observed surface roughness.

In this article, we evaluate the influence of the DAC layer thickness on etching behavior, photoresist structure, and surface roughening using an industry standard PR193 photoresist. Experimental data collected using XPS, AFM, and ellipsometry provide the basis for an ellipsometric model that describes the evolution of the photoresist layer structure. Application of this model to time-dependent ellipsometric data allows for the real-time thickness tracking of each of the individual layers that compose the photoresist structure.

2.2 Experimental Setup

The samples used in this work consisted of a 193 nm photoresist material produced by the Japan Synthetic Rubber Corporation (JSR) that has been extensively characterized.[23,20] In this work, we studied the photoresist in the form of a blanket film with a thickness of approximately 200 nm. The general formulation of 193 nm photoresists consists of a terpolymer structure with a polymethylmethacrylate (PMMA)-based backbone with leaving, lactone, and polar groups serving as the functionalized side groups.[7]

Plasma etching of the samples was conducted using an inductively coupled plasma (ICP) reactor. The system consists of a spiral antenna on a quartz dielectric that is located 13 cm above a Si electrode with a 12.5 cm diameter. We operated the

top antenna at an excitation frequency of 13.56 MHz. The substrate was biased at a radio frequency (RF) of 3.7 MHz. Additionally, the substrate temperature was maintained at 10 °C using water-cooling on the substrate backside.

For the plasma processing of the samples, we kept the chamber at a pressure of 10 mTorr. An argon plasma with a 40 sccm flow rate was used as the carrier gas. We used a source power of 300 W. Immediately after plasma ignition, we applied a -100 V substrate bias to bombard the sample with high-energy (up to ~125 eV) ions. This steady-state configuration is representative of the conditions that are used for photoresist pattern transfer.[3]

The general processing diagram for the experiments is shown in Fig. 2.1. The three phases of the processing setup, pre-bias, Phase I, and Phase II, correspond to setting up the gas flow in the absence of plasma, observing the formation of the DAC layer, and observing the depletion of the DAC layer, respectively. The computer-controlled gas injection system introduced oxygen into the chamber for intervals of 2, 6, and 10 s to modify the DAC layer by varying amounts. The flow rate of the oxygen was set so that the differential pressure between the argon and oxygen flows would be minimized, ensuring a smooth flow of oxygen into the chamber during the oxygen pulsing.

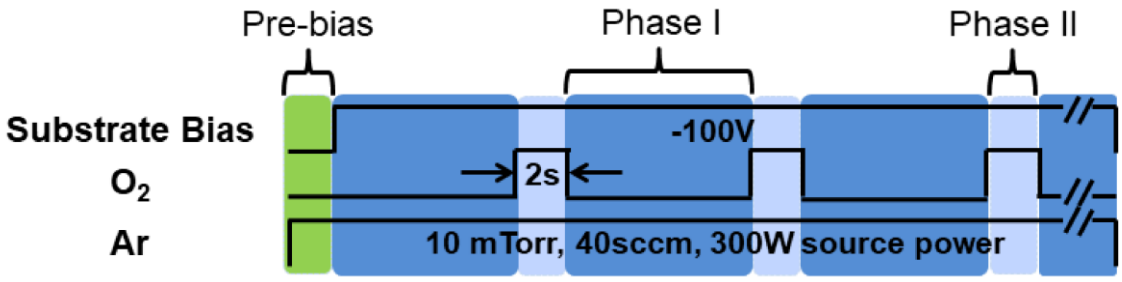

Figure 2.1. Schematic of the experimental setup. The formation and depletion of the DAC layer are observed in Phases I and II, respectively.

Information regarding the thickness and refractive index of the photoresist structure was collected in real-time using *in situ* ellipsometry in the polarizer-rotating compensator-sample-analyzer configuration at a wavelength of 632.8 nm. We interpreted the raw data generated from ellipsometry, parameterized through the optical constants psi and delta, by an optical model that incorporates modification to the photoresist from VUV irradiation and ion bombardment.

Ellipsometry is a powerful tool for examining the evolution of the photoresist layer structure, as any deviations in the trajectory of the raw data correspond to a change in the thickness and/or the refractive index of one or more of the layers. Notably, under steady-state etching conditions, the initial deviation in the trajectory (Fig. 2.2a), which is characteristic of Phase I in our processing setup, corresponds to an impact on the photoresist structure. This deviation is due primarily to the formation of the DAC layer from the impact of high-energy ion bombardment. The high reproducibility of the data under different conditions indicates that the photoresist structure responds in a consistent manner to high-energy ion bombardment. Changes from the steady-state structure can be probed by transiently altering the plasma composition for a fixed duration. We implement this process by using a computer-controlled gas injection system to introduce oxygen into the plasma for various durations. The alteration of the steady-state plasma condition corresponds to Phase II in our processing setup. The advantage of this approach is that we can control the degree of modification of the DAC layer. The impact of the oxygen pulse on the overall photoresist structure and the corresponding etch rates can be ascertained for both partial and complete modification of the DAC layer.

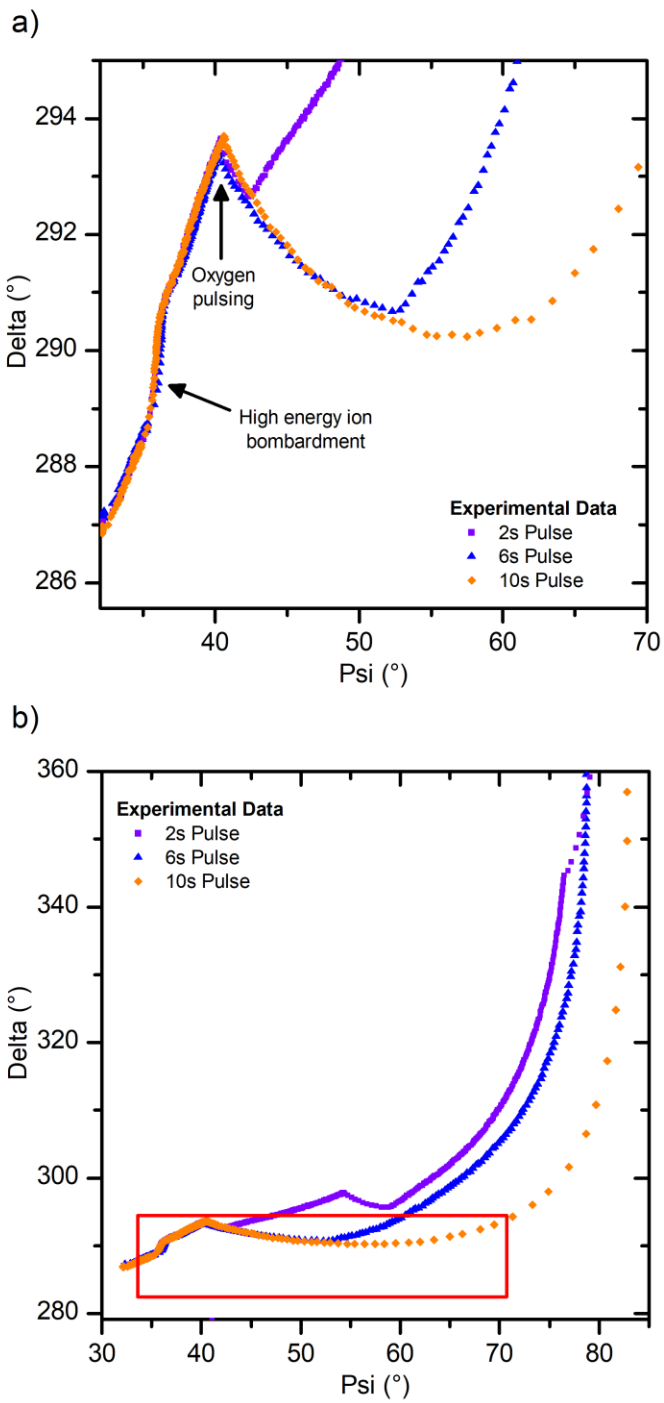

Figure 2.2. (a) Depiction of the events responsible for the deviations in the ellipsometric data. (b) Raw ellipsometric data for the various oxygen pulse lengths used. The box indicates the region of interest in this study, which is shown in (a).

Post-processing, we obtained information about the chemical structure and morphology of the samples with XPS and AFM. The XPS analysis was performed using a Vacuum Generators ESCA Mk II surface analysis chamber with a nonmonochromatized Al Kα X-ray source (1486.6 eV). Spectra were obtained at emission angles of 20 and 90 degrees in the constant-energy analyzer mode at a 20 eV pass energy. To preserve the surface condition post-processing, we moved all samples to the analysis chamber using a vacuum transfer system. The AFM analysis was performed using an Asylum Research MFP3D instrument in the tapping mode configuration with a fixed scan size of 2 μm × 2 μm. We acquired surface roughness information from these scans by calculating the root mean square (RMS) of the surface profile.

In addition to evaluating the sample properties, we also determined the composition of the plasma using optical emission spectroscopy (OES). The oxygen emission line near 844 nm was monitored relative to the argon emission line near 764 nm, as the ratio of their intensities provides information on the fraction of dissociated oxygen that is present in the plasma. The fraction of dissociated oxygen can, in turn, be related to the ellipsometric etching data. The 844 nm oxygen emission line was chosen because emission at this wavelength corresponds to the formation of atomic oxygen, which is the main oxygen reactive species that interacts with the sample surface.[14,39]

2.3 Results

Our interpretation of the structure and etching behavior of the photoresist system is based primarily on the fitting of the raw ellipsometric data to a model. In

the following section, we discuss the experimental data that were used to develop and support the model, and the behavior of the photoresist as interpreted by this model.

2.3.1 Ellipsometry

The psi-delta trajectories obtained via ellipsometry for the different oxygen pulse lengths used are shown in Fig. 2.2b. We implemented a cyclic process, with the pulsing repeating every forty seconds for each pulse length. This approach permits the effect of the modification from oxygen to be observed in a time-dependent manner and also allows us to verify the reproducibility of the modification. In the boxed area in Fig. 2.2b, which corresponds to the data in Fig. 2.2a, we focused on a comparison of the modification during the first pulse, as the initial state of the photoresist prior to the pulse shows excellent consistency among the three tested conditions. As we discuss below, we can use one model for the quantitative evaluation of the evolution of the layer structure and etch rate as the modification progresses for all the different samples tested.

2.3.2 XPS

The XPS scans shown in Fig. 2.3 provide information on the composition of the surface layer as it undergoes initial modification from high-energy ion bombardment, followed by the subsequent modification from oxygen interaction. We compared the sample before being subjected to the plasma (pristine), during etching but before the oxygen pulse (before-pulse), and during the oxygen pulse (mid-pulse). Compared to the pristine sample, the before-pulse sample has more C-C bonding and less C-O bonding, which is consistent with the formation of a DAC layer on the surface. Similarly, the enhancement of C-O and C=O bonding in the mid-pulse

sample confirms that the oxygen pulse modifies the DAC layer into one that is significantly more oxygen-rich. The C1s spectrum in Fig. 2.3a indicates that oxygen addition produces a shoulder on the main peak that is representative of oxidation of the DAC layer, as has been observed previously.[40] The O1s spectrum in Fig. 2.3b is consistent with previous experimental work that found that C=O and C-O bonds are dominant on an amorphous carbon surface that has been exposed to an oxygen-containing plasma.[41] These XPS findings support the DAC layer structure indicated by our ellipsometric model.

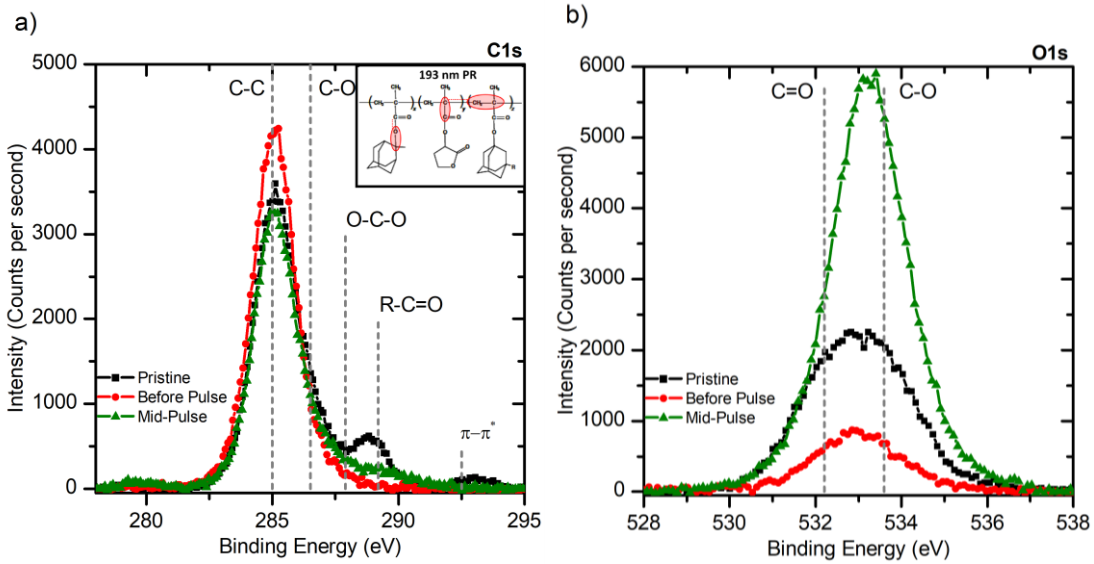

Figure 2.3. XPS spectra of the (a) C1s and (b) O1s peaks for the PR193 samples at various points in the plasma process compared with the pristine sample. The inset in (a) shows the structure of PR193. The circled regions in the structure are prone to bond scission during plasma exposure, and reform the bonds shown with the dotted lines. Reprinted with permission from Weilnboeck *et al.*, J. Vac. Sci. Technol. B **30**, 031807 (2012). Copyright 2012, American Vacuum Society

2.3.3 AFM

Figure 2.4 compares the amount of surface roughening observed in the pristine sample, under steady-state argon plasma etching, during the middle of the

first oxygen pulse, and following each of the first three oxygen pulses. The key observation from these data is that the depletion of the DAC layer during the oxygen pulse does not have a significant impact on the magnitude of the surface roughness. This observation is consistent with current understanding. Stress leads to the formation of a buckling instability and is released by surface roughening. When the DAC layer reforms after the pulse, the magnitude of surface roughness is enhanced relative to the mid-pulse and pre-first pulse conditions. A possible explanation for this behavior is that the loss of oxygen in polymer materials induces surface roughening as stresses form in the material. Increased surface roughness may result from the depletion of oxygen from the DAC layer after the oxygen pulse.[4] As the DAC layer is etched and reformed over subsequent pulses, this mechanism is a likely contributing factor for the increasing surface roughness. Additionally, roughening models have suggested that the mitigation of surface roughness is dependent on the relative magnitudes of the lateral and vertical diffusion of species in the photoresist.[3] Therefore, this interpretation suggests that the enhanced roughness observed after each pulse is a result of an enhanced magnitude of species diffusing vertically instead of laterally in the photoresist. Because the net amount of material etched increases continuously during the plasma exposure, the greater total amount of material removed when each subsequent pulse occurs is consistent with the production of greater surface roughness by the greater net movement of surface species that has occurred up to that point. The significance of these AFM results is that the oxygen-induced modification and depletion of the DAC layer during the pulse does not result in a noticeable change in the surface morphology; this has the implication that a

plasma process that involves oxygen will primarily reduce the thickness of the DAC layer without causing an increase in the surface roughness. The introduction of oxygen in fact mediates any increase in surface roughness since the PR193 surface roughness increases only once the oxygen is removed from the chamber upon the completion of Phase II of our process and an argon-dominant plasma regime is restored in Phase I of the next cycle. The observed magnitude of the surface roughness provides information on the sensitivity of the surface morphology to changes in the photoresist structure as a result of plasma-induced modifications.

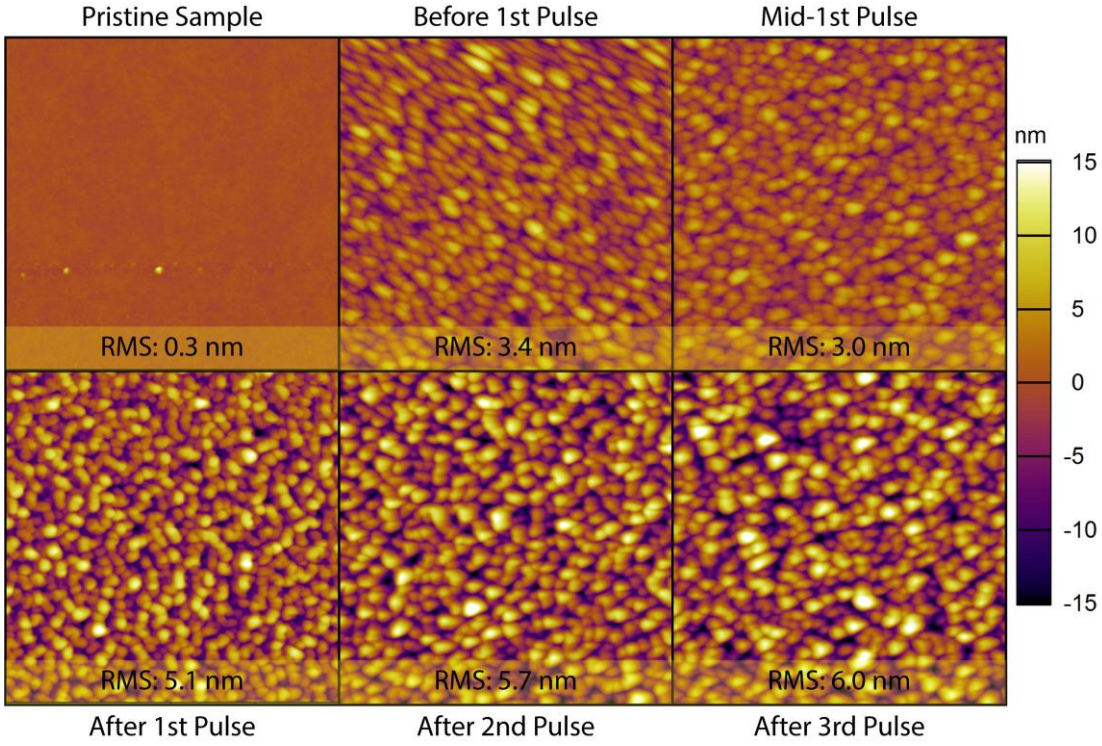

Figure 2.4. AFM scans performed at various points in the plasma etching process. Stresses in the surface layer of the photoresist are released through the formation of roughness. Further pulsing results in additional cycles of DAC layer depletion and formation, increasing the surface roughness.

2.4 Ellipsometric Modeling

Based on our experimental data, we developed a multi-layer ellipsometric model that tracks the evolution of the DAC layer and the bulk photoresist layer during the plasma exposure. In Fig. 2.5a we visualize the model in psi-delta space to describe the significance of the directionality of the raw ellipsometric data. Our model distinguishes between the DAC layer and the bulk photoresist layer, because the XPS data and SEM cross sections in Fig. 2.5b indicate that the DAC layer is a separate entity from the bulk photoresist. In the following sections we discuss the parameters of our ellipsometric model, analyze the modifications to the photoresist structure that occur as the plasma process outlined in Fig. 2.2 proceeds, and comment on the observed relationships that impact the etching behavior.

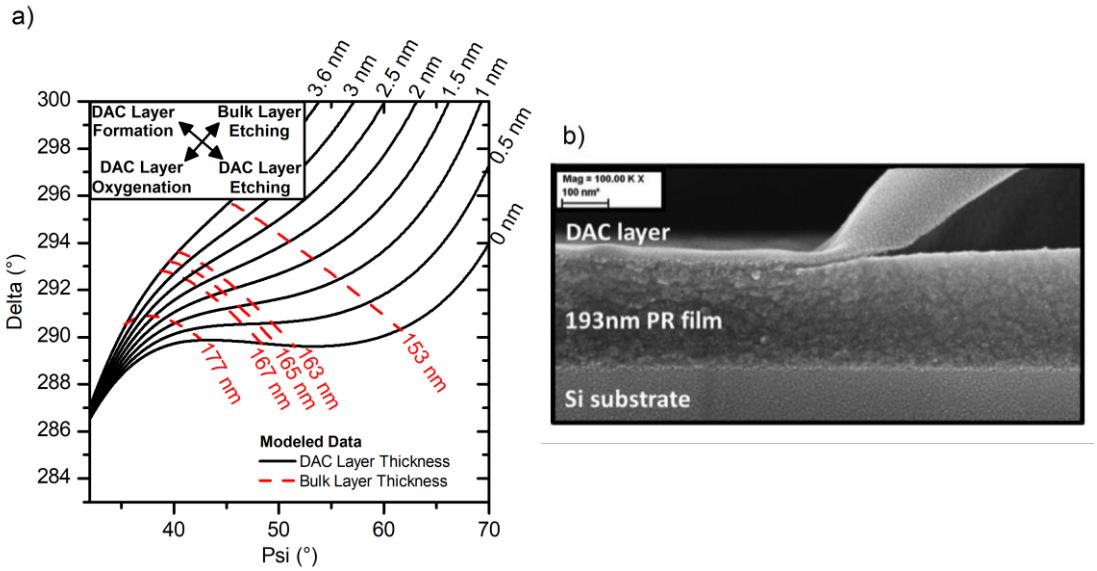

Figure 2.5. (a) Ellipsometric model used for describing the evolution of the DAC and bulk layers in the photoresist. The inset shows the significance of the directionality in the ellipsometric model. (b) SEM cross section of the photoresist structure after plasma processing. Reprinted with permission from Metzler *et al.*, J. Vac. Sci. Technol. B **33**, 051601 (2015). Copyright 2015, American Vacuum Society

2.4.1 DAC Layer Evolution

2.4.1.1 Formation of the DAC Layer

For a pristine, PR193-coated Si substrate, there are three separate layers: the Si substrate, a native SiO_2 layer, and the deposited bulk photoresist. Upon plasma exposure coupled with high-energy ion bombardment, a fraction of the bulk photoresist layer undergoes modification from VUV irradiation. The thickness of the affected layer depends on the VUV penetration depth. For PR193-type photoresists, this penetration depth is on the order of 200 nm.[30] Ion bombardment preferentially removes hydrogen and oxygen from the first several nanometers on the surface of the bulk photoresist layer, thus forming a DAC layer.[42,12] Based on simulations using the Stopping Range of Ion in Matter (SRIM) software package, for an ion energy of 100 eV, the corresponding thickness of the DAC layer is approximately 2.8-3.6 nm for our conditions. This thickness has been confirmed experimentally in previous work.[43,44] We assume that the DAC layer has a uniform refractive index over its entire thickness for the entire pre-pulse duration. In reality, the ion penetration depth decreases as the DAC layer develops and is sustained under biased plasma exposure. As a result, the initially formed DAC layer is eventually converted into a thinner DAC layer with a greater refractive due to the decreased ion penetration depth. Generally, the agreement between the ion-energy-dependent DAC layer thickness measured ellipsometrically and that predicted by SRIM is excellent. This comparison, along with consideration of the effect of the changing ion penetration depth on the DAC layer properties and etching behavior, will be discussed in a future paper. Each layer incorporated in the ellipsometric model can be simulated over a range of

thicknesses or refractive indices of the simulated layer itself and/or of other layers. For evaluating the properties of the DAC layer during plasma exposure, we simulated the thickness of the DAC layer over a range of DAC refractive indices at various thicknesses of the bulk layer. This combination of simulated parameters allows for the evaluation of the DAC layer properties as the bulk photoresist layer is etched away. As the bulk layer is being etched away, it is also modified by VUV irradiation, as the quaternary carbons that make up the PMMA backbone of PR193 photoresist are prone to bond scission upon VUV irradiation.[45] We integrated the rate of modification from VUV exposure into the model for the bulk layer based on an experimental calibration in which no substrate bias was applied, thus minimizing ion bombardment. One consideration that we took into account for the DAC layer refractive index is that the ion-induced dehydrogenation of the photoresist surface results in the development of an amorphous carbon layer that absorbs light, and thus no longer behaves as a pure dielectric material. This phenomenon is modelled by introducing loss in the form of an extinction coefficient.[46,47] A relationship for the magnitude of the extinction coefficient relative to the real component of the refractive index for amorphous carbon films was previously established by Schwarz-Selinger et al.[31] More recent work by Metzler et al. used the work by Schwarz-Selinger, in conjunction with newer studies on amorphous carbon, to improve the accuracy of the extinction-coefficient relationship for a wider range of refractive indices.[20] We used these data to model the DAC layer extinction coefficient.

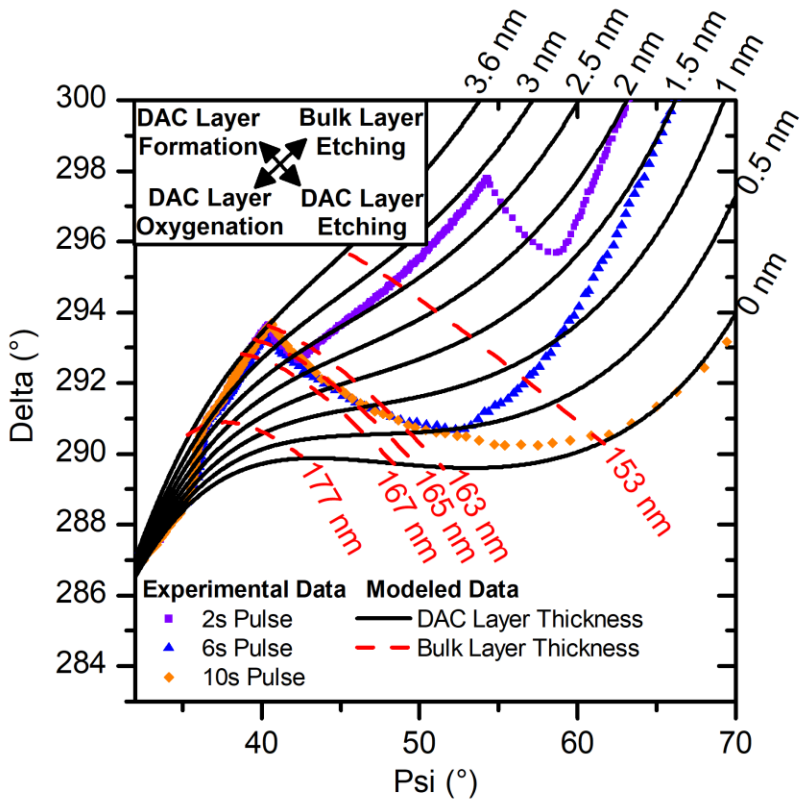

Figure 2.6. Overlay of the experimental data on the ellipsometric model used for describing the evolution of the DAC and bulk layers in the photoresist. (Inset) Significance of the directionality in the ellipsometric model.

Figure 2.6 shows our model superimposed on the raw ellipsometric data. Based on these data, we proposed the following interpretation of the DAC layer behavior. In Phase I of our process, upon initiation of substrate biasing, etching of the bulk layer proceeds. At the same time, there is a distinct change in the trajectory of the psi-delta data, corresponding to the growth of the DAC layer. Prior to the introduction of the oxygen pulse, the DAC layer attains a steady-state thickness of 3.6 nm. Combined with the information from the SEM cross-section in Fig. 2.5b, the XPS data for the before pulse condition in Fig. 2.3, and the reproducibility of the ellipsometric data upon the initiation of high-energy ion bombardment, we have

distinguished the formation of a distinct DAC layer that has a composition that is distinct from that of the bulk photoresist.

2.4.1.2 Depletion of the DAC Layer

In Phase II of our process, the introduction of the oxygen pulse rapidly depletes the DAC layer thickness. Figure 2.6 shows that the DAC layer is partially depleted by 2 s and 6 s pulses, and fully depleted by 10 s pulses. It is evident from the trajectory of the raw data that the addition of oxygen into the plasma selectively depletes the DAC layer, as has been observed previously.[48] Based on our ellipsometric model, the raw data trajectory would seem to imply absence of bulk layer etching for a brief period. In reality, etching of the bulk layer must continue, as there is uninterrupted ion bombardment of the sample. Based on the XPS data, we interpret this behavior as being due to a modification of the DAC layer properties by the interaction with the oxygen species as the layer is depleted. We termed this modification oxygenation of the DAC layer. A close examination of the data trajectory during the depletion of the DAC layer shows that the trajectory tracks in the opposite direction of bulk layer etching, implying a net growth of the thickness of the composite layer. A more plausible explanation is that the oxygen modifies the DAC layer as it is depleted in such a way that the modified DAC layer has properties that are more comparable to those of the less dense bulk layer. Several experimental studies have found that the density of deposited amorphous carbon decreases in an oxygen plasma environment.[35,49,50] Therefore, it is likely that the photoresist-derived DAC layer undergoes a similar modification. Not only is the thickness of the DAC layer reduced, but the refractive index of the oxygenated layer also decreases due to

the incorporation of oxygen. As the refractive index is related to the density, this decrease suggests a decrease in density of the DAC layer as well. To model this modification, we developed a separate model to interpret the properties of the DAC layer during the oxygen pulse, as shown in Fig. 2.7a. The model is based on the one for the formation of the DAC layer, but with the addition of a component to account for oxygen modification. We make two main assumptions for this model. First, the etching of the bulk photoresist layer initially proceeds at the same rate during the oxygen pulse as before the pulse. Second, the refractive index of the oxygenated DAC layer is between those of the unmodified layer and bulk photoresist layer. The first assumption is likely an underestimation of the actual etching rate during this period, given the fact that an argon/oxygen plasma synergistically enhances the etching of an amorphous carbon surface through physical and chemical sputtering.[51–54] For the timescales considered here, the modification of the DAC layer during the oxygen pulse is expected to be considerably greater than the modification of the bulk photoresist layer. The second assumption is supported by previous modeling work that included a soft layer in addition to the graphitic layer when describing modification to PMMA under ion bombardment.[55] Additionally, oxygen modification of the DAC layer produces a highly graded layer. Because the optical parameters measured by ellipsometry are representative of the average properties in a graded layer, we assume that this layer has a refractive index that is less than that of the parent DAC layer but greater than that of the bulk photoresist.[56] For simplicity, we also assume that the extinction coefficient of the oxygenated DAC layer is negligible.

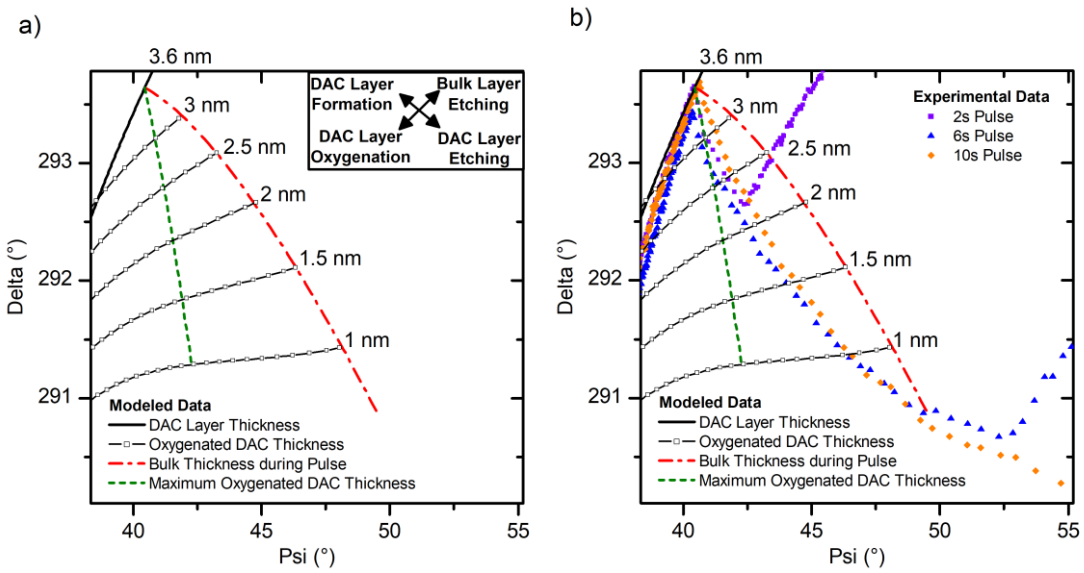

Figure 2.7. (a) Ellipsometric model used for describing the evolution of the DAC layer during an oxygen pulse. Each data point to the left of the bulk thickness line represents a 0.4 nm increment of the oxygenated DAC layer thickness. (Inset) Significance of the directionality in the ellipsometric model (b) Overlay of the experimental data on the model.

To ensure that the model is physically consistent, we also calculated a limit for the maximum potential oxygenated DAC layer thickness that can be achieved through a modification of the parent DAC layer. This limit is based on the concept of conservation of optical density, which is the product of the refractive index and thickness of the DAC layer. As Schwarz-Selinger et al. showed, the refractive index is proportional to the density of an amorphous carbon film.[35] Thus. the conservation of optical density is consistent with a conservation of mass. As shown in Fig. 2.7b, overlaying the model on the raw data, we observe that regardless of the oxygen pulse length, approximately the first nanometer of depleted DAC layer is fully converted into a modified, oxygenated DAC layer with a thickness of approximately 1.6 nm. Further depletion of the DAC layer is also accompanied by a decrease in the oxygenated DAC layer thickness as the oxygenated DAC layer reaches steady state

and then begins to be etched. Once the oxygen pulse begins to dissipate, we observe a sharp interruption in the DAC layer depletion, and an almost immediate reformation and increase in thickness of the layer. From the modeling work and experimental characterization, we have identified a modification mechanism for the DAC layer in the presence of plasma oxygen species that corresponds with the depletion of the layer.

2.4.2 Photoresist Layer Structure

We used the ellipsometric model to extract the time-dependent thickness of each of the dynamic layers in the photoresist structure for each of the various oxygen pulse lengths, as shown in Fig. 2.8.

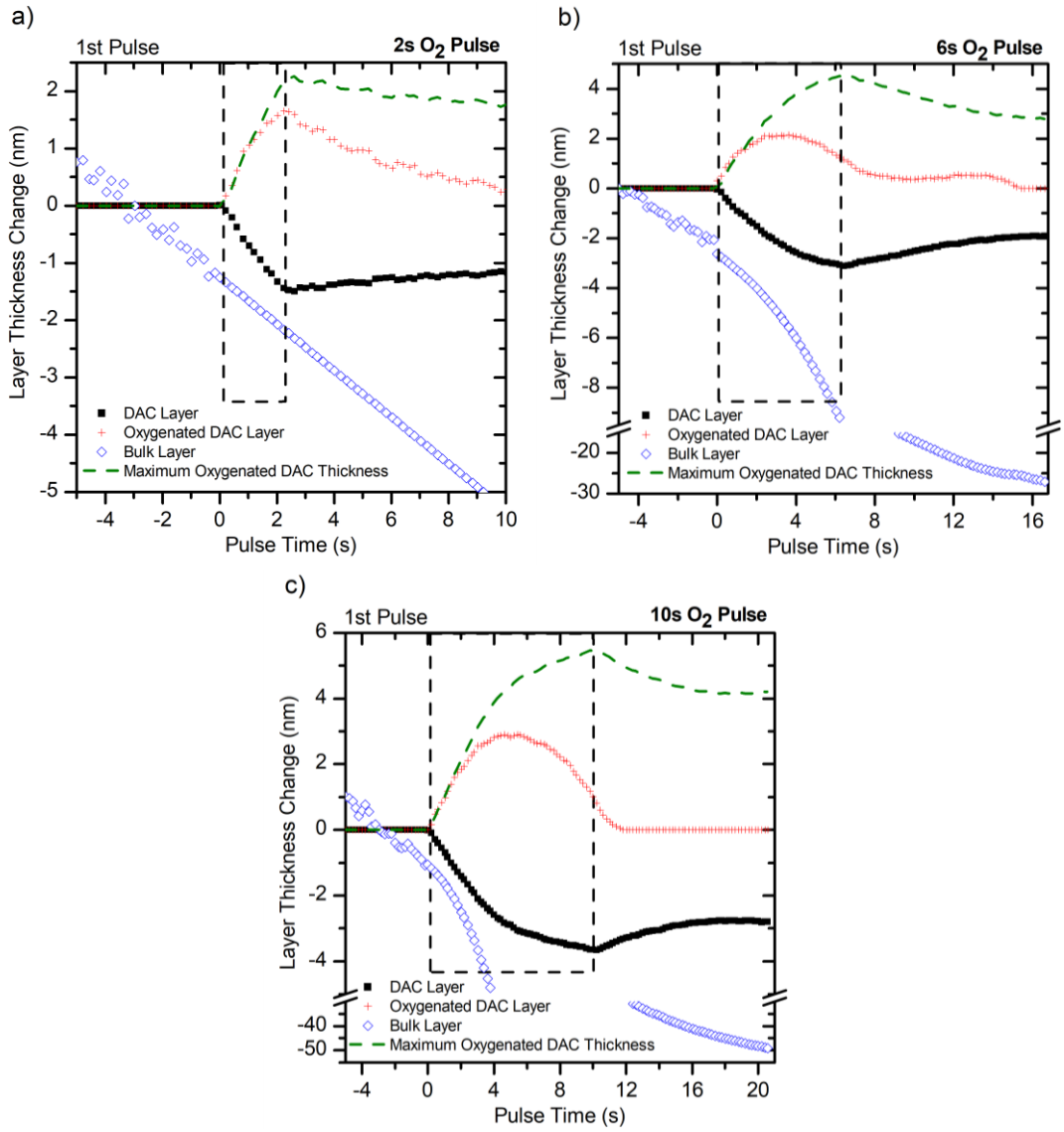

Figure 2.8. Modeled thicknesses of the layers composing the photoresist during oxygen pulses of (a) 2 s, (b) 6 s, and (c) 10 s. The outlined area indicates the period over which oxygen is being input into the system. The dashed line represents the maximum thickness of oxygenated DAC layer if there is a complete conversion of the depleted DAC layer into an oxygenated layer. In (b) and (c), the thickness loss rate of the bulk layer increases rapidly due to the depletion of the DAC layer, resulting in a greater total bulk layer thickness loss over the pulse duration.

Due to the number of dynamic layers during the pulse, we manually fitted the thickness change of the bulk layer during this period to a smooth transition between the calculated thickness prior to and following the pulse. This procedure allowed for

the thickness of the modified and unmodified DAC layers to be modeled explicitly. We identified three distinct behaviors that occur during the oxygen pulse. First, as oxygen is introduced into the chamber, the thickness of the oxygenated DAC layer develops concurrently with the depletion of the DAC layer. The partially-hydrogenated photoresist-derived DAC layer depletes more slowly than non-hydrogenated, amorphous carbon films.[57] Second, once the oxygen pulse is terminated, the oxygenated DAC layer begins to be etched away concurrently with a reformation of the DAC layer. Upon the resumption of an argon plasma-dominant ion bombardment regime, the oxygenated DAC layer is preferentially etched relative to the unmodified DAC layer, because the higher oxygen content has lower etching resistance.[14,13] Third, the rate of thickness loss of the bulk layer is dependent on the thickness of the DAC layer. For a depletion of the DAC layer of approximately 1.6 nm (Fig. 2.8a), the bulk layer thickness loss rate remains unchanged. However, for the greater depletions of the DAC layer that occur with the 6 s and 10 s pulse lengths (Figs. 2.8b,c), the thickness of the DAC layer is no longer sufficient to mediate the steady-state etching of the bulk layer, and thus the bulk layer is removed at an increasing rate. This relationship between the DAC layer thickness and the bulk layer etch rate can be explained by the ion dose reaching the bulk layer being mitigated by the thickness of the DAC layer, which leads to a reduced sputter yield of the bulk layer.[58,59] Our key conclusion is that the initial thickness loss of the DAC layer occurs as a result of the oxygenation of the layer, which persists only for as long as oxygen is introduced into the system. Once the oxygen dissipates, the oxygenated DAC layer is rapidly depleted, and the DAC layer begins to reform.

2.4.3 DAC Layer/Etch Rate Relationship

We determined the overall photoresist etch rate as a function DAC layer thickness from the time-dependent thickness evolution of the photoresist layer structure, which was the main objective of this study. We illustrate this relationship in Fig. 2.9 for the three tested pulse lengths.

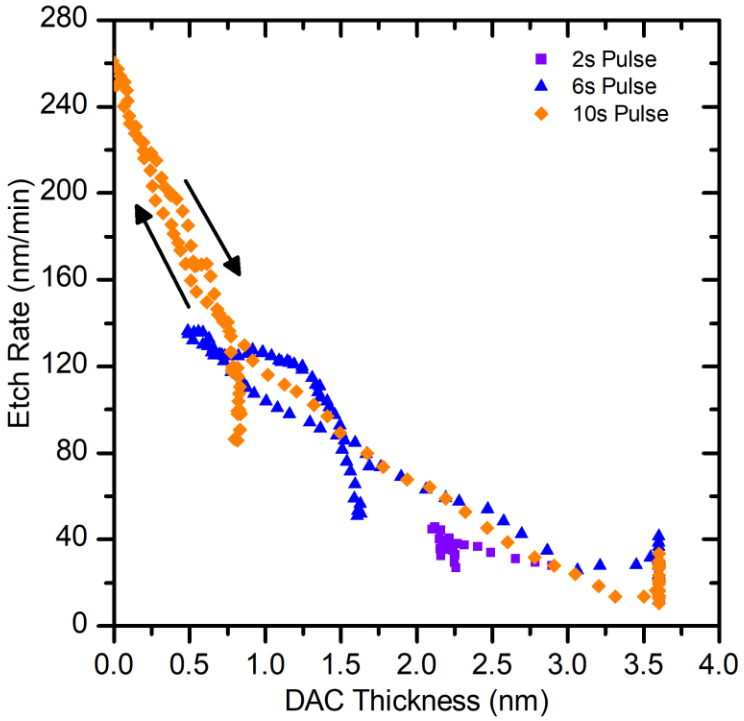

Figure 2.9. Relationship between the PR193 etch rate and the thickness of the DAC layer. Arrows indicate the direction of the trend during the depletion and reformation of the DAC layer.

The key impacts of the DAC layer thickness on the photoresist etch rate become evident based on the duration of the oxygen pulse. For the 2 s pulse length, the depletion of the DAC layer by approximately 1.6 nm does not result in a significant increase in the overall etch rate. The DAC layer remains sufficiently thick that the introduction of oxygen enhances the photoresist etch rate by less than 10 nm/min. In

this condition, there remains a sufficient graphitization of the surface of the photoresist to maintain the etch rate.[60] At the longer pulse lengths, the effect of the thinning DAC layer on the photoresist etch rate becomes much more apparent. Below a DAC layer thickness of 2 nm, the etch rate increases inversely proportional to the DAC thickness. Below a DAC layer thickness of 1 nm, the trend for the etch rate is further enhanced, culminating in a maximum etch rate 260 nm/min upon full depletion of the DAC layer. As the DAC layer reforms after the pulse, the trajectory of the etch rate with increasing DAC layer thickness follows a similar trend to when it is being depleted. The increased or decreased rate of etch rate progression as the DAC layer is nearing depletion or is being formed initially, respectively, implies that the presence of the DAC layer plays a large role in controlling the magnitude of photoresist etching. Correlating the time dependence of the DAC layer thickness and etch rate, as shown in Fig. 2.10, provides information on the relative etch yield of the DAC layer compared to the unmodified bulk layer. Upon initiation of high-energy ion bombardment, the etch rate is elevated as the corresponding etch yield of the surface layers is enhanced due to the volatilization of oxygen and hydrogen in the polymer structure. As the DAC layer thickness approaches steady-state, the etch rate sharply decreases and attains a steady-state threshold as the etch yield of the DAC layer decreases not only due to the dehydrogenation and crosslinking, which occurs in this layer, but also because the ion penetration depth in the modified layer is less than that in the unmodified bulk layer.[61] At the surface of the DAC layer, dangling bonds predominate the structure. Upon the introduction of oxygen into the plasma, the etch yield of the DAC layer is enhanced by the oxygen reacting with the dangling bonds

and forming a sputtering product. However, from the reduced penetration depth of ions in the DAC layer, up to a 1.6 nm depletion of this layer does not cause the etch rate of the total layer structure to increase appreciably. The ability of the remaining approximately 2 nm thick DAC layer to maintain an etch yield that is significantly lower than that of the bulk layer, and thus can to maintain the overall steady-state etch rate, is supported by findings from MD simulations and other experimental work.[42,61,62]

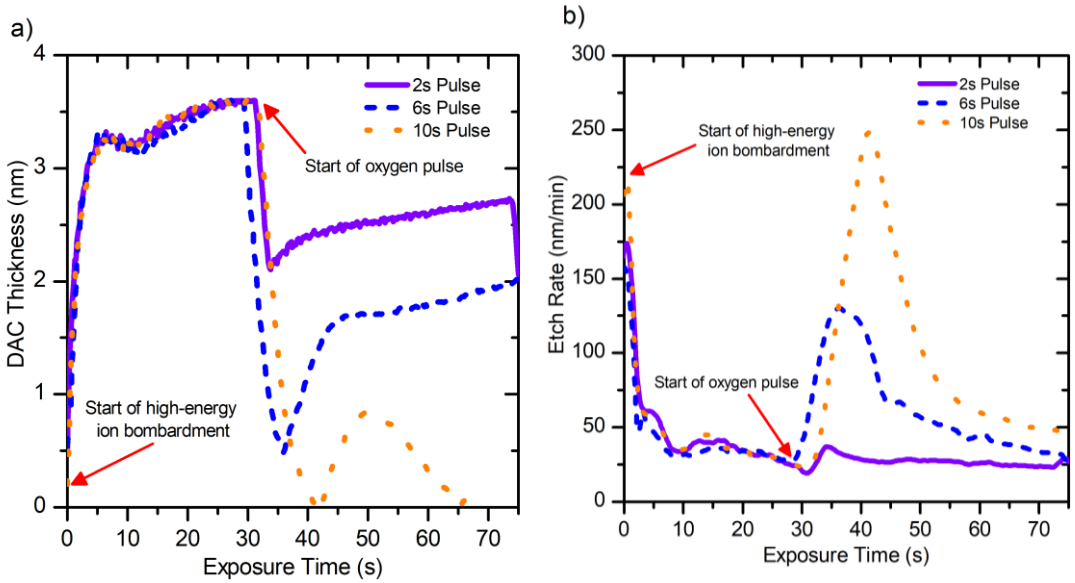

Figure 2.10. Evolution of (a) the DAC thickness and (b) the etch rate during the initial formation of the DAC layer from high-energy ion bombardment and depletion from interaction with oxygen in the plasma. The initial high etch rate as the DAC layer is forming correlates with an enhanced etch yield of the surface layer as primarily oxygen and hydrogen is volatilized. Upon attainment of a steady-state DAC layer thickness, the etch rate is sharply reduced due to the DAC layer having an etch yield that is much lower than that of the bulk layer.

We corroborated the etching behavior of the photoresist by using OES to interpret the DAC layer etching behavior from the perspective of the plasma condition. Figures 2.11a and 2.11b depict the relationship between the ratio of

monatomic oxygen to argon in the plasma versus the etch rate and DAC layer thickness, respectively. We believe that the increasing hysteresis with pulse time for both properties arises from the following mechanism. The initial presence of oxygen in the plasma primarily reduces the thickness of the DAC layer, but the overall etch rate remains stable as the thickness of the DAC layer remains above approximately 2 nm. For the 6 s and 10 s oxygen pulse lengths, a greater relative amount of oxygen is present in the plasma, resulting in an enhanced depletion of the DAC layer, which also corresponds to an increasing etch rate. Upon the termination of the oxygen pulse, the monoatomic oxygen fraction stabilizes. The oxygen fraction only begins to decrease as it is pumped out of the chamber, in an interval that is determined by the chamber residence time. As the oxygen residence time at the given processing condition is approximately 2 s, we observe the post-pulse effects on the DAC layer thickness and etch rate after an initial rapid decrease in the atomic oxygen fraction. In this region, the sharp decline of the atomic oxygen fraction results in the reestablishment of regime that is dominated by argon ion bombardment, which leads to the reformation of the DAC layer and a corresponding decrease in the etch rate.

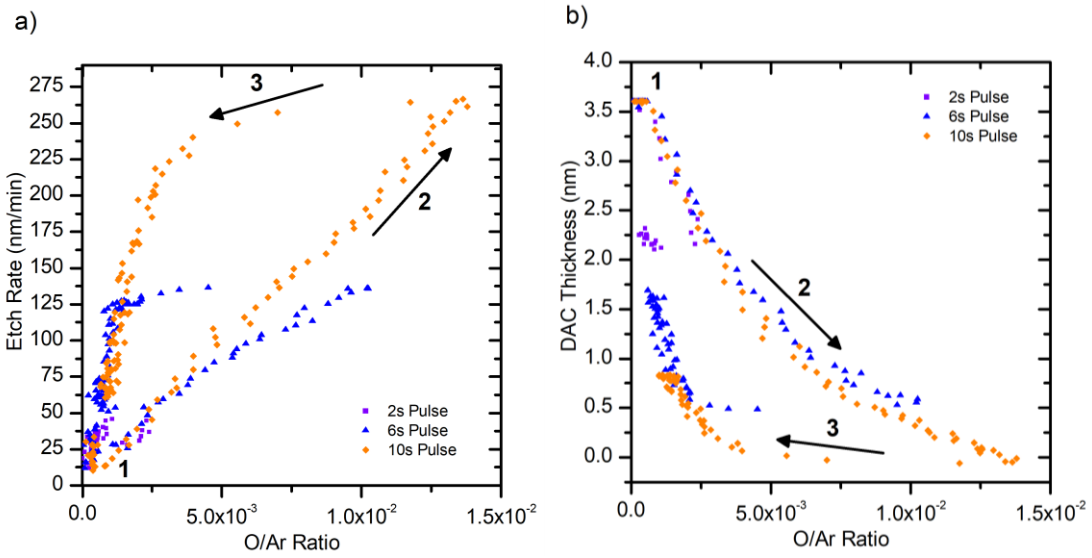

Figure 2.11. Relationship between (a) the PR193 etch rate and (b) the thickness of the DAC layer as a function of the oxygen-to-argon ratio during pulsing, as measured via OES.

1. Beginning of pulse partially depletes DAC layer, but etch rate remains stable
2. Continuation of pulse further depletes DAC layer, resulting in a sharp increase in the etch rate
3. Completion of pulse results in decrease in oxygen/argon ratio, allowing DAC layer to reform which is accompanied by a sharp decrease in the etch rate

The smaller hysteresis in the etch rate versus DAC layer thickness relationship (Fig. 2.9) compared to the etch rate versus oxygen-to-argon ratio indicates that the etch rate is primarily controlled by the thickness of the DAC layer.

The key conclusion from this analysis is that a threshold DAC layer thickness of approximately 2 nm is required to maintain a stable etch rate of the PR193 photoresist. As long as there is sufficient oxygen in the plasma, depletion of the DAC layer proceeds, resulting in a sharp increase in the photoresist etch rate when the layer is depleted beyond the threshold thickness. From the narrower hysteresis in the relationship between the etch rate versus the DAC layer thickness compared to the relationship between the etch rate versus the atomic oxygen fraction, we conclude

that the etch rate is primarily controlled by the thickness of the DAC layer, rather than the amount of oxygen that is present in the gas phase.

2.5 Summary and Conclusions

In this work, we developed an ellipsometric model to interpret the role of the DAC layer on the photoresist layer structure and overall etch rate. Under an argon plasma with a maximum ion energy of 125 eV, a distinct and reproducible DAC layer with a steady-state thickness of approximately 3.6 nm forms on the surface of the photoresist. At the steady-state condition, the etch rate of the photoresist is maintained at a value of approximately 30 nm/min. Upon introduction of oxygen into the plasma, the surface of the DAC layer becomes oxygen rich, resulting in a greater susceptibility to etching. Depletion of the DAC layer occurs via the incorporation of oxygen into the layer, which is then etched away.

A partial depletion of the DAC layer, up to a remaining thickness of approximately 2 nm, is sufficient to maintain the steady-state etch rate. Further depletion of the layer causes a sharp increase in the etch rate, as the DAC layer can no longer sufficiently mediate the etching of the underlying bulk photoresist layer.

The initial formation of the DAC layer induces stresses within the surface of the photoresist which leads to surface roughening. Because the stress is relaxed upon the formation of roughness, the depletion of the DAC layer from the oxygen pulse does not impact the magnitude of the observed roughness. Reformation of the DAC layer after the oxygen pulse introduces additional stresses which enhance the magnitude of surface roughening.

Overall, we benchmarked the DAC layer properties and the etching behavior for a PR193-type photoresist under varying sets of plasma parameters. A further extension of this will work will involve benchmarking the etching behavior of additional photoresists and polymers to develop a model that can connect the DAC layer properties, etching behavior, and chemical composition of the processed materials. This comprehensive model, along with the current work, will allow us to understand the etching behavior of new photoresist materials that are currently in development to achieve sub-10 nm feature sizes using new lithographic techniques.[6]

Acknowledgements

The authors would like to thank Dr. Dominik Metzler, Andrew Knoll, Chen Li, Pingshan Luan, Steven Hong, Dr. A. S. Mullin, Dr. D. E. Falvey, and Dr. J. S. Petersen for helpful insights and discussions on this project. The authors gratefully acknowledge financial support of this work by the National Science Foundation (CMMI-1449309) and US Department of Energy Office of Fusion Energy Sciences (DE-SC0001939).

Chapter 3: Evolution of Photoresist Layer Structure and Surface Morphology under Fluorocarbon-Based Plasma Exposure

Adam Pranda[1], Sandra Abigail Gutierrez Razo[2], John T. Fourkas[2,3,4], and Gottlieb S. Oehrlein[1]

[1]Department of Materials Science and Engineering and Institute for Research in Electronics and Applied Physics, University of Maryland, College Park, Maryland 20742

[2]Department of Chemistry and Biochemistry, University of Maryland, College Park, Maryland 20742

[3]Institute for Physical Science and Technology, University of Maryland, College Park, Maryland 20742

[4]Center for Nanophysics and Advanced Materials, University of Maryland, College Park, Maryland 20742

A. Pranda performed all the experimental work and analysis in this chapter. The other authors assisted with collaborative discussion of the supporting ideas behind the work in this chapter.

Abstract

Ion bombardment of photoresist materials during plasma etching results in the formation of a surface dense amorphous carbon (DAC) layer that contributes to both etch resistance and the development of surface roughness. Real-time ellipsometric measurements/analysis reveals that a C_4F_8-containing plasma interacts with an Ar-plasma-formed DAC layer to produce a modified DAC/fluorocarbon (FC) layer by FC deposition/diffusion of fluorine into the surface. The depletion of the DAC layer via modification and ion bombardment causes the etch rate of the bulk layer to increase. As the modified surface layer is formed, a noticeable decrease in surface roughness is observed. These findings provide an understanding of the mechanisms of atomic layer etching processes in photoresist materials.

3.1 Introduction

Two of the key requirements for reproducible, high fidelity, photoresist-based pattern transfer are high etch resistance and low surface and line-edge roughness. For typical photoresist materials, such as PR193, the presence of ion bombardment during plasma exposure has a significant correlation with both the etch resistance and roughness. Sufficiently energetic ion bombardment forms a dense amorphous carbon (DAC) layer on the sample surface, as a result of the depletion of oxygen, hydrogen, and volatile-product-forming species.[11,23,36] This depletion results in the surface layer becoming significantly denser than the underlying bulk material, resulting in an enhancement of the etch resistance.[3,31,63] However, as the DAC layer grows from the underlying bulk layer, the increase in density introduces compressive stresses within the surface layers, causing a buckling instability that can lead to the enhancement of

surface roughness.[19] Therefore, the tradeoff between enhancement of etch resistance and degradation of feature fidelity due to surface roughness needs to be considered carefully when processing photoresist materials under energetic plasma conditions.

The addition of reactive gases, such as octafluorocyclobutane (C_4F_8), to the plasma composition during pattern transfer is necessary to facilitate sufficient etching selectivity between the photoresist and SiO_2 or Si_3N_4. However, maintaining a controlled and consistent etching selectivity depends on the stability of the etch resistance of the photoresist material. For a 193 nm photoresist exposed to energetic plasmas, the etch resistance is proportional to the developed thickness of the surface DAC layer.[63,58–60] However, the DAC layer is susceptible to chemical sputtering from reactive plasmas, which depletes the layer and decreases the etch resistance.[5,52,53,64] For this reason, it is imperative to understand the impact of reactive gases on the DAC layer in conditions representative of a pattern transfer process, particularly with regards to the potential implications for process stability and reproducibility.

The main goal of the work presented here is to evaluate the impact of a reactive plasma composition containing C_4F_8 on the photoresist surface characteristics, such as the DAC layer thickness, layer structure, and surface roughness, and the resulting etching behavior. By altering the ion energy and the duration of the C_4F_8 exposure, we are able to perform discrete evaluation of the impacts of the chemical reactivity of the C_4F_8 and the physical sputtering from ion bombardment on the evolution of the surface characteristics and etching behavior.

3.2 Experimental Section

The samples used in this study were 200 nm thick blanket films of 193 nm photoresist material (PR193) produced by the Japan Synthetic Rubber Corporation (JSR); these films have been characterized extensively in previous works.[23,63,20] The 193 nm photoresist consists of a terpolymer structure with a polymethylmethacrylate (PMMA)-based backbone with leaving, lactone, and polar groups serving as the functionalized side groups.[7]

Plasma processing of the samples was performed using an inductively coupled plasma (ICP) reactor that has a spiral antenna on top of a quartz dielectric located 13 cm above a Si electrode with a diameter of 12.5 cm. The top antenna was operated at an excitation frequency of 13.56 MHz and the substrate was biased at a radio frequency (RF) of 3.7 MHz. Water cooling of the substrate backside maintained a substrate temperature of 10 °C during processing.

Plasma processing was performed at a chamber pressure of 10 mTorr and a source power of 300 W for all experiments. The chamber gas consisted of Ar at a flow rate of 40 sccm and C_4F_8 at a flow rate of 2.7 sccm for all experiments. This C_4F_8 flow rate was chosen such that the differential pressure between the Ar and C_4F_8 flow rates into the chamber was minimized, ensuring a smooth flow of C_4F_8 into the chamber during the pulsed operation. Figure 3.1 is a schematic process diagram for the experimental setup.

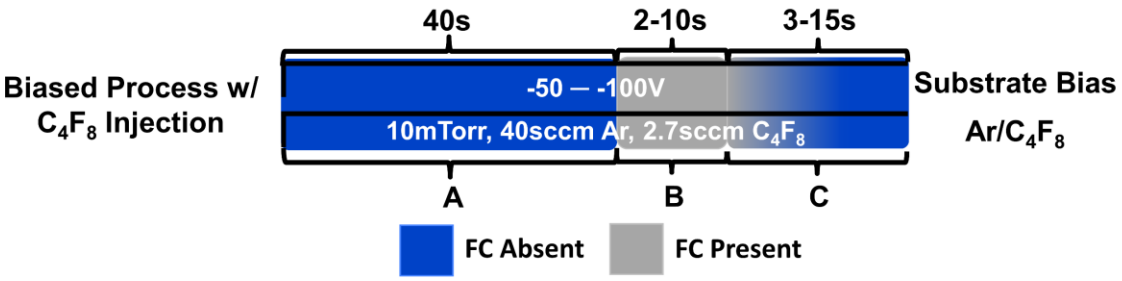

Figure 3.1. Process diagram for the experimental setup. Segment A: Prolonged bias time under an FC absent position, which allows for the development of a prominent DAC layer. Segment B: C_4F_8 injection and resulting modification and etching of the DAC layer. Segment C: Evacuation of residual C_4F_8 in chamber leading to reformation of the DAC layer.

Each experiment consisted of two distinct operating modes, a FC-absent regime and a FC-present regime. At the outset of each experiment, only argon with an applied substrate bias of -50 V, -75 V, or -100 V was supplied for 40 s, to facilitate the formation of a well-defined, steady-state DAC layer. As the plasma potential is approximately 25 V at the chosen processing conditions, the corresponding maximum ion energy at the sample surface is 75 eV, 100 eV, and 125 eV, respectively at the chosen applied substrate biases. After 40 s, C_4F_8 was injected into the plasma chamber for 2 s, 6 s, or 10 s. The injection of C_4F_8 into the plasma chamber was precisely controlled using LabView software to open and close the gas valves at the specific times. Upon completion of the pulse, the residual C_4F_8 was evacuated from the chamber within 3-15 s, depending on the pulse length. For experiments in which the ion energy was varied, the C_4F_8 injection times were held constant at 10 s, whereas for experiments with varied injection times, the applied substrate bias was held constant at -100 V.

In situ ellipsometry was employed to obtain information about the thickness and refractive index of the photoresist samples. The ellipsometer was set up in a

polarizer-rotating compensator-sample-analyzer configuration using a wavelength of 632.8 nm. Interpretation of the ellipsometric raw data, parameterized via the optical constants psi and delta, was performed using an optical model that takes into account surface modification from ion bombardment as well as interactions with the reactive FC species.

Ellipsometry is the key characterization tool for probing the layer structure of the photoresist sample. Any changes in the thickness and/or refractive index of the layers that make up the photoresist sample are manifested as deviations in the trajectory of the raw ellipsometric data. Figure 3.2 shows the relevant deviations in the ellipsometric data that motivate the analysis for this study. The initial deviation from high energy ion bombardment is associated with the formation of the DAC layer. Through the control of the magnitude of substrate biasing or duration of C_4F_8 injection, we can use differences in the ellipsometric data trajectory to visualize both the prominence of the initially formed DAC layer and the subsequent modification and etching of this layer as a result of the C_4F_8 interaction. Interpretation of this data through an ellipsometric model, which is supported by secondary characterization techniques, yields quantitative information about the thickness evolution of the photoresist layer structure.

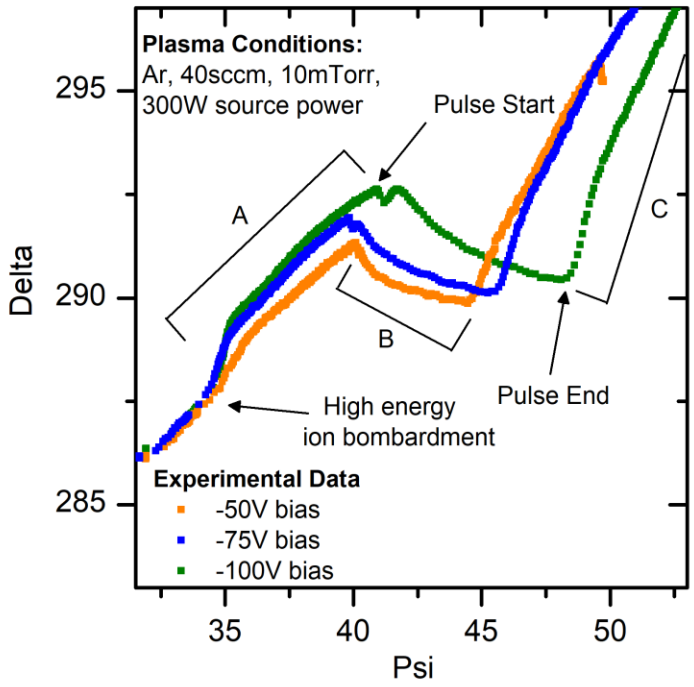

Figure 3.2. Observed deviations in the raw ellipsometric data. The regions marked A, B, and C represent the deviations originating from the corresponding regions in the process diagram shown in Fig. 3.1.

The secondary characterization techniques employed in this study were X-ray photoelectron spectroscopy (XPS) and atomic force microscopy (AFM). XPS analysis, which was used to verify the surface chemistry evolution, was performed using a Vacuum Generators ESCA Mk II surface analysis chamber with a non-monochromatized Al Kα X-ray source (1486.6 eV). The instrument was operated in a constant-energy analyzer mode with a 20 eV pass energy. Emission angles of both 20° and 90° were used to probe the surface and near surface regions as well as for determination of the thickness of a modified surface layer using angle-resolved XPS analysis. All samples were delivered for XPS analysis using a vacuum transfer system to prevent any interaction with ambient atmospheric species. AFM analysis was

performed using a Veeco Multimode instrument with a scan size of 2 μm × 2 μm and a resolution of 512 × 512 pixels. The surface roughness of the samples was defined as the root mean square (RMS) of the surface height data.

3.3 Results and Discussion

3.3.1 Ellipsometry

To interpret the real-time surface modification in appropriate detail, our ellipsometric model analyzes both the general modification behavior that occurs over the duration of the entire experiment and the specific modification mechanisms that occur when C_4F_8 interacts with the sample surface.

3.3.1.1 Baseline Model of Surface Modification

The fundamental details of our baseline ellipsometric model have been discussed extensively in our previous work.[63] The components of the model, which correspond to the directionality of the raw data in psi-delta space, are depicted in Fig. 3.3a. Briefly, our baseline model treats the bulk layer of the photoresist and the developed surface DAC layer that arises from ion bombardment as separate entities. The evolution of these layers, specifically the formation and etching of the DAC layer and the etching of the bulk layer, each has its own characteristic directionality in psi-delta space, due to sufficiently distinct refractive indices. This distinction allows for the construction of the ellipsometric map as shown in Fig. 3.3a. Overlaying the raw experimental data on top of this map, as shown in Fig. 3.3b, allows for the visual interpretation of the magnitude of the surface modification from the plasma exposure. For example, in the shown case with various substrate biases, there is a greater observed deviation when high energy ion bombardment is introduced at greater

substrate biases, due to the formation of a DAC layer with a greater thickness. The greater the substrate bias the greater the acceleration of the ions, yielding a greater ion energy and thereby increasing the penetration depth of the ions into the material.

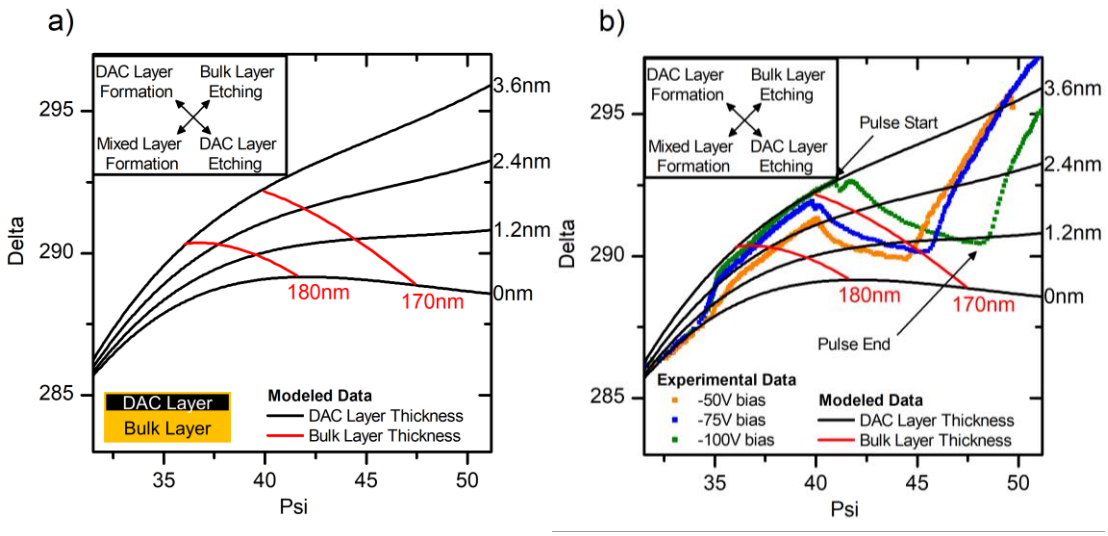

Figure 3.3. (a) Interpretation of the directionality in the ellipsometric data based on a two-layer model. (Inset) Schematic of the modeled photoresist layer structure. (b) Raw data overlaid on the ellipsometric model.

The argon ions scission bonds of hydrogen and oxygen atoms within the penetration depth, thus generating a discrete DAC layer that is distinct from the underlying bulk material.[42,12] The ion penetration depth, and thus the resulting thickness of the DAC layer, ranges from approximately 3.6 nm at -100 V substrate bias to 3 nm at -50 V substrate bias for the PR193 material. This range is based on simulations using the Stopping Range of Ions in Matter (SRIM) software package, as well as on previous experimental results.[43,44] Additionally, the magnitude of substrate bias proportionally controls the etch rate. Therefore, for the equivalent Ar-only processing time of 40 s, there is less etching of the bulk layer in the -50 V bias condition relative to the -75 V and -100 V conditions.

Upon introduction of the C_4F_8 pulse, we initially observe a selective depletion of the DAC layer thickness. Once the DAC layer has been thinned by a certain amount, there is a corresponding decrease in the bulk layer thickness. This reactive etching of the DAC layer is consistent with prior works, in which selective depletion of the DAC layer was observed under either a reactive oxygen or FC plasma environment.[63,64,5,48] However, based on the directionality of the ellipsometric data, the interaction of the C_4F_8 with the DAC layer does not purely reduce the thickness of the DAC layer, but also induces another surface modification that has a directionality opposite to that of bulk layer etching. We believe that this modification is caused by the diffusion of fluorine into the DAC layer, which results in the observed change in the measured optical properties. More specific details of the modeling of this interaction are discussed in the next section. Under all conditions, once the reactive C_4F_8 gas is evacuated from the system, the resumption of Ar-dominated ion bombardment results in the reformation of the DAC layer and reestablishment of the normal regime of bulk layer etching.

3.3.1.2 Surface Interaction with C_4F_8

At ion energies below 50 eV, FC groups from the C_4F_8 deposit on the sample surface, forming a FC polymer layer.[25,27,65] This polymer layer has optical properties that are distinct from those of the DAC layer. Thus, the presence of the polymer layer is indicated by a distinct trajectory in the ellipsometric data. However, we did not observe an ellipsometric profile that is representative of a deposited FC layer. This finding is consistent with our experimental setup, because the substrate bias is applied for the entire duration of each experiment with a magnitude range (50 V-100 V) that

prevents any appreciable buildup of an FC layer; the corresponding ion energies (75 eV to 125 eV) cause any deposited FC film to immediately be removed from the surface. In determining the most likely nature of the C_4F_8 interaction with the photoresist surface, we propose the ellipsometric model shown in Fig. 3.4a.

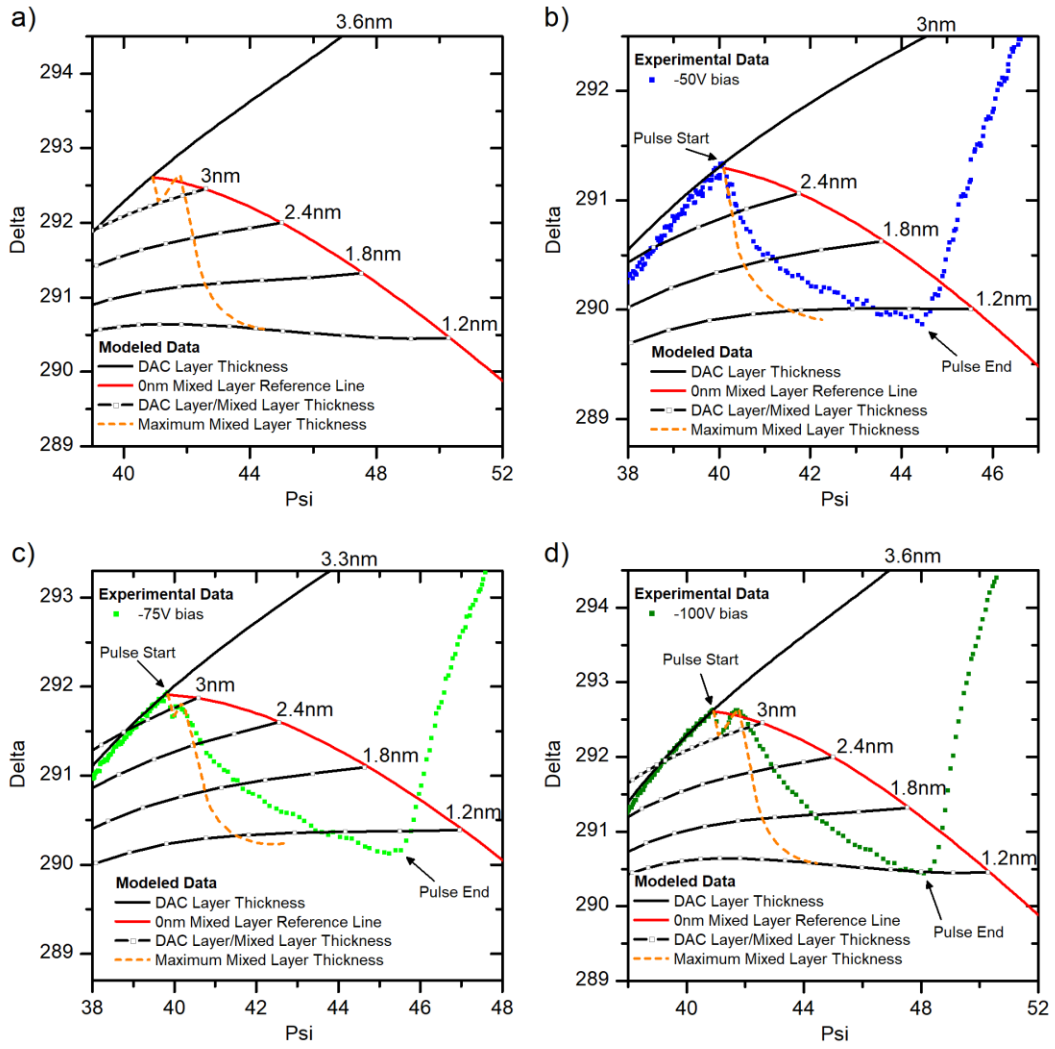

Figure 3.4. (a) Ellipsometric model for the period in which the FC interacts with the PR193. Overlays of the raw data on the model for (b) -50 V, (c) -75 V, and (d) -100 V substrate bias conditions. DAC thickness loss without any concurrent modification of the layer would cause the raw data to follow the 0 nm reference line, whereas complete thickness DAC thickness loss as a result of conversion into a mixed layer corresponds to the “maximum mixed layer thickness” line. Each data point to the left of the 0 nm reference line corresponds to an increment in the mixed layer thickness of 1 nm.

Because the deviation in the ellipsometric trajectory during the C_4F_8 pulse is not consistent with FC layer buildup and also cannot be justified with a growth in the thickness of the bulk layer, as suggested by our baseline model in Fig. 3.3b, we hypothesize that a modification mechanism must exist that alters the measured optical properties of the reacted surface layer. Indeed, in fitting our experimental data we found that a plausible modification is fluorine from the FC groups diffusing into the DAC layer, thus altering its optical properties such that they are intermediate between those of a steady-state DAC layer and a discrete FC film. The mixing of fluorine within the surface layers to form a modified layer has been observed in numerous studies with both inorganic (SiO_2, Si_3N_4) and organic (PR193, PR248, PMMA) surface compositions.[4,27,65,66] A similar modification mechanism has also been observed with an oxygen plasma in our prior work; the model setup from that work motivated the model setup for the current work.[63] Due to the complexity of the surface interaction with C_4F_8, we made the following assumptions in establishing the ellipsometric model. (1) The etch rate of the bulk layer remains continuous between the start and end of the C_4F_8 pulse. This assumption is necessary to limit the number of dynamic variables and focus our analysis on the surface region. (2) The refractive index of the modified layer was fixed at a value less than that of the DAC layer but greater than that of a pristine FC layer. This assumption is supported by experimental work that found the fluorination of a photoresist surface to decrease the refractive index of the surface layer.[4,26,67] (3) There is an upper bound for the maximum thickness of the modified layer that can be achieved via the modification of the initial DAC layer. The purpose of this limit was to ensure that the model is physically

consistent. The limit is based on the concept of conservation of optical density, which is the product of the refractive index and thickness of the DAC layer. The conservation of optical density is consistent with a conservation of mass for the DAC layer as it has been shown that the refractive index of an amorphous carbon film is proportional to its density.[35]

Using this model, we can deduce the following behaviors of the photoresist interaction with the C_4F_8. At low substrate biases of -50 V and -75 V, shown in Fig. 3.4b-c, the initial 0.5 nm to 1 nm thickness loss of the DAC layer can be attributed to conversion of the DAC layer into a modified DAC/FC layer. After this region of initial conversion, further thickness loss of the DAC layer is attributed to etching of the DAC layer without any further modification from C_4F_8 interaction. Due to the oxygen-poor nature of the DAC layer, the fluorination of the surface assists in the removal of carbon atoms that are not bonded to oxygen[16]. At these magnitudes of substrate bias, reactive sputtering is partially suppressed due to the surface deposition of FC groups.[68–70] In both cases, the modified layer develops a maximum thickness between 1.6 to 2 nm. Once the C_4F_8 pulse is terminated, the modified layer is rapidly etched away, and the DAC layer begins to reform. The -100 V substrate bias condition, Figure 3.3d, follows a similar progression, with one notable difference being the presence of a transient region immediately after the initial C_4F_8 pulse injection that results in a delay of approximately 1 to 1.5 s before the DAC layer thickness starts to decrease from the reaction with the C_4F_8.

A 0.5 s transient region is also present in the -75 V substrate bias condition. As the duration of this transient region is proportional to the substrate bias voltage,

one possible origin of this transient effect is the interaction between the bias electric field and the C_4F_8, which we have observed to lead to a brief increase in the applied substrate bias voltage. An increase in the bias voltage likely promotes an increase or temporary stabilization in the DAC layer thickness in the presence of reactive C_4F_8 gas.[71] At the same time, the small percentage of C_4F_8 that is introduced into the plasma composition has a small impact on the ion current density. [25,72,73] However, based on Langmuir probe measurements, the introduction of C_4F_8 results in an initial reduction in the electron density, and corresponding ion density, of as much as 3×10^{10} cm^{-3}.[74] As a result of all these changes to the electrical properties, upon the introduction of C_4F_8, the initial impact on the surface from ion bombardment diminishes and the impact from chemical modification from the deposited FC groups becomes more prominent. Once the C_4F_8 pulse injection stabilizes electrically and the deposited FC starts to volatilize, the thickness of the DAC layer begins to decrease due to the C_4F_8 interaction.

3.3.1.3 Photoresist Layer Structure

Using the ellipsometric model, the temporal evolution of each of the layers that make up the photoresist structure was extracted, as shown in Fig. 3.5. For all three substrate bias cases (Fig. 3.5a-c), the evolution of the layers followed the same trend, with the quantitative differences arising from the different magnitudes of substrate bias. The key to the evolution of the layer structure is the fluorination of the surface. Upon initiation of the C_4F_8 pulse, there is an immediate small loss of the DAC layer due to the FC groups arriving at the surface.

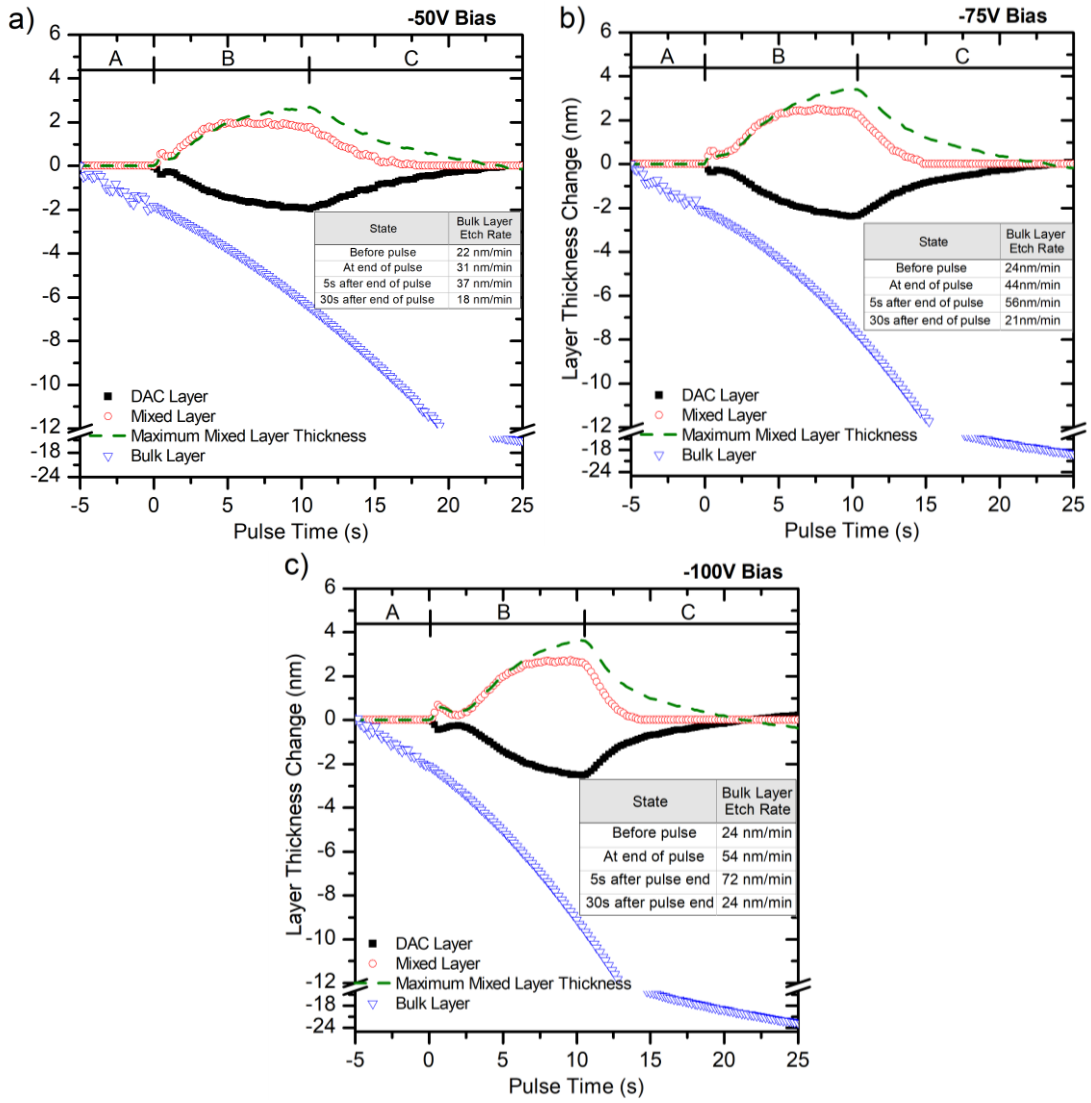

Figure 3.5. Extraction of the individual layer thicknesses during the FC interaction with the PR193 for (a) -50 V, (b) -75 V, and (c) -100 V substrate bias conditions. (Inset) Table of bulk layer etch rates at specified points in the pulse. The bulk layer etch rate increases by the end of the pulse due to the depletion of the DAC layer. After the completion of the pulse, the bulk layer etch rate further increases as a result of the removal of the surface mixed layer and the reformation of the DAC layer. Once the DAC layer reestablishes its steady state, ~30 s after the pulse ends, the bulk layer etch rate is restored to a magnitude comparable to that before the pulse.

The FC groups present in the plasma and deposited on the surface contribute atomic fluorine to the sample surface, which is the main component for initiating surface etching of the DAC layer.[75–77] Atomic fluorine is of added significance in an

~94% Ar/6% C_4F_8 plasma admixture as used in this work, because at this composition the flux of neutral species becomes comparable to the flux of ions. [25,67,78] Ion bombardment of the FC groups at the surface releases atomic fluorine, which begins to reduce the thickness of the DAC layer.[70,79,80]. The initial thinning during the first ~5 s of C_4F_8 exposure is a result of fluorine diffusing into the DAC layer, lowering its refractive index and density, and producing a modified layer at the photoresist surface.[4,81] The etch front of the modified layer propagates deeper into the layer structure. The depth is determined by a balance between available fluorine at the greatest depth of the modified layer, which promotes additional conversion of the DAC layer into the modified layer, and ion bombardment of the surface, which etches the top of the modified layer. [71,80,28,33,82,83] As the magnitude of the substrate bias increases, the modified layer etch front propagates at a faster rate because more fluorine is available from the deposited surface FC groups and can be driven more deeply into the underlayer.[79] The maximum thickness of the modified layer corresponds to the point the concentration of C_4F_8 in the chamber is the greatest, at the end of the pulse duration. This point also corresponds to the smallest thickness of the DAC layer, due to the presence of a reactive etching environment. In all cases, as the thickness of the DAC layer decreases, its ability to passivate the bulk layer likewise decreases, and so the etch rate of the bulk layer increases. Because the DAC layer decreases the ion dose that reaches the underlying bulk layer, a decrease in the passivating thickness leads to an increase in the sputter yield from the bulk layer.[58,59]

Upon the termination of the C_4F_8 pulse, the bulk layer is etched at a faster rate due to the removal of the passivating modified layer and the reformation of the DAC

layer. Once the DAC layer reestablishes its steady state, the etch rate of the bulk layer becomes comparable to the etch rate that was present before the pulse. The evolution of the layer structure seen here is comparable to that observed in our previous work on oxygen interactions with the DAC layer. Reactive plasma species, such as oxygen or C_4F_8, readily modify the DAC layer to form a modified surface layer which then proceeds to reduce the thickness of the DAC layer.[63] The reduction in the DAC layer thickness has a corresponding impact on the bulk layer thickness. The main difference between the oxygen and C_4F_8 gases in impacting the layer structure is that the rate of modification from C_4F_8 is slower than that from oxygen, because the FC deposited on the surface functions as an additional passivating layer that mediates the existing etching interaction between the DAC layer and underlying bulk layer.[75,76,79,80,84]

3.3.2 XPS

The evolution of the C1s peak of the photoresist surface as it undergoes energetic ion bombardment followed by interaction with C_4F_8 is shown in Fig. 3.6. The photoresist sample was scanned in the pristine state, during the energetic steady-state Ar ion bombardment, at the midpoint of the C_4F_8 pulse, and after the conclusion of the pulse. The pristine sample primarily consists of C-C, C-O-C, and O-C=O type bonding, which is consistent with the backbone structure of PR193.[7] Upon initiation of energetic ion bombardment, we observe an elimination of O-C=O type bonding and an increase in C-C type bonding as a result of the formation of the DAC layer on the sample surface. When C_4F_8 is introduced during the pulse, the XPS data indicate the formation of numerous CF_x type species, including CF, CF_2, and CF_3. The

formation of these species is consistent with the findings of numerous other works.[65,27,4,16,82] The peaks corresponding to the CF_x type species are prominent due to the underlying DAC layer being oxygen poor.[85]

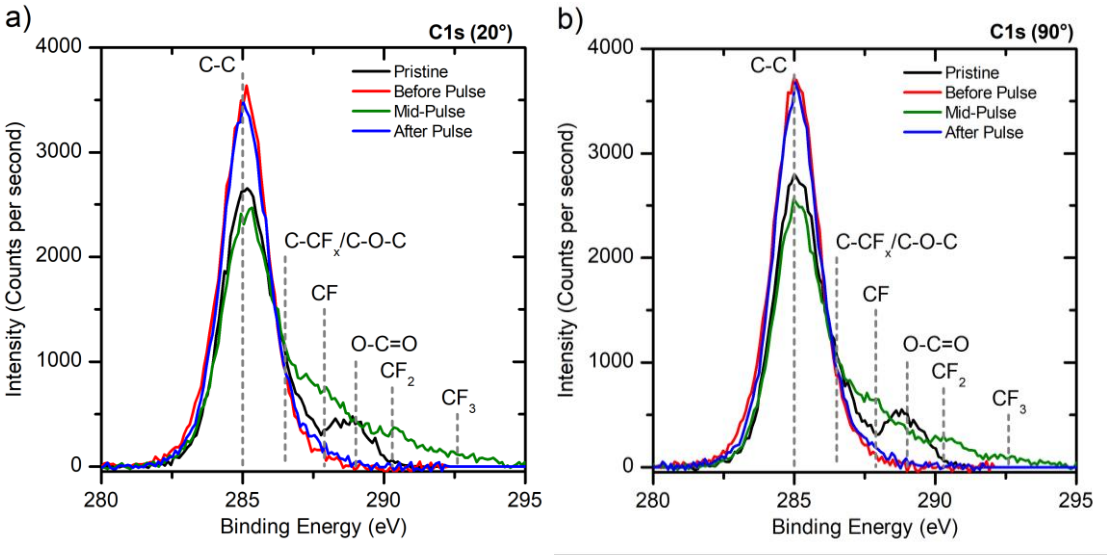

Figure 3.6. XPS data for the C1s peak for a (a) 20° and (b) 90° emission angles at points corresponding to the pristine PR193 sample, prior to the C_4F_8 pulse, at the midpoint of the C_4F_8 pulse, and after the pulse. Ar ion bombardment removes the C-O type species from the pristine sample while the introduction of the C_4F_8 results in the formation of CF_x species on the sample surface. Once the C_4F_8 pulse is terminated, ion bombardment removes the CF_x species from the surface.

We used an angle-resolved XPS analysis technique to estimate the thickness of the modified layer to be approximately between 1 to 3 nm.[86] This thickness range for a modified FC layer is consistent with that observed in other works.[64,73,87] When the C_4F_8 is evacuated from the chamber upon completion of the pulse, the peaks corresponding to the CF_x species disappear as the modified layer is etched from the surface. The concurrent reformation of the DAC layer is also evident from the fact that the peak shape of the after-pulse condition is identical to that of the before-pulse condition when the steady-state DAC layer is formed. Through the XPS analysis, we provided support for our ellipsometric model by both confirming the presence of a

FC-rich surface layer and quantifying the depth of the FC species that define the maximum thickness of the modified surface layer.

3.3.3 AFM

3.3.3.1 Influence of Ion Energy

Understanding the surface roughening behavior of the photoresist during C_4F_8 interaction is critical for applications involving photoresist materials. To gauge the evolution of the surface roughness, we evaluated the surface roughness at the representative points indicated in the ellipsometric map in Fig. 3.7 at applied substrate bias voltages of -50 V, -75 V, and -100 V (75 eV, 100 eV, 125 eV ion energies). For this analysis, we chose points corresponding to immediately before and after the initiation of the C_4F_8 pulse to evaluate the immediate impact of the C_4F_8 on the steady-state DAC layer. At the points immediately preceding the start of the pulse, we consistently observe that the magnitude of the RMS roughness scales proportionally with the magnitude of the applied substrate bias.[19,7,17,88–90] As the substrate bias increases, a greater ion energy is dissipated within the surface layers, which leads to a more prominent buckling instability that gives rise to surface roughening.[19]

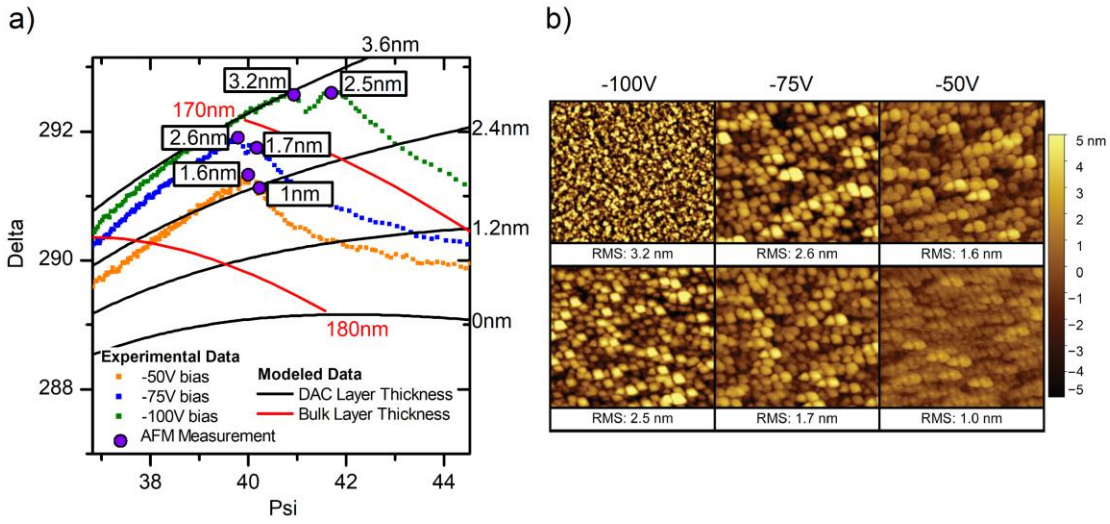

Figure 3.7. (a) Ellipsometric map with representative points indicating where the samples were evaluated using AFM. The numbers in the boxes correspond to the RMS roughnesses in the corresponding AFM images. (b) Corresponding AFM scans of the PR193 samples. In all cases, the initial C_4F_8 interaction with the PR193 results in a smoothening of the sample surface.

The key finding in the results shown in Fig. 3.7 is the ability of the C_4F_8 pulse to affect an appreciable reduction in the RMS roughness after only a brief interaction with the photoresist surface. Typically, when photoresist materials are exposed to plasma discharges containing a continuous flow of C_4F_8, the surface roughness has been found to increase with processing time and amount of material etched. [4,16,17] However, a key difference between these studies and our work is that in the other works, the C_4F_8 was introduced from the outset of the plasma exposure, whereas in our work we introduced the C_4F_8 after 40 s of Ar-only exposure. Our initial Ar-only exposure allows for the formation of a prominent DAC layer. Supplying C_4F_8 from the outset of an experiment prevents the formation of any DAC layer, as any DAC formed readily react with, and be etched away by, the FC. Therefore, in our experiments other mechanisms are responsible for the smoothing the photoresist

surface. One possibility is that a reduction in the magnitude of compressive stress as the DAC layer thins from the interaction with C_4F_8. For example, a DAC layer with a thickness of approximately 1.1 nm has a compressive stress that is 10% less than that of a DAC layer with a thickness of approximately 2.0 nm.[19] Similarly, the elastic modulus of the fluorinated surface layer, if we assume it to be comparable to polytetrafluoroethylene (PTFE), is one to two orders of magnitude less than that of the DAC layer.[91,92] The significantly lower elastic modulus of the fluorinated layer relative to the underlying DAC layer is a potential reason for the reduction in surface roughness. Another possibility is that the introduction and diffusion of FC groups into the rough DAC layer surface produces a locally high concentration of FC polymer, which may prefer to occupy the voids in the rough surface profile, thus smoothing the surface. This hypothesis is based on the observation that high concentrations of C_4F_8 (>50 %) result in a deposition behavior that can lead to a reduction in the RMS roughness.[89,93] These ideas are in agreement with our observed results. Overall, the concept of being able to reduce the surface roughness of surfaces via a reactive gas with depositing chemistry has significant implications for applications, such as pattern transfer, for which controlling roughness profiles is essential for feature fidelity.

3.3.3.2 Influence of Fluorocarbon Concentration

In addition to evaluating the impact of ion energy on the surface roughness, we sought to determine the longevity of the smoothing effect and its relation to the presence of FC species on the sample surface. The left panel of Fig. 3.8 depicts the representative points on the ellipsometric map at which AFM scans were taken, and

the right panel shows the corresponding images. In this experiment, the substrate bias voltage was fixed at -100 V (125 eV maximum ion energy) and C_4F_8 pulse durations of 2 s, 6 s, and 10 s were tested to alter the concentration of FC at the photoresist surface.

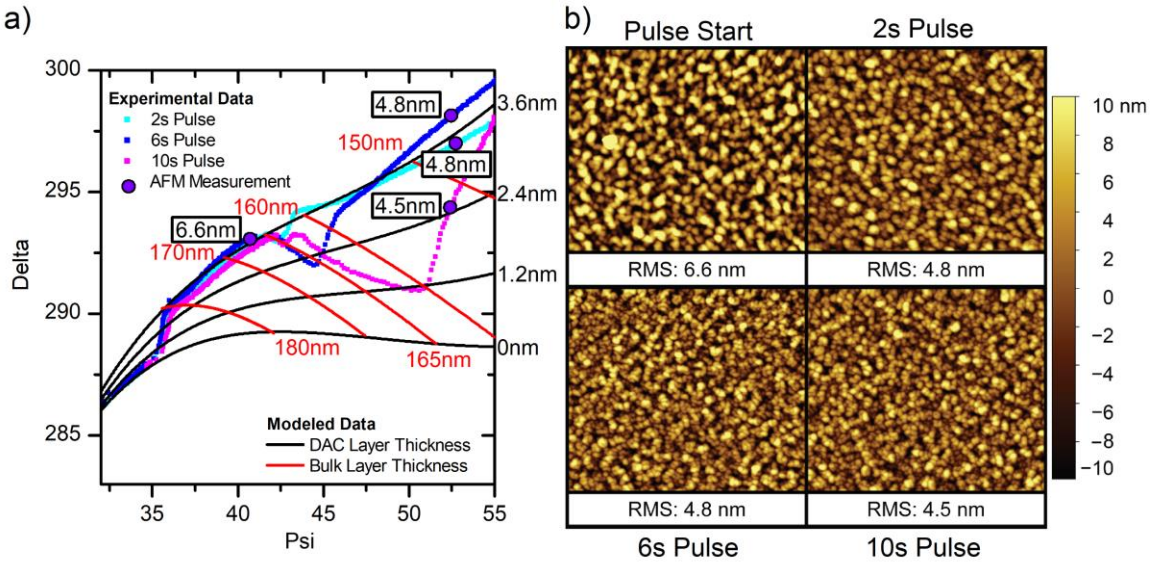

Figure 3.8. (a) Ellipsometric map with representative points indicating where the samples were evaluated using AFM. (b) Corresponding AFM scans of the PR193 samples. For all pulse lengths with the same magnitude of substrate bias, once the C_4F_8 pulse dissipates, the surface roughness associated with the reformation of the DAC layer is comparable in all cases.

A reference point was chosen before the start of the C_4F_8 pulse to determine the initial roughness prior to any C_4F_8 interaction. Points were then chosen at a similar amount of thickness etched after the completion of the various pulse durations to determine if the pulse duration has any residual impact on the surface roughness once the modified layer is removed. As shown in Fig. 3.8, although the surface after the C_4F_8 pulse did exhibit a lower RMS roughness than before the pulse for all pulse durations, the magnitude of the RMS roughness did not differ as a result of a longer C_4F_8 pulse duration. These results suggest that the modified layer is so thin that the

initial roughness mitigation that it provides upon initiation of the C_4F_8 pulse is rapidly countered by the roughness that is reintroduced as a result of the reformation of the DAC layer. However, in the case of 2 s and 6 s pulse durations, the AFM measurement corresponds to a point at which the DAC layer has reestablished a steady state. Thus, in these cases the prior C_4F_8 interaction does have an effect in reducing the surface roughness even once all the FC is etched away from the surface. The lower surface roughness after the pulse, where more material has been etched, relative to the greater surface roughness before the pulse, indicates that the transient C_4F_8/surface interaction can reduce the surface roughness even for later points in the plasma process.[16,17] The ability to reduce and/or stabilize the surface roughness during a plasma process involving C_4F_8 is potentially advantageous for cyclic processes such as atomic layer etching, in which roughness control is essential for preserving feature fidelity.

3.4 Conclusion

In this work, we evaluated the impact of a pulsed C_4F_8 injection onto a PR193 photoresist material with a well-established DAC layer. We determined the influence of the FC on the evolution of the photoresist layer structure, the surface chemistry, and the surface morphology. The thickness of the initial DAC layers varies between 3 nm at a -50 V bias to 3.6 nm at a -100 V bias. Upon introduction of the C_4F_8 pulse, the surface of the DAC layer is converted into a FC-rich modified layer that has properties intermediate between those of the parent DAC layer and a pristine FC film. As the FC species on the surface volatilize, a combination of further chemical conversion and physical sputtering reduces the thickness of the DAC layer.

Concurrently, the reduction in the DAC layer thickness coincides with an increase in the etch rate of the underlying bulk material. Once the C_4F_8 pulse is terminated, the modified layer is rapidly removed, and the bulk layer etch rate is reduced once a steady-state DAC layer is reestablished.

At all the substrate bias voltages tested, the magnitude of surface roughness is reduced immediately after the introduction of the C_4F_8. Although the magnitude of the substrate bias affects the magnitude of the surface roughness from C_4F_8 interaction, the duration of the C_4F_8 pulse does not. However, even after full removal of FC species from the surface, the surface roughness after the pulse is smaller than the roughness prior to the start of the pulse.

The goal of this work was to identify the interaction behavior between a PR193-type photoresist and a FC-containing plasma under conditions in which the surface had already developed a DAC layer due to ion bombardment. In future work we will incorporate the knowledge gained from these analyses to evaluate photoresist materials under experimental setups that are more conventional in pattern-transfer applications. In particular, we will investigate the behavior of existing and in-development photoresist materials under continuous wave and atomic layer etching processes to ascertain their viability for pattern-transfer applications.

Acknowledgements

The authors would like to thank Dr. Andrew Knoll, Dr. Pingshan Luan, Chen Li, Kang-Yi Lin, Alex Jennion, Dr. A. S. Mullin, Dr. D. E. Falvey, and Dr. J. S. Petersen for helpful insights and discussions on this project. The authors gratefully acknowledge financial support of this work by the National Science Foundation

(CMMI-1449309) and US Department of Energy Office of Fusion Energy Sciences (DE-SC0001939).

Chapter 4: Significance of Plasma-Photoresist Interactions for Atomic Layer Etching (ALE) Processes with Extreme Ultraviolet (EUV) Photoresist

Adam Pranda[1], Kang-Yi Lin[1], Sebastian Engelmann[2], Robert Bruce[2],

Eric A. Joseph[2], Dominik Metzler[2], and Gottlieb S. Oehrlein[1]

[1]Department of Materials Science and Engineering and Institute for Research in Electronics and Applied Physics, University of Maryland, College Park, Maryland 20742

[2]IBM T. J. Watson Research Center, Yorktown Heights, New York 10598

[3] IBM Semiconductor Technology Research, Albany, New York 12203

A. Pranda performed all the experimental work and analysis in this chapter. The other authors significantly assisted with the experimental and data analysis approach. The materials for this work were provided by IBM.

Draft manuscript, to be submitted

Abstract

Extreme ultraviolet (EUV) lithography has emerged as the next generational step in advancing the manufacturing of increasingly complex semiconductor devices. The commercial viability of this new lithographic technique requires compatible photoresist (PR) materials that satisfy both the lithographic and etch requirements of good feature resolution, chemical sensitivity, a low line edge roughness (LER), and good critical dimension uniformity (CDU). Achieving the decreased feature pitches of modern processing nodes via EUV lithography places a limit on the available photoresist thickness for a pattern transfer process. Therefore, etch processes are required that maximize the etching selectivity of a hard mask material, such as SiO_2, to an EUV photoresist. In this work, we evaluated the ability of an atomic layer etching (ALE) process to maximize the SiO_2/EUV PR etching selectivity. Through the flexible parameter space available in an ALE process, we evaluated the etching behaviors as a function of the ALE parameters of ion energy, etch step length (ESL), fluorocarbon (FC) deposition thickness, and precursor gas type. We find that the interaction between energetic argon ion bombardment and a deposited FC layer produces a modified surface layer on the PR that can strongly control the PR etch rate and even produce an etch stop under some conditions. Under the same processing conditions, the etching behavior of SiO_2 continues unimpeded, thus resulting in a high overall SiO_2/PR etching selectivity. Secondary characterization using x-ray photoelectron spectroscopy (XPS) and atomic force microscopy (AFM) was used to support the conclusions derived from the ellipsometric modeling based on the surface chemistry evolution and determine the impact of the ALE process on the surface

roughness of the EUV PR, respectively. Additionally, attenuated total reflection Fourier-transform infrared (ATR-FTIR) spectroscopy was used to track the impact on specific functional groups within the PR composition from both the argon ion bombardment and FC deposition components of the ALE process. The ALE-based PR etching concept established in this work serves as a foundation for both the understanding of the impacts of an ALE process on an EUV PR material and for future work employing an ALE process for PR-based pattern transfer.

4.1 Introduction

Semiconductor devices are becoming increasingly more complex to manufacture, both in the lithographic steps, with constantly increasing feature densities, and in the pattern transfer steps, in which highly selective etch processes are required in order to produce multilayer, multicomponent structures with high-aspect-ratio features. One of the key reasons why EUV lithography has emerged as an alternative to the current state-of-the-art 193 nm immersion lithography is an overall streamlining of the lithographic process. To produce feature densities which are characteristic of the 10 nm or 7 nm processing nodes using ArF lithography requires multiple patterning steps such as double, quadruple, and even octuple patterning.[94] Although these techniques enable the fabrication of more complex devices with established 193 nm deep ultraviolet (DUV) lithography, the requirement of multiple patterning steps increases fabrication time, cost, and complexity. The most significant consequence of these drawbacks is a low production yield. For the same cost, EUV lithography can halve the number of patterning steps for existing devices and makes it viable to pursue processing nodes beyond 7 nm.[95] However, despite this advantage,

several key technical challenges remain for EUV processing. One major challenge is termed the RLS (resolution, LER, sensitivity) tradeoff, due to the difficulty of simultaneously obtaining all three parameters.[96–98] At the heart of this tradeoff is the compatibility of the PR material with the fabrication wavelength. The main issue with PR materials for EUV lithography has been the low sensitivity of the chemical response to EUV photons, which is necessary in order to pattern features.[96,99] Not only is the absorbance of EUV photons significantly lower than that of DUV photons in PR materials, but current EUV sources cannot produce the same photon density for a given dose.[98,100] A consequence of the reduced absorbance is nonuniform crosslinking within the PR material, which results in poor LER. [99,101] However, recent advances in both PR materials and higher power EUV sources, which increase the dose received by the PR material, have sufficiently improved the RLS tradeoff to make EUV lithography commercially viable.[102]

Critically, though, the fabrication of semiconductor devices also requires the ability to transfer the lithographically patterned features into a substrate material via a plasma etch process. Thus, an EUV-compatible PR material must have a high etch resistance relative to the substrate material and the ability to preserve the fidelity of the patterned features, namely the LER and CDU, under a plasma exposure. In this area, a key constraint of EUV PR-based pattern transfer is that the available PR thickness is often limited to under 50 nm due to physical constraints, such as preventing pattern collapse or minimizing profile variation in subsequent pattern steps, and to enable integration with feature-dense processing nodes, which require thin layers.[103–105] Due to this thickness limitation, a highly selective etch process is

required in order to minimize the amount of PR loss relative to the substrate material, such as SiO_2. This selectivity is especially important for the patterning of high aspect ratio features. Traditional continuous wave (CW) pattern transfer processes with a reactive gas chemistry, such as Ar/C_4F_8, are not ideal for high SiO_2/PR etching selectivity, due to the susceptibility of PR to etching under this condition, which involves a reactive plasma composition with energetic ion bombardment.[93] Managing the PR etch rate while simultaneously having a plasma condition that is favorable for etching of substrate materials, such as SiO_2 or Si-containing anti-reflection coatings in trilayer stacks, requires selective time-dependent control of plasma parameters, such as the plasma composition and ion energy. For this reason, an ALE process is a good candidate for an EUV PR-based pattern transfer process, as an ALE process provides a flexible parameter space via a cyclic FC passivation layer deposition followed by energetic ion bombardment that can potentially mitigate PR loss while proceeding with SiO_2 etching.[27,29,106,107] Compared to a CW process, an ALE process permits for the decoupling of the synergistic effect between reactive species and ion bombardment, allowing for both components to be controlled individually for better etching selectivity. In this manner, the thickness limitation of EUV PRs can be overcome while also enabling a highly selective etch for the pattern transfer of high-aspect-ratio features.[21,108,109]

In this work, we evaluate the impact of several key ALE processing parameters, namely the ion energy, etch step length (ESL), FC deposition thickness, and precursor gas composition, on the relative etching behaviors of a model EUV PR and SiO_2. Sample characterization via ellipsometry, AFM, XPS, and ATR-FTIR

spectroscopy provides information on the interaction of the EUV PR with the ALE process in terms of the surface modification and etching behavior, surface morphology evolution, and chemical composition impacts, respectively. The results of this work provide a foundational understanding of the application of ALE processes on EUV PRs for the purposes of pattern transfer.

4.2 Experimental Setup

The samples used in this work consisted of separate blanket films of a model EUV PR and SiO_2. The model EUV PR films had a thickness of approximately 56 nm and a polymer backbone formulation that consists of polyhydroxystyrene-methyladamantyl methacrylate (PHOST-MAdMA) as shown in Fig. 4.1. The model EUV PR was a full formulation that also contained a triphenylsulfonium nonaflate photoacid generator and base quencher consisting of 2,4,5-triphenylimidazole. The as-received PR films were also fully exposed with ultraviolet light. This model EUV PR formulation was used as it had identical etching behavior to that of a proprietary commercial EUV PR, while also having a known composition for our chemical characterization work. The SiO_2 films had a thickness of 70 nm.

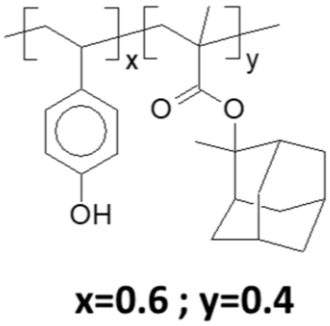

Figure 4.1. Molecular structure and chemical composition of the polymer backbone of the model EUV PR.

Plasma processing of the samples was performed using an inductively coupled plasma (ICP) reactor. The chamber setup consists of a spiral antenna on a quartz dielectric that is located 13 cm above a 12.5 cm diameter Si electrode. The top

antenna is operated at an excitation frequency of 13.56 MHz and the substrate is biased at a radio frequency (RF) of 3.7 MHz. The temperature of the substrate was maintained at 10 °C via water-cooling on the substrate backside.

Figure 4.2 outlines the ALE process used here. For all experiments, the chamber pressure was kept at 10mTorr, an argon carrier gas with a fixed flow rate of 50 sccm was used, and the source power was kept at 200 W. Two different FC precursor gases were evaluated, octafluorocyclobutane (C_4F_8) and trifluoromethane (CHF_3). The flow rate of the FC precursor gases for experiments with C_4F_8 and CHF_3 was 2.2 sccm and 6 sccm, respectively. The difference in flow rates was designed to produce equivalent FC deposition thicknesses between the two different precursors. Table 4.1 lists the key components of the ALE process that were investigated as part of this work.

Table 4.1. Definition of the key ALE parameters in the process setup. Several of the parameters were varied in order to evaluate the impact on the SiO_2/PR etching selectivity.

Step	Processing Parameter	Value
A	FC Deposition Thickness	~0.5nm, ~1nm
B	FC Purge Length	12s
C	Substrate Bias Voltage	20-40V (35-55eV)
D	Etch Step Length	6s, 10s, 18s

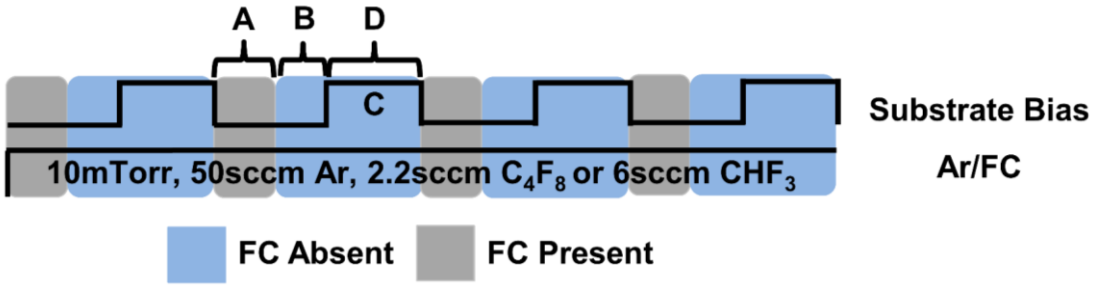

Figure 4.2. Schematic of the ALE process setup. The meaning of each lettered region is given in Table 4.1.

The ALE process follows the framework established by prior works and consists of the following components[27,28,74]: At the start of a cycle, there is first an injection of the precursor gas into the chamber, which deposits an FC layer on the sample surface (A). Next comes a 12 s purging step to evacuate any residual FC precursor from the chamber (B). Next, the substrate biasing is activated (C) to increase the ion energy of the incident argon ions during the etching step (D). Upon the conclusion of the etching step, the substrate bias is removed, and the FC deposition step of the next cycle begins after a one-second delay to prevent any overlap with the energetic ion bombardment of the etching step. As part of this work, the substrate bias voltage/ion energy, etch step length, and FC deposition thickness were systematically varied in order to analyze their relative impacts on the model EUV PR and SiO_2 etching behaviors.

An understanding of the surface modification and etching behavior was obtained by using real-time *in situ* ellipsometry. The ellipsometer was setup in the polarizer-rotating compensator-sample-analyzer configuration at a wavelength of 632.8 nm. The raw data generated from the ellipsometric scan, parameterized through the optical constants psi and delta, was interpreted via an optical model that allowed for distinguishing the extent of surface modification and etching throughout the duration of the ALE process.

After sample processing, information about the surface morphology and surface chemical composition was obtained via AFM, XPS, and ATR-FTIR analysis, respectively. The XPS analysis was performed using a Vacuum Generators ESCA Mk II surface analysis chamber with a non-monochromatized Al Kα X-ray source

(1486.6 eV). The instrument was operated in a constant-energy analyzer mode with a 20 eV pass energy. Electron take-off angles of 20° and 90° were evaluated to probe the chemical evolution of the sample surface. The probing depths of the 20° and 90° scan angles are approximately 2 nm and 8 nm, respectively.[86] The spectra for the C 1s peak were fit using C-C, C-CF_x/C-O-C, CF, O-C=O, CF_2, and CF_3 peaks at 285 eV, 286.5 eV, 287.9 eV, 289 eV, 290.3 eV, and 292.6 eV, respectively.[15] All plasma processed samples were delivered for XPS analysis using a vacuum transfer system to prevent any interaction with ambient atmospheric species. AFM analysis was performed using an Asylum Research MFP3D instrument in the tapping mode configuration with a fixed scan size of 10 µm × 10 µm. Surface roughness information from these scans was quantified by calculating the root mean square (RMS) roughness of the surface profile. The ATR-FTIR analysis was configured based on the previous work done by Luan et al.[110] The FTIR setup consisted of a Shimadzu IRTracer-100 equipped with a HgCdTe (MCT) detector and variable-angle single-reflection ATR accessory with a Ge crystal. The incident light angle at the Ge crystal was set to 60°. The use of an ATR accessory in combination with a Ge crystal probes the sample surface down to a depth of approximately 500 nm, which in the case of the model EUV PR samples results in chemical information being acquired from the whole 126 nm combined thickness of the model EUV PR film and SiO_2 substrate. A ZnSe polarizer was installed on the optical inlet of the ATR accessory to select p-polarization of the incident IR light. IR spectra were acquired and averaged over 20 scans between 3400 cm^{-1} and 600 cm^{-1} with a resolution of 4 cm^{-1}.

4.3 Results

4.3.1 PR Surface Modification from ALE Process

4.3.1.1 Distinctiveness from CW Processes

The motivation behind employing an ALE process for the etch control of the model EUV PR resides in the unique interaction that occurs on the PR surface when compared to traditional CW processes. A comparison of the surface behavior between an ALE process, an inert CW process, and reactive CW process is shown in Fig. 4.3.

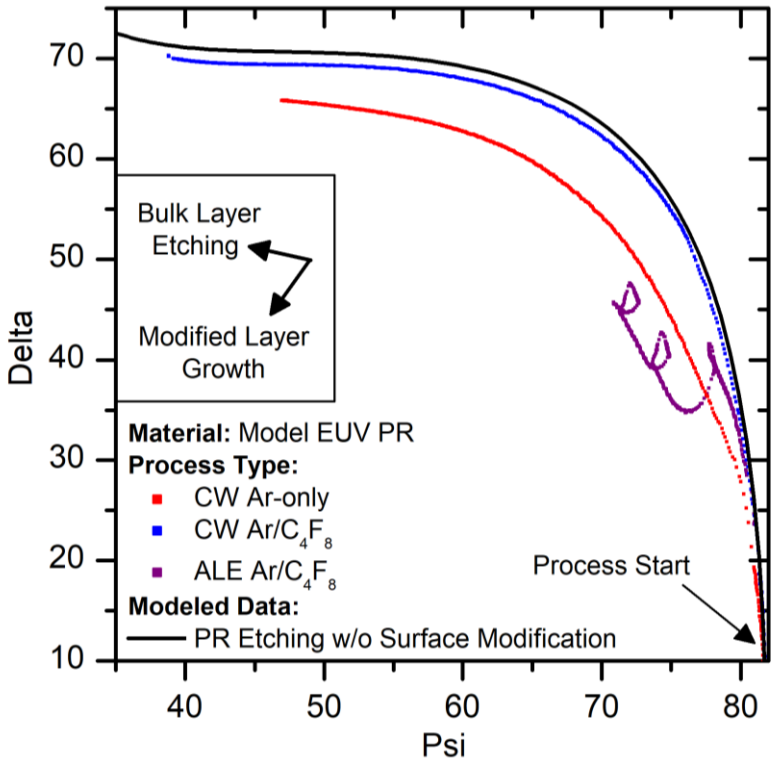

Figure 4.3. Comparison of the Model EUV PR etching behavior under equivalent duration CW Ar-only (40 V bias), CW Ar/C_4F_8 (40 V bias), and ALE Ar/C_4F_8 (100 V bias) plasma processes. The inset compass describes the physical significance of the directionality of the ellipsometric data. Energetic Ar ion bombardment forms a modified surface layer that enhances the etch resistance of the PR. A CW Ar/C_4F_8 results in the greatest amount of etching due to the continuous flux of reactive species, which prevents the modified layer from forming, as well as the high bias voltage, which is required to prevent FC accumulation on the surface. An ALE Ar/C_4F_8 produces yields a high degree of PR etch resistance due to the prominence of the established modified layer from the cyclic interaction of energetic Ar ions with the deposited FC films.

The data for the various process types is shown for an equivalent processing time. Both the CW Ar-only and ALE Ar/C_4F_8 process were performed under a 40V substrate bias while a higher bias of 100V was used for the CW Ar/C_4F_8 process, both in order to overcome the accumulation of a FC layer on the surface, which restricts etching of the PR material, and because this is a typical accelerating voltage that is used in pattern transfer applications. A baseline Ar-only process develops a modified surface layer in the form of a dense amorphous carbon (DAC) layer that mitigates the PR etch rate.[63] This behavior is in contrast to a CW Ar/C_4F_8 process in which the reactive FC species restrict the formation of the modified surface layer, and thus the PR is susceptible to a greater amount of etching. An ALE process presents a novel approach to controlled PR etching, as the Ar process with cyclic deposition and biased etching of a deposited FC layer produces a more prominent modified layer relative to either CW process case, which yields the least amount of PR etching over the equivalent process time. Comparing the CW Ar-only and ALE cases over longer durations, as shown in Fig. 4.4a, illustrates that the modified layer in an ALE process is maintained throughout the process duration and remains more prominent than the modified layer produced by the CW Ar-only process. Furthermore, as the modified layer in the ALE process saturates, the corresponding amount of PR etching is almost completely halted before proceeding at a greatly reduced rate. The differences in the chemical composition of the modified layer, Fig. 4.4b, and emphasized in the difference spectra, Fig. 4.4c, show that the modified layer in the CW Ar-only case is dominated by C-C bonding, consistent with the presence of a DAC layer, whereas the modified layer produced by the ALE process is more abundant in CF and CF_2-bonded

type species. Tracking the evolution of the surface chemistry throughout the ALE process in Fig. 4.4d, with the difference spectra in Fig. 4.4e, shows that the composition of the modified layer becomes increasingly abundant in CF, CF_2, and CF_3 bonded species and less abundant in C-C bonded species as the number of ALE cycles increases.

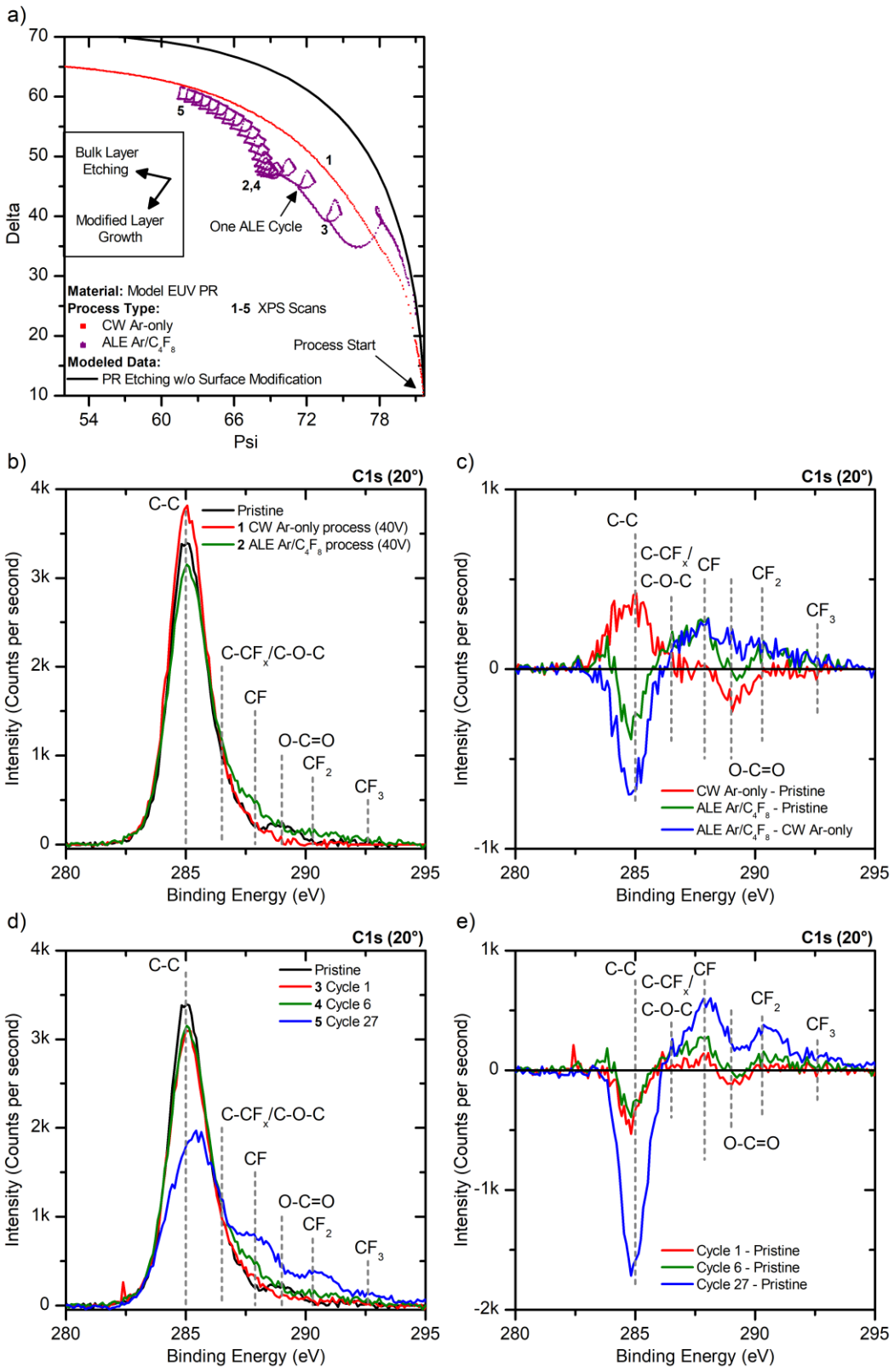
a)
Delta
Psi
Bulk Layer Etching
Modified Layer Growth
One ALE Cycle
Material: Model EUV PR
Process Type:
CW Ar-only
ALE Ar/C4F8
1-5 XPS Scans
Process Start
Modeled Data:
PR Etching w/o Surface Modification
b)
C1s (20°)
Intensity (Counts per second)
Binding Energy (eV)
Pristine
1 CW Ar-only process (40V)
2 ALE Ar/C4F8 process (40V)
C-C
C-CFx/C-O-C
CF
O-C=O
CF2
CF3
c)
C1s (20°)
C-C
C-CFx/
C-O-C
CF
CF2
CF3
O-C=O
CW Ar-only - Pristine
ALE Ar/C4F8 - Pristine
ALE Ar/C4F8 - CW Ar-only
d)
C1s (20°)
Pristine
3 Cycle 1
4 Cycle 6
5 Cycle 27
e)
C1s (20°)
Cycle 1 - Pristine
Cycle 6 - Pristine
Cycle 27 - Pristine

Figure 4.4. Comparison of the ellipsometric PR surface response during a CW Ar-only and an ALE Ar/C_4F_8 process. The indicated numbers represent the corresponding points and process types of the XPS scans in (b) and (d) that were taken. Corresponding XPS absolute (b) and difference (c) spectra for the CW Ar-only and ALE Ar/C_4F_8 process. These spectra support the concept that the etch-inhibiting modified layer in a CW Ar-only process is primarily a graphitic layer with predominantly C-C bonding, whereas the more prominent modified layer in a ALE Ar/C_4F_8 process contains CF, CF_2, and CF_3 bonded species in addition to the C-C bonding. XPS absolute (d) and difference (e) spectra taken at various points in the ALE process. The 6^{th} cycle is representative of the point at which the PR loss is minimized as the modified layer attains its maximum extent. The 27^{th} cycle is representative of a point well beyond the time at which the modified layer is well established. The XPS characterization indicates that the modified layer in an ALE process becomes increasingly abundant in FC species as the number of ALE cycles increases.

4.3.1.2 Interpretation of Surface Modification

Determination of the mechanism that leads to the PR surface modification in an ALE process was pursued by defining an ellipsometric model that is supported by secondary XPS characterization. Based on this setup, the directionality of the ellipsometric data describes the physical significance of the modifications that are occurring on the PR. The psi-delta trajectory, and the significance of this trajectory for a characteristic ALE cycle, in this case the second ALE cycle in the process, are shown in Fig. 4.5a. The supporting XPS characterization in Fig 4.5b,c and Fig. 4.4c,e suggests the presence of a discrete FC layer at the end of the deposition steps in the ALE process, which leads to the formation of a progressively more FC-rich modified layer from the ion bombardment during the etching step.

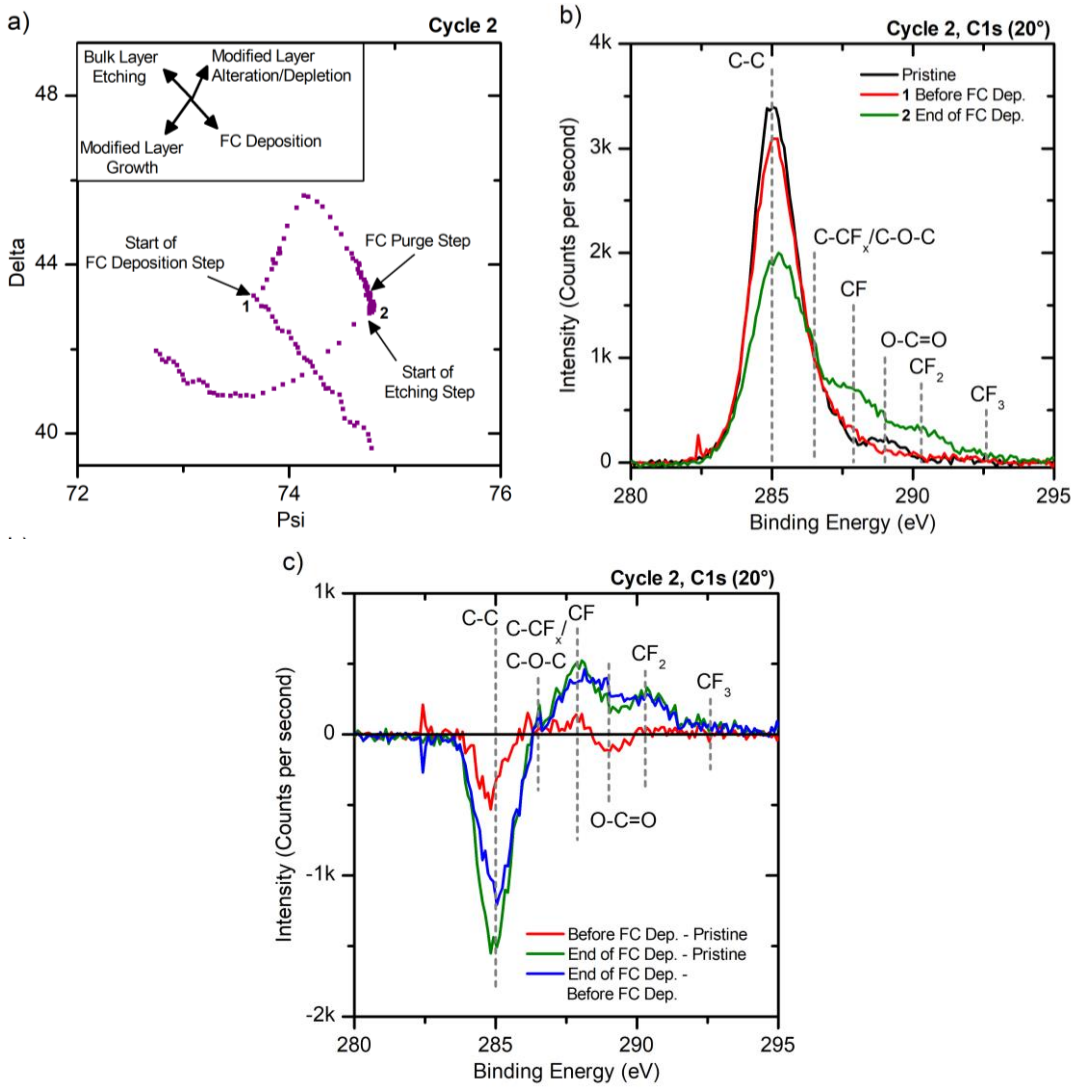

Figure 4.5. (a) Evolution of the ellipsometric PR surface response during an ALE cycle. (Inset) Physical significance of the modifications that are occurring on the PR material, as described by the directionality of the ellipsometric data. The developed modified layer from the preexisting FC deposition and ion bombardment is initially altered by the FC deposition, which begins to accumulate a discrete FC layer on the surface once the initial modification saturates. Upon enabling of energetic ion bombardment for the etching step, the deposited FC layer is converted into a modified layer that is thicker than the one present at the beginning of the cycle. The growth of the modified layer is a critical component in limiting the amount of the bulk layer that is lost during each ALE cycle. The indicated numbers represent the corresponding points and process types at which the XPS scans in (b) were taken. (b) Supporting XPS characterization, which correlates the surface chemistry to the events indicated by the ellipsometric data in Cycle 2. (c) Difference XPS spectra of the conditions analyzed in (b)

The directionality of the ellipsometric data suggests the following mechanism, which leads to the surface modification and corresponding etch control of the PR material in an ALE process. Prior to the beginning of the deposition step, the interaction between the argon ion bombardment and deposited FC layer from the preceding cycles establishes the initial formation of a modified layer on the PR surface, as can be seen in Fig. 4.4a from the second cycle onwards. Furthermore, etching of the bulk layer takes place. Upon the initiation of the FC deposition step, the surface response, as indicated by the trajectory of the ellipsometry, suggests that there is alteration and/or depletion of the surface modified layer as it interacts with the FC species that are arriving at the surface. During this step, etching of the bulk layer does not take place. Before the FC deposition step concludes, the FC interaction with the modified layer saturates, after which another sharp change in the trajectory of the ellipsometric data indicates the deposition of a discrete FC layer on the surface. This deposited FC layer is stable on the PR surface throughout the conclusion of the FC deposition and purge steps. Upon initiation of substrate biasing during the etching step, the energetic argon ion bombardment results in the concurrent depletion of the FC layer, further growth of the modified layer on the PR surface, and a resumption in the etching of the bulk layer. The growth of the modified layer, however, corresponds with a decrease in the amount of bulk layer that is etched with each subsequent cycle.

4.3.1.3 Impact of ALE Processing Parameters

The impact of the ALE processing parameters on the extent of surface modification and resulting PR etch behavior is shown in Fig. 4.6. For the model EUV PR system, etching of the bulk layer in the absence of any surface modification would

cause the trajectory of the ellipsometric data to follow the line marked “PR Etching w/o Surface Modification.” Any deviation towards the lower left away from this line is representative of the formation of the modified layer on the PR surface, whereas the progression of the data from lower right to upper left is representative of bulk layer etching, as depicted by the inset compass in Fig. 4.5a. Independent of the set processing conditions, as the number of ALE cycles progresses, the establishment of the modified layer results in a progressive decrease in the amount of bulk layer that is etched during each cycle. Under some conditions, an etch stop is almost obtained. The impact of the ion energy on the surface modification and etching behavior is shown in Fig. 4.6a.

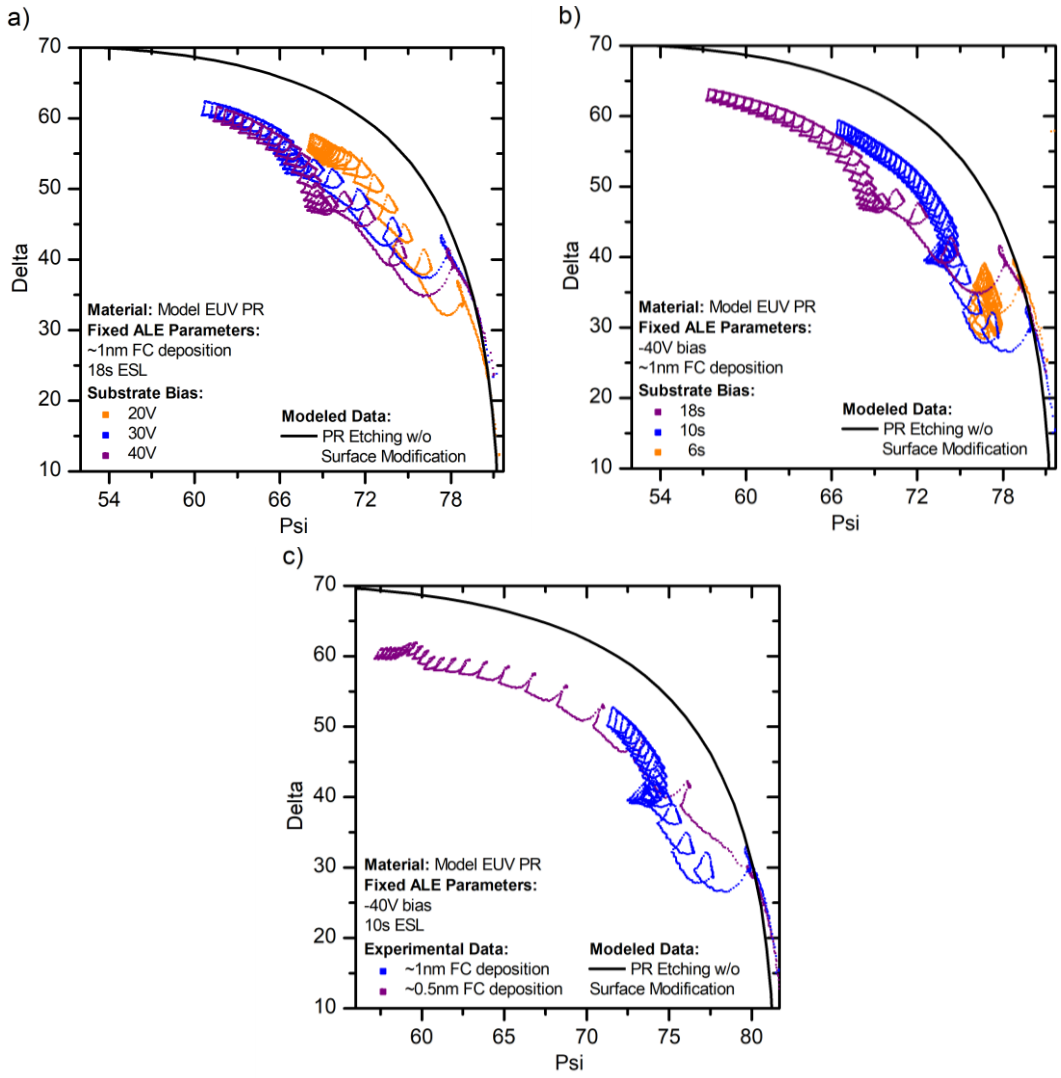

Figure 4.6. Dependence of the PR etching and modification behavior on (a) substrate bias voltage, (b) etch step length, and (c) FC deposition thickness. Increasing the substrate bias voltage leads to a greater ion energy that induces a more prominent modified layer. The prominence of the modified layer becomes such that a further increase in the substrate bias from 30 V to 40 V does not result in additional PR etching. Decreasing the duration of the etch step limits the amount of PR loss before a steady-state etching regime is established. A small difference in the amount of FC deposited during each ALE cycle has critical implications for establishing the surface modified layer that controls the PR etching behavior.

Initially, the increase in the substrate bias from 20 V to 30 V produces a more prominent modified layer. However, the amount of material etched over the process duration is increased as well, from 16 nm to 26 nm. A further increase in the substrate

bias to 40 V produces an even more prominent modified layer, but in this case the enhanced formation compared to the 30 V case results in the next amount of thickness etched to be comparable to that of the 30 V case (about 23 nm). Therefore, a substrate bias of 40 V was chosen and held fixed for evaluation of the remaining ALE process parameters, as this voltage provided the best potential for maximizing SiO_2 etching. Next, Fig. 4.6b examines the impact of the etch step length at a fixed 40 V substrate bias. Compared to the substrate bias parameter, the ESL mainly controls the extent of the bulk layer that is etched. Correspondingly, the longest ESL of 18 s yields the greatest amount of PR loss and a decrease in the ESL to 10 s decreases the net amount of PR loss to approximately 18 nm. When the ESL is further decreased to 6 s, the duration of energetic ion bombardment is insufficient for full removal of the deposited FC from each subsequent ALE cycle, and eventually results in irreversible deposition on the PR surface. The last panel, Fig 4.6c, shows the impact of the FC deposition thickness at a 40 V substrate bias and 10 s ESL. The standard condition with a 1 nm FC deposition thickness yields the characteristic ALE cycles, and produces the surface modification that limits the etching of the PR. Critically, a decrease in the FC deposition thickness to 0.5 nm results in a less prominent modified layer, a much longer duration to establish a stabilized PR etch regime, and a significantly greater net amount of bulk layer etching, in excess of 30 nm.

4.3.2 Impact of ALE Parameters on SiO_2/PR Etching Selectivity

4.3.2.1 Ion Energy

Figure 4.7 compares the total thickness change of the model EUV PR and SiO_2 over the duration of the ALE process using the two different FC precursor gases

at substrate biases of 20 V, 30 V, and 40 V. At the lowest tested substrate bias of 20 V, the net amount of material etched is comparable between the PR and the SiO_2 using a C_4F_8 precursor, but the CHF_3 precursor results in deposition on both the PR and SiO_2. At 30 V, the etching behavior of SiO_2 and the PR is comparable between the two FC precursors, with the PR being able to attain a steady-state etching regime; thus, the overall amount of SiO_2 etched is about twice as that of the PR. Increasing the substrate bias to 40 V results in the amount of SiO_2 etched to be about two and a half times greater relative to the PR. The net PR loss at the end of the process duration is comparable between the two precursors. However, the initial PR loss during the initial ALE cycles before a steady-state etching regime is established is over one and a half times greater with CHF_3 compared to C_4F_8. Based on these results, a 40 V substrate bias was held fixed for evaluation of the remaining ALE process parameters, as it yielded the highest etching selectivity of SiO_2 to PR.

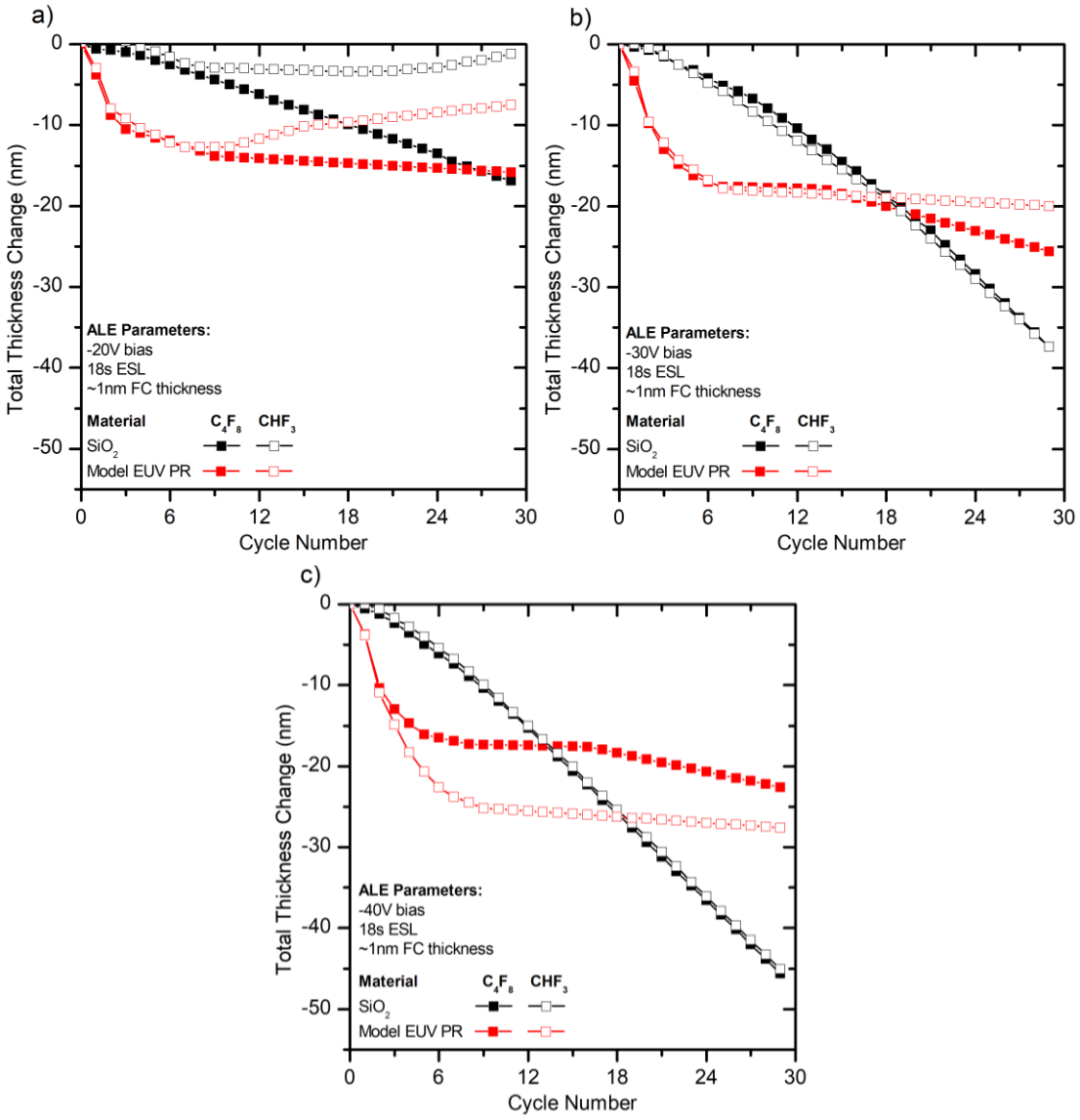

Figure 4.7. Comparison of the thickness change of SiO_2 and the model EUV PR with the progression of the number of ALE cycles for (a) 20 V, (b) 30 V, and (c) 40 V substrate biases. As the substrate bias and corresponding ion energy increases, the etch per cycle of SiO_2 increases much more significantly than that of the PR. The PR exhibits a significantly reduced etch per cycle once the PR surface modification is established after 5-6 cycles.

4.3.2.2 Etch Step Length

Figure 4.8 compares the total thickness change of the model EUV PR and SiO_2 over the duration of the ALE process for ESLs of 18 s, 10 s, and 6 s. For an accurate comparison of the overall etching amounts, the total process duration was

kept the same for each examined ESL (i.e., an experiment with a shorter ESL requires a greater number of cycles to have the same processing duration as one with a longer ESL). Decreasing the ESL from the initial 18 s to 10 s under both FC precursors reduces the amount of PR loss during the initial five to six cycles, and strongly limits any further PR loss once the steady-state behavior is established after this point. Actually, when using CHF_3, the PR exhibits an etch stop after the initial cycles, with subsequent cycles producing a minimal deposition on the PR surface. For both FC precursors, the SiO_2 attains a steady-state etching behavior after approximately ten cycles and remains stable throughout the duration of the process. The consistent SiO_2 etching, coupled with the PR etch stop, results in the 10 s ESL yielding the greatest net SiO_2/PR etching selectivity (in excess of 3:1). It is possible that a greater net etching selectivity can be achieved by extending the process duration. A further decrease in the ESL to 6 s results in irreversible deposition on the PR surface after the initial PR loss occurs in the first five to six cycles. The decreased ESL duration also results in a decreased amount of SiO_2 etching compared to the other ESL durations. Based on these results, a 10 s ESL was chosen for evaluation of the remaining ALE process parameter as it produced the best SiO_2/PR etching selectivity.

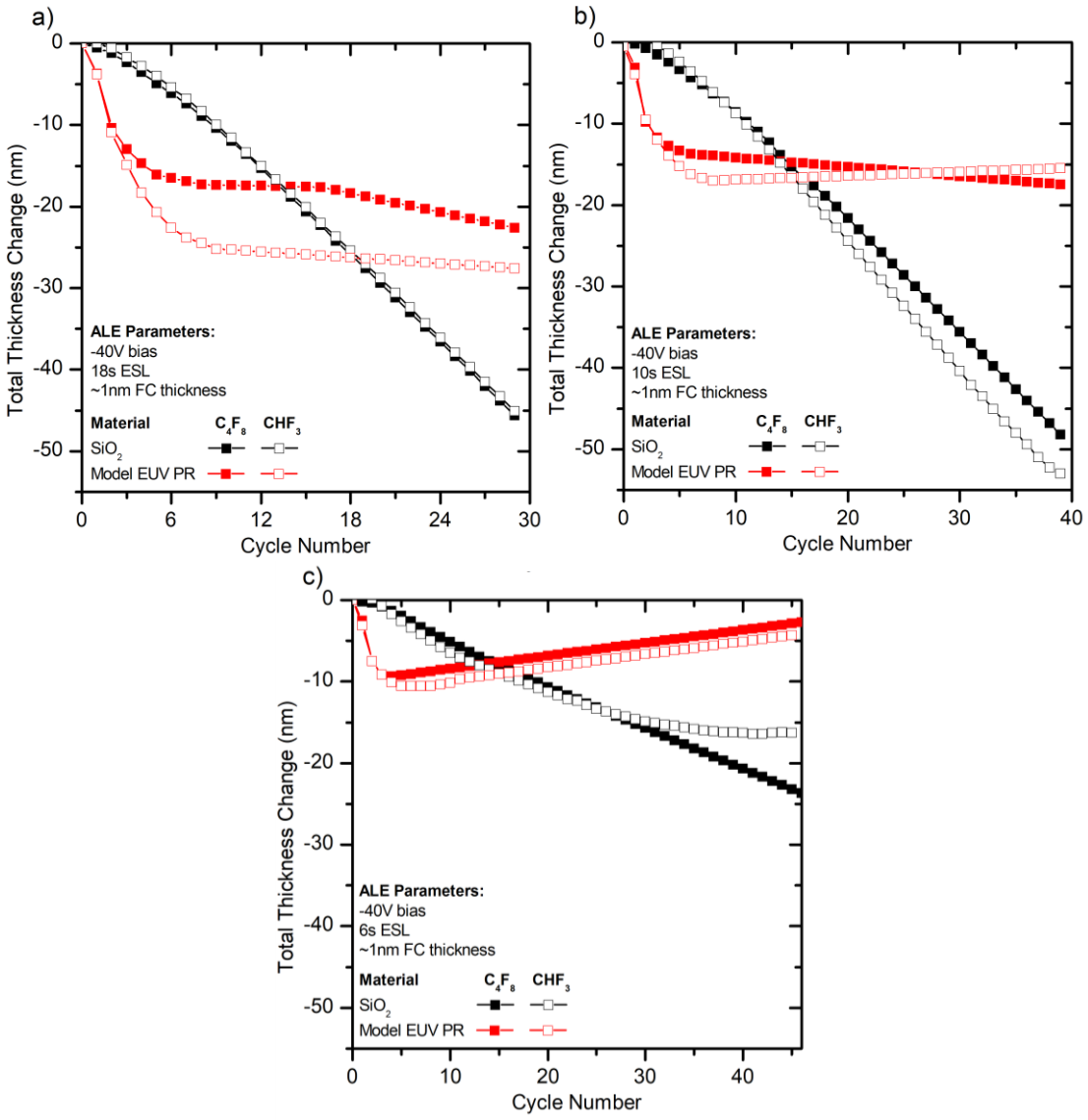

Figure 4.8. Comparison of the thickness change of SiO_2 and the model EUV PR with the progression of the number of ALE cycles for (a) 18 s, (b) 10 s, and (c) 6 s etch step lengths. A reduction of the etch step length to 10 s minimizes the initial PR loss before the surface modification attains a steady-state etch per cycle. At the same time, a good SiO_2 etch per cycle is maintained, thus maximizing the SiO_2/PR etching selectivity. A further decrease of the etch step length to 6 s results in a cessation of etching and a progressive deposition of FC on the PR surface.

4.3.2.3 FC Deposition Thickness

Figure 4.9 compares the total thickness change of the model EUV PR and SiO_2 over the duration of the ALE process for a FC deposition thickness of

approximately 0.5 nm and 1 nm. The indicated FC deposition thickness was calibrated based on the thickness of the discrete FC layer that formed on SiO_2. The processing parameters to achieve the desired thickness were then applied to the experiments with the PR. The thickness of the discrete FC layer on the PR could not be directly quantified due to the complex interaction between the FC and the surface modified layer. A FC deposition thickness of 1 nm in each ALE cycle produces the controlled PR etching behavior and continuous SiO_2 etching that enables the high SiO_2/PR etching selectivity. Reducing the FC deposition thickness to 0.5 nm in each ALE cycle results in much greater amount of PR loss before a steady-state etching regime is established as well as a decrease in the amount of SiO_2 that can be etched.

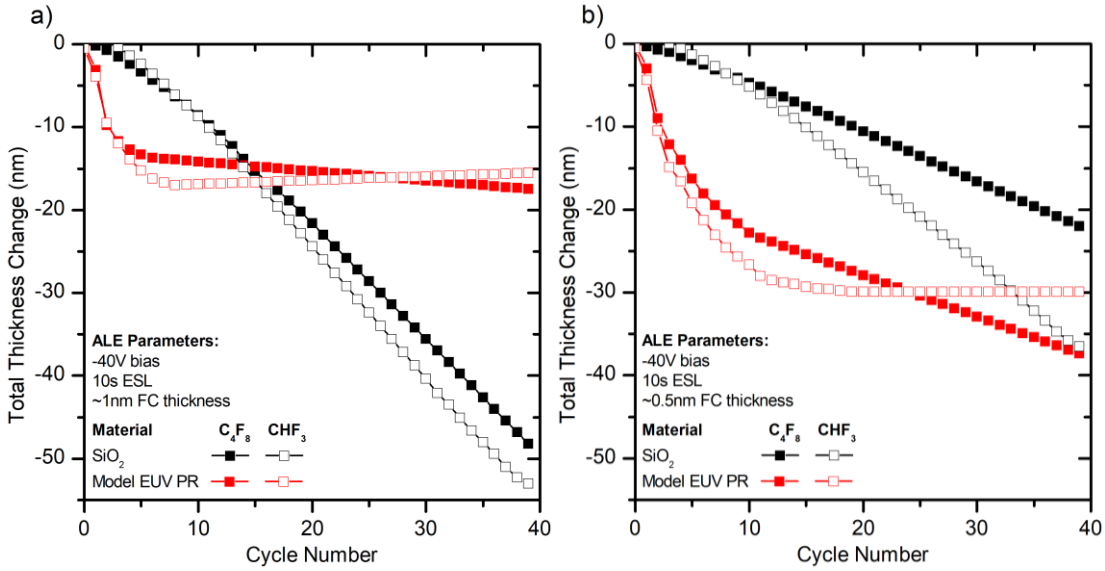

Figure 4.9. Comparison of the thickness change of SiO_2 and the model EUV PR with the progression of the number of ALE cycles for a (a) 1 nm FC deposition thickness per cycle and (b) 0.5 nm FC deposition thickness per cycle. A reduction of the FC deposition thickness to 0.5 nm both reduces the etch per cycle of the SiO_2, because fluorine is required to enhance the etching of SiO_2, and increases the net thickness loss of the PR, because a sufficient carbon content from the deposited FC film is potentially required upon energetic ion bombardment in order to form the modified layer that limits the PR etch rate.

4.3.3 Surface Morphology

The extent of the impact of an ALE process and the chosen FC precursor chemical composition on the model EUV PR surface morphology is shown in Fig. 4.10. The AFM scans were taken for an equivalent amount of material etched for the processed samples. The pristine model EUV PR has a low RMS roughness of 0.2 nm which increases to 0.4 nm as a result of a baseline argon plasma exposure with a 40 V substrate bias. Under an ALE process, the RMS roughness increases to 1.0 nm and 1.5 nm with a C_4F_8 and CHF_3 precursor, respectively.

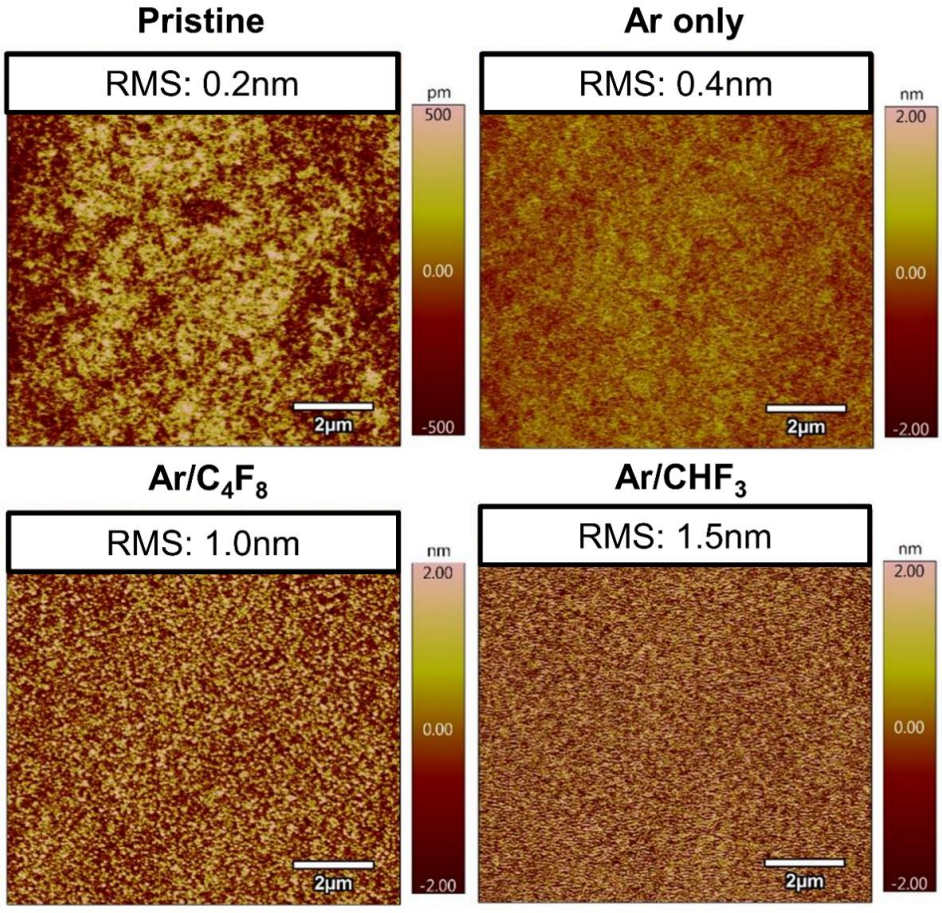

Figure 4.10. AFM measurements of the surface roughness of the model EUV PR. Controlling the PR etch rate via an ALE process introduces additional surface roughness relative to a baseline Ar-only process. However, the overall RMS magnitude remains small.

4.3.4 Surface Chemical Composition/Molecular Structure

Figure 4.11 depicts the evolution of specific bonds of characteristic functional groups within the model EUV PR composition at various timepoints in the ALE process as measured using ATR-FTIR. The identities of the indicated bonds and associated functional groups observed in the spectra are listed in Table 4.2. [30,37,110] The FTIR spectra of the processed model EUV PR samples were taken at the end of the FC deposition steps of the 1st, 6th, and 27th ALE cycles and compared with a pristine unprocessed sample. As the spectral intensity obtained via the ATR technique is sensitive to the quality of the contact between the sample surface and the Ge crystal, the peak intensities were normalized to a characteristic SiO_2 spectral peak (Peak H), as this peak originates from the substrate, which is not impacted by the plasma process, and is identical for all the samples tested.

Table 4.2. Identification of the key bonds within specific functional groups in the PR composition using ATR-FTIR that are impacted by the ALE process.

Peak Label	**A**	**B**	**C**	**D**	**E**	**F**
Absorption Peak(cm^{-1})	3400	2920-2862	1713-1692	1614-1597	1514	1448
Vibrational Mode	O-H stretch	C-H stretch	C=O stretch	C=C stretch	C=C stretch	C-H scissor
Functional Group/ Bond	Phenol	Methyl/ Methylene/ Aromatic	Ester/ Ketone	Aromatic	Aromatic	Methyl/ Methylene
Peak Label	**G**	**H**	**I**	**J**	**K**	**L**
Absorption Peak(cm^{-1})	1377-1360	1217	1172-1146	1103-1094	887	831
Vibrational Mode	C-H rock	Si-O-Si stretch/ C-O stretch	C-F stretch	C-O stretch	C-H bend	C-H bend
Functional Group/Bond	Methyl	Si-O/ Ester	Fluoroalkane	Ester	Substituted Alkene	Substituted Aromatic

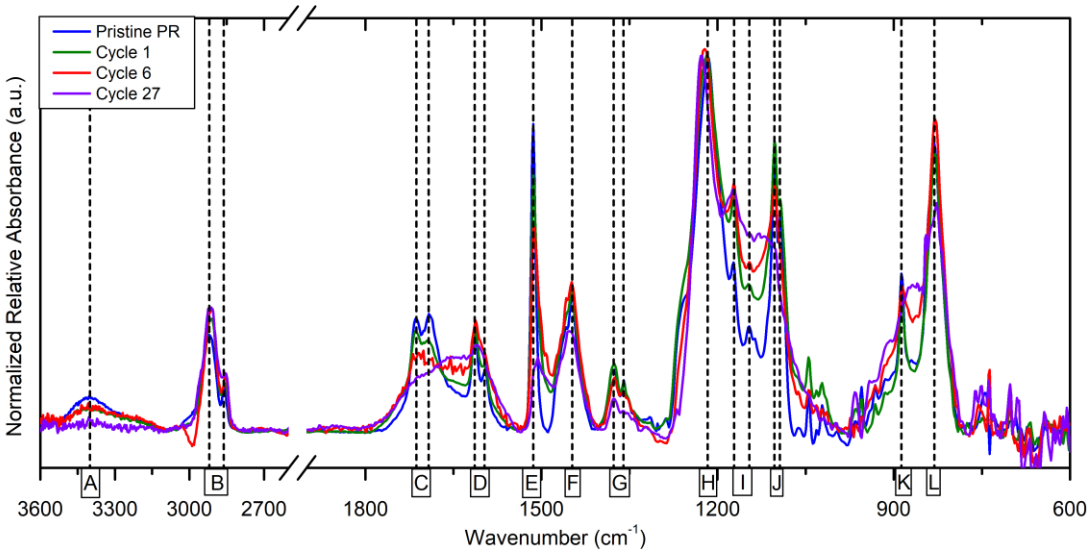

Figure 4.11. ATR-FTIR spectra at various timepoints in the ALE process using a C_4F_8 precursor. The details of the labeled peaks are given in Table 4.2.

The functional groups in the model EUV PR molecular structure that are most significantly impacted by the ALE process are examined in Fig. 4.12. The decrease in the signal intensity of these groups with an increasing number of cycles highlights the volatility of the oxygen- and hydrogen-containing functional groups. Specifically, there is a depletion in the O-H stretch vibrational mode corresponding to the phenol group (Fig. 4.12a), a depletion of the C=O stretch vibrational mode corresponding to an ester or ketone group (Fig. 4.12b), and a depletion of the C-H scissor (Fig. 4.12c) and C-H rock (Fig. 4.12d) vibrational modes corresponding to methyl/methylene and methyl groups, respectively. The C=C stretch vibrational mode corresponding to the aromatic functional group (Fig. 4.12c) also exhibits a progressive depletion as the number of ALE cycles increases. Notably, however, there is an increase in the amount of C-H stretch vibrational modes corresponding to methyl, methylene, and aromatic groups (Fig. 4.12a) with an increasing number of ALE cycles. Figure 4.13a illustrates the main region in which the impacts from the FC species are potentially

observed via an increase in the peaks at 1172 cm^{-1} and 1146 cm^{-1}, which can be interpreted as originating from the C-F stretch vibrational modes that are characteristic of fluoroalkane groups. This region also shows a depletion of the C-O stretch vibrational mode that corresponds to the ester functional group. The included FC reference line represents the characteristic spectrum of a thick deposited FC layer on silicon produced with a C_4F_8 precursor. The expanded wavenumber range compared against the reference spectrum in Fig. 4.13b illustrates the characteristic peak of native FC species as being a broad peak in the region of 1000-1400 cm^{-1}. As the number of ALE cycles increases, the progressive FC enrichment of the surface results in the pristine PR FTIR spectrum to become more similar in conformation to that of the reference FC spectrum. Within the region shown in Fig. 13b, there is expected to be an additional C-O stretch vibrational mode corresponding to the ester group around 1210 cm^{-1}, however this peak is obscured by the characteristic SiO_2 spectral peak at 1217 cm^{-1}. Figures 4.11-4.13 show the surface chemistry evolution for an ALE process using a C_4F_8 precursor, but the surface chemistry evolution under an ALE process with a CHF_3 precursor is nearly identical for the majority of the functional groups. The one notable difference in the surface chemistry evolution between the two precursors is shown in Fig. 4.14b, where the CHF_3 precursor results in the emergence of a C-H bend vibrational mode that is characteristic of substitutions occurring on alkene groups, whereas the C_4F_8 precursor (Fig. 4.14a) does not exhibit this modification behavior on the PR. In this wavenumber region, however, both FC precursors exhibit a similar depleting impact on the C-H bend vibrational mode that corresponds to substituted aromatic groups.

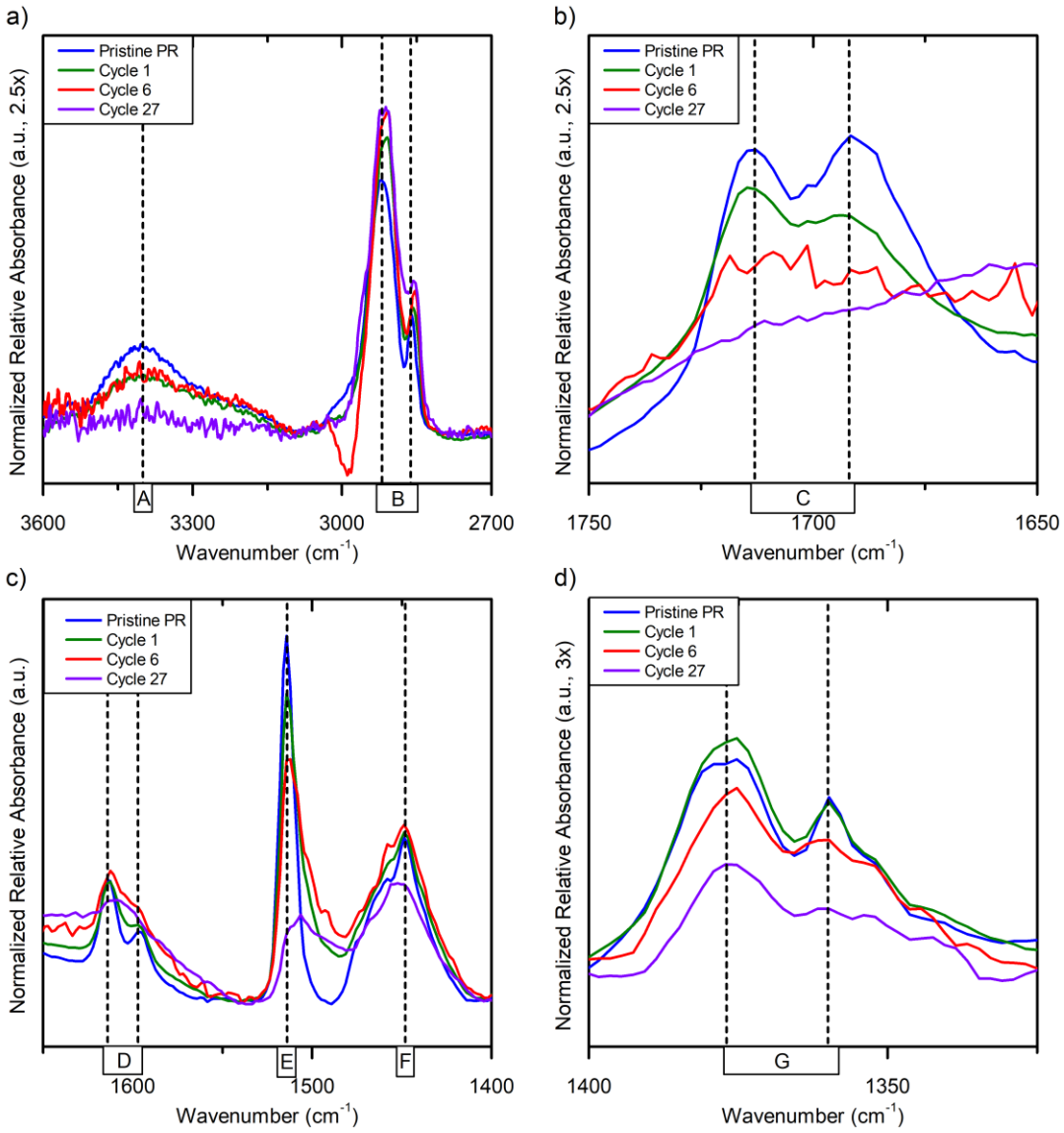

Figure 4.12. Evolution of the FTIR peak regions during an ALE process with a C_4F_8 precursor that indicate the (a) depletion and emergence of the phenol O-H stretch and methyl/methylene/aromatic C-H stretch modes, respectively. (b) Depletion of the ester/ketone C=O stretch mode. (c) Depletion of the aromatic C=C stretch and methyl/methylene C-H scissor mode. (d) Depletion of the methyl C-H rock mode.

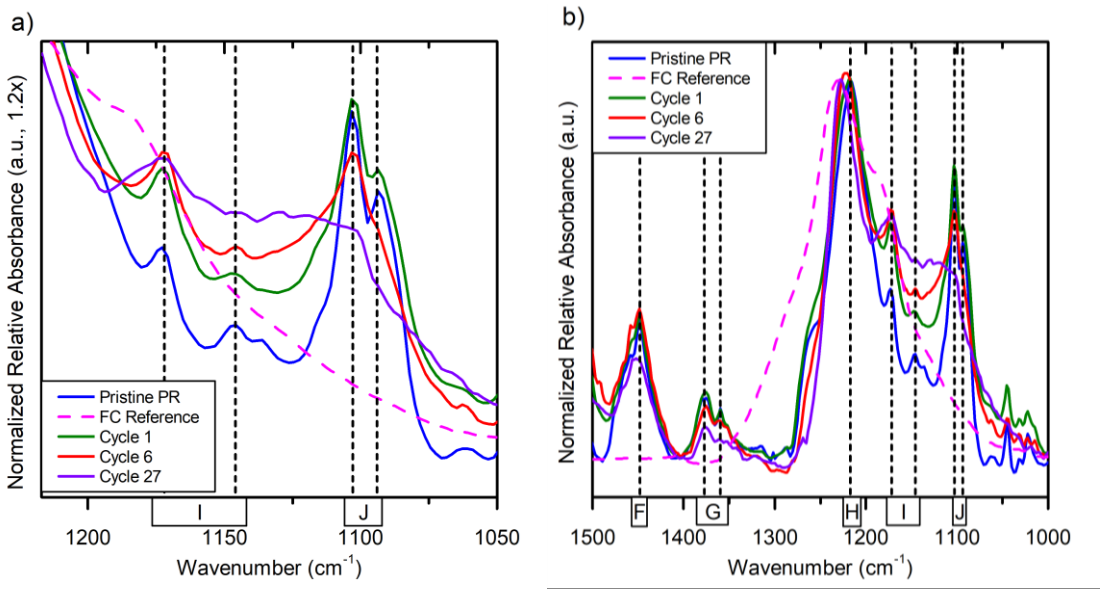

Figure 4.13. (a) FTIR peak region showing the emergence of the fluoroalkane C-F stretch mode from the deposition of FC species and the depletion of the ester C-O stretch mode under an ALE process with a C_4F_8 precursor compared against a FC reference spectrum produced by a thick FC film deposited on a Si substrate that was also created with a C_4F_8 precursor. (b) Expanded wavenumber region comparing the extent of the impact from the FC species on the model EUV PR against the FC reference spectrum.

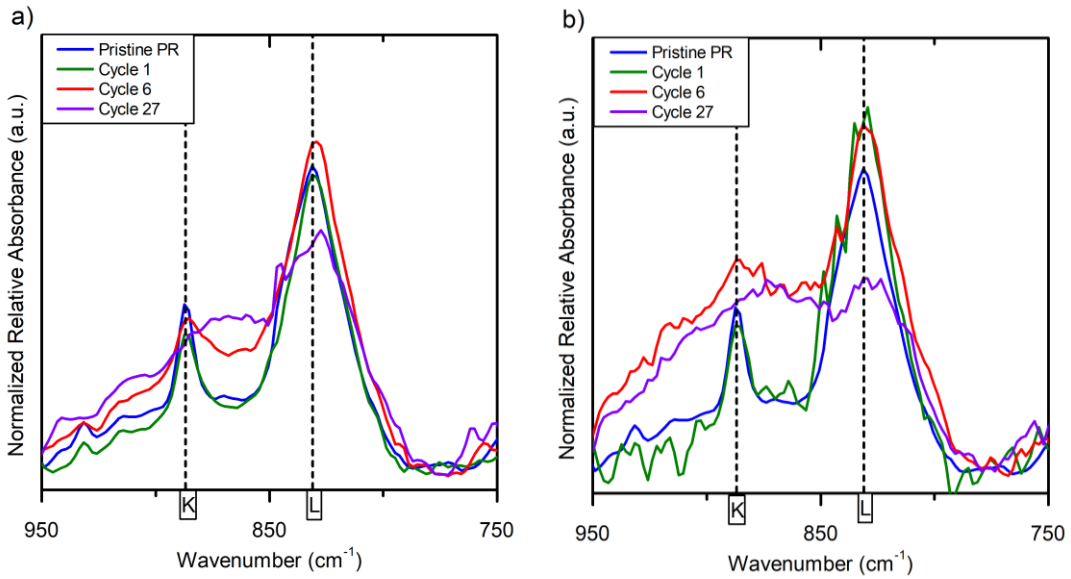

Figure 4.14. Comparison of the FTIR peak regions showing the differences in the magnitude and evolution of the C-H bend modes corresponding to substituted alkene and substituted aromatic structures under an (a) C_4F_8 precursor and (b) CHF_3 precursor. The accumulation of the FC film produced by the CHF_3 precursor results in a greater prominence of vibrational modes corresponding to substituted alkene structures relative to those observed in the FC film produced by the C_4F_8 precursor.

4.4 Discussion

4.4.1 Mechanisms Behind ALE Process-Induced PR Surface Modification

The comparison of the PR etching behavior under an ALE process relative to a typical CW process emphasizes the unique surface modification that takes place on the model EUV PR material, which allows for controlled etching to take place in a reactive plasma composition. In prior work, controlled etching via the formation of an etch-mediating surface layer was only observed under an inert plasma condition. In this situation, energetic ion bombardment depletes oxygen, hydrogen, and volatile-product-forming species from the surface region, which produces a surface dense amorphous carbon (DAC) layer with a high density from the majority C-C bonding, as supported by the XPS scan in Fig. 4.4b, and low etch yield. [3,7,11,23,31] The DAC layer dissipates energy, which mediates the etching of the underlying bulk layer.[63] However, for pattern transfer applications, a reactive plasma chemistry is required in order to realize sufficient etching of substrate or hard mask materials, such as SiO_2. Under a CW reactive FC plasma condition, the chemical etching of the DAC layer from fluorine species prevents a significant DAC layer from forming, and thus there is no enhancement of the etch resistance of the PR material, as is explained in Fig. 4.3.[16,111] Therefore, the ability of an ALE process to incorporate a reactive FC plasma chemistry while concurrently creating a greater developed etch resistance than that created by an inert CW Ar-only process represents a significant potential

improvement over reactive CW processes for enabling applications such as pattern transfer processes with reduced PR thickness loss.

The key mechanism that enables a controlled PR etch behavior in the presence of the reactive FC gas chemistry in an ALE process is the interaction between energetic argon ions and the deposited FC passivating layer. This interaction forms a modified layer on the PR surface that behaves as an additional passivating layer to limit the etching of the underlying bulk layer. Like the etch resistant, C-C-bond-rich DAC layer that is formed under an inert CW plasma, an ALE process produces a similar passivating layer, but one that also has a composition consisting of CF-bonded type species (Fig 4.4b). An etch stop of the PR can occur if the developed modified layer becomes so thick and dense that it cannot be adequately etched away to enable etching of the underlying bulk layer. However, under energetic enough conditions, the etch stop is only temporary, and the etching of the bulk layer is resumed once the modified layer becomes sufficiently enriched with FC species. This relationship between the plasma condition, developed surface modification, and corresponding etching behavior is outlined in Figs. 4.3-4.5. Specifically, the near-etch-stop condition that occurs after approximately six cycles, as shown in Fig. 4.4a, corresponds to a surface composition that is dominated by C-C bonding with a lesser content of CF-type bonded species (Fig. 4.4c). However, Fig. 4c also shows that upon resumption of etching of the bulk, which occurs past the sixth cycle, the surface composition contains a greater content of CF-type bonded species relative to C-C bonded species.

One key aspect of the ALE process setup that allows the PR behavior to develop relative to a CW process is the ability to adjust the ESL and FC deposition intervals such that the majority of the processing time consists of an inert argon plasma condition. For example, in the condition that produced the highest SiO_2/PR etching selectivity (Fig. 4.8b), argon ion bombardment constitutes over 90% of the process duration. In this manner, an etch-mediating surface modified layer can still form and be sustained even in the periodic presence of reactive FC species. Another important consideration, though, is that formation of a significant DAC layer for enhancing the PR etch resistance under a CW inert plasma condition usually requires an ion energy in excess of 65 eV, which is beyond the upper limit of the typical ALE energy window.[111,112] This energy is required in order to scission sufficient bonds to produce the denser carbon-rich surface layer. Based on these findings, our optimal ion energy setting of a 40 V substrate bias (~55 eV ion energy) would not be expected to yield a significant modified layer for etch mediation. However, several mechanisms are present in the ALE process that supplement the intrinsic carbon content of the PR material, and thus are able to produce an etch-mediating modified layer in the presence of a lower ion energy. First, the deposition of the FC layer on the PR layer results in some mixing with the underlying bulk layer, resulting in the characteristic directionality in the ellipsometric data (Fig. 4.5a) and increasing the carbon content in the near-surface region, as shown in the XPS characterization in Fig. 4.5b.[4] Next, ion bombardment of the deposited FC layer during the etching step leaves some residual carbon on the underlying PR surface in the form of a FC-rich modified layer that accumulates over the process duration (Fig. 4.4c) and produces the periodic

ellipsometric trajectory that describes the progressive formation of the modified layer.[24,28,65] The combination of both the intrinsic carbon content of the PR material and the carbon content supplied from the ion bombardment of the FC film produces a modified layer that mediates the etching behavior of the PR under an ALE processing setup.

4.4.2 Establishing SiO_2/PR Etching Selectivity

Attaining a high SiO_2/model EUV PR etching selectivity requires the formation of the modified layer on the PR surface. As Figs. 4.7-4.9 show, the development of a modified layer requires five to six ALE cycles to progress before the modified layer is sufficiently built up to limit the etching of the PR. During these initial cycles, the amount of PR etched per cycle is high due to the lack of a built-up modified layer and enhanced etching from the reactive FC species. For the same conditions, the etching behavior of SiO_2 is more consistent with significantly less variability between the initial cycles and later cycles. The slightly lower etch per cycle of SiO_2 during the initial cycles is likely due to a progressive stabilization of the FC concentration on the reactor walls.[113] For most conditions, the etching behavior of both the SiO_2 and the model EUV PR does not vary significantly between the two FC precursor chemistries. Thus, the choice between the two FC precursors is not significant for the SiO_2/PR etching selectivity. Overall, once the etch-mediated regime is established for the PR, the relative etch per cycle of SiO_2 relative to PR can exceed a ratio of 10:1, with the net SiO_2/PR etching selectivity then only being dependent on the duration of the ALE process. Table 4.3 summarizes the key trends

in the relative model EUV PR and SiO_2 etching behaviors from the evaluation of the ALE processing parameters.

Table 4.3. Summary of the impacts of the ALE parameter trends on the relative etching trends of the model EUV PR and SiO_2. Net selectivity is defined as the total amount of SiO_2 etched relative to the total amount of PR etched over the process duration.

ALE Parameter Trend	Model EUV PR etch per cycle	SiO_2 etch per cycle	Net SiO_2/PR etching selectivity
Increasing ion energy	→	↑	↑
Decreasing etch step length	↓	→	↑
Reduction in FC deposition thickness	↑	↓	↓

One area that is important for pattern transfer viability is maintaining the cleanliness of both the PR and SiO_2 surfaces, as the integrity of the interface between the PR and underlying substrate is essential for preserving the fidelity of pattern-transferred features. Under the explored ALE parameter space, the thickness of the residual FC/modified layer at the end of the etching step is expected to be less than 1 nm, thus preserving the surface condition for pattern transfer.[28] Avoiding undesired deposition on the sample surfaces mainly requires the use of a sufficient ESL to remove the deposited FC layer. An ESL of insufficient duration, such as 6 s (Fig. 4.8c), exhibits not only consistent FC accumulation on the PR surface once the modified layer is established, but also highlights a key difference between the two FC precursors that is significant for etch selectivity in a pattern transfer process. Due to the differences in the deposition yields, a higher flow of CHF_3 is needed relative to that of C_4F_8 (6 sccm vs 2.2 sccm) in order to attain the same FC deposition thickness on the SiO_2 and PR. Additionally, a shorter ESL leads to a greater number of cycles

and FC deposition steps within a given processing time, resulting in an increased FC concentration on the reactor walls. With the higher flow rate of CHF_3 compared to C_4F_8, the buildup of the FC concentration in the reactor eventually results in an etch stop of the SiO_2 with CHF_3, but not with C_4F_8. This finding illustrates the importance of the FC precursor gas chemistry with regards to the deposition yield as the use of a higher flow rate to offset a lower deposition yield can eventually lead to an undesirable etch stop of both PR and substrate materials.[114]

Crucially, the FC deposition thickness is the most important processing parameter for enabling highly selective etching of PR materials. Based on the findings shown in Figs. 4.6c and 4.9, a reduction in the per-cycle deposited FC thickness from just 1 nm to 0.5 nm results in the absence of a discrete FC layer on the PR surface and initially a less prominent modified layer. The consequence of these occurrences is that a sufficiently etch-mediating modified layer requires a much longer process duration to form. Therefore, the initial PR loss is greater, and the net amount of PR loss is significantly higher than the case with a 1 nm per-cycle FC deposition thickness. At the same time, the reduced FC deposition thickness also reduces the net amount of SiO_2 that is etched during the process. In this condition, the residual FC concentration in the chamber may play a more significant role in defining the etching behavior as the process using CHF_3, with its higher flow rate, etches 75% more SiO_2 over the process duration relative to the process using C_4F_8. These results suggest that the thickness of the deposited FC layer is related to the fluorine content that is necessary to etch the SiO_2, as well as the carbon content that is needed to form a sufficiently etch-mediating modified layer on the PR surface.

4.4.3 ALE Process Impact on PR Roughening Behavior and Surface Composition/Molecular Structure

4.4.3.1 PR Roughening Behavior

The PR roughening behavior is a crucial aspect in defining parameters of patterned features related to the feature fidelity, such as the LER. The presence of an etch-mediating modified layer has potential additional implications on the roughening behavior, as a reduction in the etch rate requires the PR surface to dissipate more of the energy of the incident ions before it is etched away. This phenomenon can induce stresses within the surface region that result in enhanced surface roughening, especially if the PR composition is sensitive to vacuum ultraviolet (VUV) irradiation.[8,19,38] Thus, although there is some increase in the RMS roughness of the model EUV PR compared to a baseline process as a result of the ALE process, the magnitude of roughening is still significantly lower than that of a 193 nm PR processed under the same conditions (4-6 nm RMS). Elements of the model EUV PR composition, such as the presence of an aromatic group that is largely insensitive to VUV irradiation and the scarcity of oxygen, facilitates the high intrinsic etch resistance and low magnitude of surface roughness.[8,10,11,19,30,38] Additionally, the systematic etching of the PR material via sequential FC deposition and argon ion bombardment steps in an ALE process has been shown to produce a smoothening effect that mediates the roughness development.[115] The slight differences in the surface roughness between the CHF_3 and C_4F_8 precursors may be caused by a variation in the chemical composition at the PR surface. Based on the measured

surface roughness of the model EUV PR, existing relationships predict the developed LER to be less than 7 nm RMS.[93]

4.4.3.2 Surface Composition/Molecular Structure

The ATR-FTIR analysis allows for correlation of the impacts of the ALE process, precursor chemistry, and resultant etching behavior, to the PR composition. Although the ATR-FTIR analysis is not as localized to the surface region as the XPS analysis, with a probing depth that samples the entire 126 nm combined thickness of the model EUV PR and SiO_2 substrate compared to the ~2 nm probing depth of the 20° XPS scans, the ATR-FTIR analysis provides complementary information to the bonding information provided by XPS on the specific functional groups that are impacted by the plasma process. The methyl, ester, and phenol functional groups exhibit a significant depletion from the plasma process as the C-O and C-H bonds residing in the MAdMA block and the O-H bond in the PHOST block of the PR structure are the most susceptible to scissioning from ion bombardment. [3,7,11,23] The vibrational modes at 1713 cm^{-1} and 1692 cm^{-1} in Fig. 4.12b, which have been interpreted as being representative of the C=O stretch of the ester functional group, are located lower in wavenumber than what is typically observed. Furthermore, the polymer backbone only has one ester group present, thus the expectation would also be for only one characteristic C=O stretch peak to be present. However, there are several possible mechanisms that can account for multiple peaks in this wavenumber region. If there are nearby hydrogen species present in the PR structure, then the hydrogen bonding between the oxygen in the ester group and the nearby hydrogen atoms can lead to a shift in the infrared peaks to a lower wavenumber.[116] Another

potential mechanism arises from the scissioning of the C-O bond in the ester group from the blanket ultraviolet exposure that was used to prepare the PR films and from the plasma exposure during the ALE process. If the broken bond reforms with molecular structures that are heavier in mass, then the resulting impact is likewise a shift in the infrared peaks to a lower wavenumber.[117] Therefore, a combination of both hydrogen bonding and bond reconfiguration may play a role in the presence of the two distinct infrared peaks corresponding to the C=O stretch vibrational modes. Similar mechanisms may account for the two distinct infrared peaks at 1103 cm^{-1} and 1094 cm^{-1} (Fig. 4.13a), which can be attributed to the C-O stretch vibrational modes, corresponding to an ester group. Continuous plasma exposure during the ALE process results in the progressive depletion of these peaks that are attributed to the ester functional group. Similarly, the peaks representative of a C-H scissor vibrational mode at 1448 cm^{-1} and C-H rock vibrational mode at 1377 cm^{-1} (Fig. 4.12c,d), both corresponding to a methyl group, exhibit a comparable decrease from the plasma exposure. One of the distinctive components of the PHOST structure in the infrared spectrum is the presence of a phenol group. As an oxygen-containing functional group, the infrared peaks associated with this group decrease as a result of the plasma exposure. This effect can be seen in the decrease of the C-H bend vibrational mode at 831 cm^{-1}, corresponding to a substituted aromatic group (Fig. 4.14a,b), and the decrease of the O-H bend vibrational mode, corresponding to a phenol group (Fig. 4.12a), at 3400 cm^{-1}.[118] Another distinctive peak of PHOST arises from the C=C stretch vibrational modes that correspond to the aromatic ring structure at 1514 cm^{-1} with less prominent secondary peaks around 1600 cm^{-1} (Fig. 4.12c).[118] All these peaks

also exhibit a depletion as the ALE process progresses, however, the high intrinsic etch resistance of the aromatic functional group, due to the stability of the aromatic ring to ion bombardment and VUV irradiation, suggests that the depletion of this functional group arises from the chemical reaction with the deposited FC species.[11,19,30] Concurrently, the increase in the peaks between 2862 cm^{-1} and 2920 cm^{-1}, corresponding to the C-H stretch mode of methyl, methylene, and aromatic groups, may arise from the breakdown of the aromatic ring structures in the PR into linear chains. Relative to the decrease in signal intensity exhibited by the vibrational modes corresponding to the other significant functional groups, the loss in signal intensity corresponding to the vibrational mode of the aromatic group is the greatest. Combined with the supporting XPS characterization, which shows a decrease in the amount of C-C bonding and increase in C-F_x bonding (Fig. 4.4b,c, Fig. 4.5b,c), the aromatic group is one of the key structures in the PR molecular structure that becomes depleted from the interaction with the FC species as the ALE process proceeds. In fact, the degradation of the aromatic group under the cyclic FC exposure in the ALE process may explain why the PR etch per cycle increases under some conditions after the minimum etch per cycle is obtained upon the maximum formation of the modified layer, such as in Fig. 4.7b,c.

Regarding the impact from the FC species, even though the peak from the FC species in the FTIR analysis is broad and overlaps the SiO_2 and ester group peaks (Fig. 4.13b), the corresponding increase of the signal intensity in the region between 1100-1200 cm^{-1}, as the number of ALE cycles progresses, relates to the increased formation of C-F bonds on the PR surface, and is consistent with the reference FTIR

spectra and supporting XPS characterization (Fig. 4.4b,c, Fig. 4.5b,c). This behavior is evidence for a progressive fluorine enrichment of the surface that can be associated with the formation of the modified surface layer. The smaller C-F subpeaks in Fig. 4.13a potentially originate from a small intrinsic fluorine content in the model EUV PR, which was observed with XPS analysis, and increase as the number of ALE cycles progresses, from the formation of the modified surface layer that develops from the supplied fluorine interacting with the native carbon-rich structures in the PR composition.

Although the surface chemistry impact from the two FC precursors is similar for the majority of the functional groups, the process with CHF_3 progressively develops a broad shoulder around 900 cm^{-1}, which is characteristic with the formation of substituted alkene groups on the surface. Previous work comparing the properties of deposited films produced by C_4F_8 and CHF_3 precursors found that films produced from a CHF_3 precursor possessed a higher degree of crosslinking.[119,120] The presence of an increased number of substituted alkene groups is potentially consistent with a higher degree of crosslinking and may also contribute to morphological effects such as the greater magnitude of surface roughness that was observed with the CHF_3 precursor relative to that observed with C_4F_8.

4.5 Summary and Conclusions

In this work, we evaluated the impact of an ALE process using a CHF_3 and C_4F_8 precursor on the etching behavior of a model EUV PR material. Several ALE processing parameters, namely ion energy, etch step length, and deposited fluorocarbon thickness, were systematically assessed on both the model EUV PR and

SiO_2 in order to determine the evolution of the overall SiO_2/PR etching selectivity. The evaluation of the PR using ellipsometric data supported by secondary XPS characterization reveals that under an ALE process, the argon ion bombardment of the deposited FC layer results in the buildup of a modified layer on the PR surface, which can significantly reduce the amount of PR loss. By incrementing the substrate bias voltage from 30 V to 40 V, with a corresponding increase in the ion energy, the buildup of the modified layer becomes such that net amount of PR loss over the process duration is marginally increased compared to the much larger increase in the amount of SiO_2 etched. Further evaluation of the etch step length finds a reduction from 18 s to 10 s to minimize the initial PR loss while not significantly affecting SiO_2 etching, resulting in a high net SiO_2/PR etching selectivity. Evaluation of the FC deposition thickness showed that it is the critical parameter for enabling the formation of the modified layer that controls the PR etching behavior. A sufficient FC deposition thickness is likely required to supply carbon for formation of the PR etch-mediating modified layer and to supply fluorine for satisfactory etching of SiO_2. The two FC precursor gases examined in this study, C_4F_8 and CHF_3, produce comparable etching behavior on both the PR and SiO_2

Analysis of the surface morphology via AFM shows that an ALE process marginally increases the surface roughness of the model EUV PR relative to a baseline argon process while possessing an absolute RMS magnitude that is significantly less than that of previous 193 nm PR materials. Surface chemistry analysis via XPS and ATR-FTIR finds that the combination of energetic ion bombardment of a deposited FC layer in an ALE process produces a FC-rich

modified layer that accumulates with an increasing amount of process cycles. The major impacts on the PR composition include the depletion of functional groups containing volatile oxygen- and hydrogen-containing bonds, whereas the aromatic ring structure, which contributes to the etch resistance, is less affected.

This work evaluated the fundamental mechanisms that enable a high etching selectivity between SiO_2 and a model EUV PR. The results present the potential for achieving good etching selectivity in a pattern transfer process via ALE parameter control while also maintaining a clean surface with a low magnitude of PR roughness.

Acknowledgements

The authors would like to thank D.L. Goldfarb and M. Sanchez from IBM for providing the model EUV polymer formulations and our industrial liaisons for their feedback in guiding the direction of this work. The authors gratefully acknowledge financial support of this work by the Semiconductor Research Corporation (Task No. 2017-NM-2726).

Chapter 5: Extent of Non-Vertical Ion Bombardment Due to Edge Effects on Polymer Surface Morphology Evolution and Etching Uniformity

Adam Pranda[1,3], Chen Li[2,3], Youngsik Seo[4], and Gottlieb S. Oehrlein[1,3]

[1]Department of Materials Science and Engineering, University of Maryland, College Park, Maryland 20742, USA

[2]Department of Physics, University of Maryland, College Park, Maryland 20742, USA

[3]Institute for Research in Electronics and Applied Physics, University of Maryland, College Park, Maryland 20742, USA

[4]Samsung Electronics, Hwasung City, Gyeonggi-Do, 445-701, Republic of Korea

---

A. Pranda performed all the experimental work and analysis in this chapter. C. Li extensively assisted with the realization of the experimental approach. The other authors assisted with defining the experimental objectives and discussions of the analytical approach.

Abstract

Maintaining uniform sample etching during a plasma process is a critical requirement for applications in large-scale wafer processing. Although a suitable plasma uniformity in plasma etching applications can be achieved on the macroscale by ensuring that the electrodes between which the plasma is generated are sufficiently larger than the sample processing area, the plasma uniformity on the microscale at the sample surface is strongly impacted by the electrostatic interactions between the plasma species and the sample surface. The interface between the plasma and the sample surface is defined by the plasma sheath, which accelerates ions towards the sample surface. Therefore, in areas where the plasma sheath is not parallel to the sample surface, such as near the sample edges, the incident ions arrive at shallower, off-normal angles that can result in a greater etch yield relative to other areas of the sample. This phenomenon leads to nonuniform etching, along with characteristic surface morphology evolution. In this work, we utilized a combination of spatial ellipsometry, atomic force microscopy (AFM), and power spectral density (PSD) analysis to quantify the extent and spatial dependence of the nonuniform etching near the sample edges. The spatial ellipsometry indicated that the region near the sample edge experiences approximately 10-15% more thickness loss relative to areas near the center of the sample under the tested processing conditions. Via AFM analysis, we detected the presence of ripple features that correspond to the directional ion impacts on the surface morphology. AFM scans performed in two different sample orientations confirmed that the ripple features are oriented perpendicular to the direction of incident ions and propagate along the direction of the incident ions.

Correspondingly, the magnitude of surface roughness decreases as the distance from the sample edge increases. The ripple features were quantified via the PSD analysis, which found the presence of a greater population of long-wavelength roughness closer to the sample edge. The findings of this study provide insight into the influence of the plasma sheath distortions near sample edges on the extent of nonuniform sample etching and characteristic surface morphology evolution in plasma etching applications.

5.1 Introduction

Large-scale wafer processing applications utilizing plasma etch processes necessitate precise, reproducible, and uniform etching of the processed material across the entire reactor substrate. However, plasma-surface interactions involve local electrical phenomena that impact the etching uniformity on the sample surface. The variations in the local sample uniformity arise mainly due to the presence of the plasma sheath. The plasma sheath forms as a result of the greater velocity of electrons compared to ions in a low-temperature plasma.[121] Near the sample surface, the electrons are able to escape the plasma and induce a negative charge on the sample surface relative to the bulk plasma. Consequently, the negative charging of the sample surface results in the plasma sheath to accelerate ions towards the sample surface. Over most of the sample area, this phenomenon results in uniform etching as the ions are normal to the sample surface. However, near the sample edges, the plasma sheath bends around the sides of the sample. Thus, the ions that are accelerated through the sheath impinge on the sample at a shallow off-normal incident angle.[122,123] A schematic of the influence of the sheath conformation on the incident ion angle is shown in Fig. 5.1. The shallower ion incident angle has a key impact on the etch yield in a plasma process. In empirical studies, the etch yield exhibits a maximum around an incident angle of 45°, resulting in more material etched near the sample edges as compared to the center of the sample.[124] In wafer processing, in which multiple dies are present on a single wafer, the enhanced etching at the wafer edges results in any dies located within several millimeters of the edge to be unusable.[125] However, the plasma chemistry and parameters strongly dictate the exact spatial extent of the off-

normal ion incident angle. The dimensionality of the electrostatic effect of the plasma sheath that relates the extent of angular distortions of ion impingement on the sample surface is defined by the Debye screening length. For the conditions used in this study, the Debye length is on the order of 60 μm.[126]

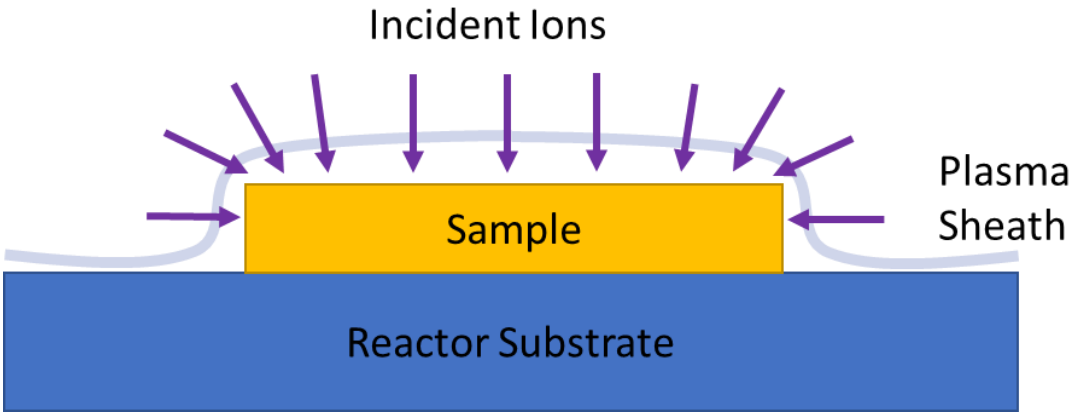

Figure 5.1. Side view schematic of the plasma sheath that develops around the sample surface, showing the regions near the sample edges where the ions collide with the sample surface at a shallower incident angle due to the conformation of the sheath.

In this study, we seek to design an experimental setup that allows for quantification of the spatial extent of the varied ion incidence angle. To accomplish this task, we utilized the surface morphology that develops on the surface of a 193 nm PR material. Following a concept employed by Merkulov et. al.[127], in which the variation in the growth direction of carbon nanofibers as a function of the distance from the sample edge demonstrated the variation in incident ion angle from the plasma sheath, we hypothesized that ions impinging the PR material at shallow angles would result in the formation of directional morphology, specifically ripple features, on the PR surface, and that these ripples could be used to track the spatial extent of the variation in the incident ion angle.[128–130] This characteristic ripple morphology produced from off-normal ions has been previously shown to be present following ion

bombardment of a wide variety of materials, including silicon, germanium, and 193 nm PR, the latter of which is used in our work.[131–133] As the ion angle of incidence approaches grazing, the corresponding etch impact can be observed via the changes in the ripple alignment, definition, and morphology.[134,135] The ripple features develop perpendicular to the direction of incident ions and propagate away from the sample edges in the direction of incident ions.

193 nm PR materials, especially, develop a significant magnitude of surface roughness from the synergistic reaction between plasma ion and VUV photon species.[8–10,19,30,63] Consequently, as the magnitude of the surface roughness increases with the amount of material etched, tracking the roughness magnitude as a function of the distance from the sample edge also provides information on the impact of off-normal ions. A precise measurement in the variation in the amount of thickness etched can be provided by use of *ex situ* spatial ellipsometry. Combining the AFM scans with the spatial ellipsometry data provides visual evidence of the range and magnitude of the impact of the spatial plasma sheath properties on the sample etching behavior, which has key implications in plasma processing applications.

5.2 Experimental Setup

The sample used in this work consisted of a 193 nm PR material that has a general molecular structure which consists of a polymethylmethacrylate (PMMA)-based backbone with several additive side groups, as described in Chapter 2.[63] The sample stack consisted of blanket 200 nm PR films deposited on 70 nm of SiO_2.

An inductively coupled plasma (ICP) reactor was used for plasma processing of the PR samples. The system consists of a spiral antenna on a quartz dielectric that

is located 13 cm above a Si electrode with a 12.5 cm diameter. The top antenna, which produces the plasma, was operated at an excitation frequency of 13.56 MHz. Control of the incident ion energy was established via substrate biasing at a radio frequency (RF) of 3.7 MHz.

For the plasma processing of the samples, the chamber was kept at a pressure of 5 mTorr. Argon gas with a 50 sccm flow rate was used to produce an argon plasma. A source power of 300 W was used to generate and maintain the plasma. Immediately after plasma ignition, an RF substrate bias of either -50 V, -75 V, or -100 V was applied to produce incident ions with energies of ~65 eV, ~90 eV, and ~115 eV, respectively, depending on the experiment. As shown in Fig. 5.1, the PR sample was directly placed on the reactor substrate in order to ensure a constant temperature, which was maintained at 10 °C using water-cooling on the substrate backside.

Tracking of the sample etching during the plasma process and evaluation of the sample thickness uniformity was performed using *in situ* and *ex situ* ellipsometry, respectively. The ellipsometer setups were configured in the polarizer-rotating compensator-sample-analyzer configuration at a wavelength of 632.8 nm. The raw data generated from the ellipsometric scans, parameterized through the optical constants psi and delta, were interpreted via an optical model that provided information on the thickness of the samples. The *in situ* setup tracked the real-time evolution of the sample thickness during the plasma process, whereas the *ex situ* setup was used post-process to perform line scans across the center of the samples to examine the spatial thickness uniformity.

Extensive atomic force microscopy (AFM) analysis was performed to image the surface morphology of the PR samples after plasma processing. AFM measurements were performed using an Asylum Research MFP3D instrument in the tapping mode configuration with a fixed scan size of 10 μm × 10 μm. The magnitude of the surface roughness was quantified by calculating the root mean square (RMS) roughness of the surface profile. A determination of the directionality of the potential ripple features on the PR was performed by utilizing two distinct scan directions on each sample, one in each the parallel and perpendicular orientation relative to the sample edge. The AFM scans were taken at the sample edge and several points further from the edge, closer to the center of the sample, along with a scan at the center of the sample for reference. Further characterization of the acquired surface profiles was performed using a power spectral density (PSD) analysis. The PSD of a surface is a mathematical method decomposing the height profile into contributions from different spatial frequencies by Fourier transform of the autocorrelation function of the signal.[136] This process allows for identification of the spatial frequencies that can be found in the signal, and provides statistical information on the surface topography. The PR surface ripple formation and orientation were characterized and quantified by evaluating the AFM scans with PSD analysis in both the parallel and perpendicular directions relative to the sample edge. A one-dimensional PSD analysis was performed only in the horizontal direction on the AFM data, as this direction on an AFM apparatus corresponds with the fast-scanning axis, which is less susceptible to low frequency noise relative the slow-scanning axis in the vertical direction.[137]

5.3 Results

5.3.1 Thickness Uniformity

The uniformity of the etched surfaces relative to a pristine sample, as determined via the *ex situ* ellipsometric line scans, is shown in Fig. 5.2. The pristine sample, as expected, contains negligible thickness variation. For the samples processed at the three different substrate bias voltages, a consistent trend is an enhanced amount of thickness loss in the regions within approximately 1000 μm from the sample edge. This behavior near the sample edges, where the plasma sheath conformation begins to deviate from a normal angle to the surface, is in agreement with an elevated etch yield that is caused by ion bombardment at a shallower incident angle.[132] As a result, the area near the sample edge exhibits approximately 10-15% greater thickness loss compared to the central areas of the sample under all of the tested plasma conditions.

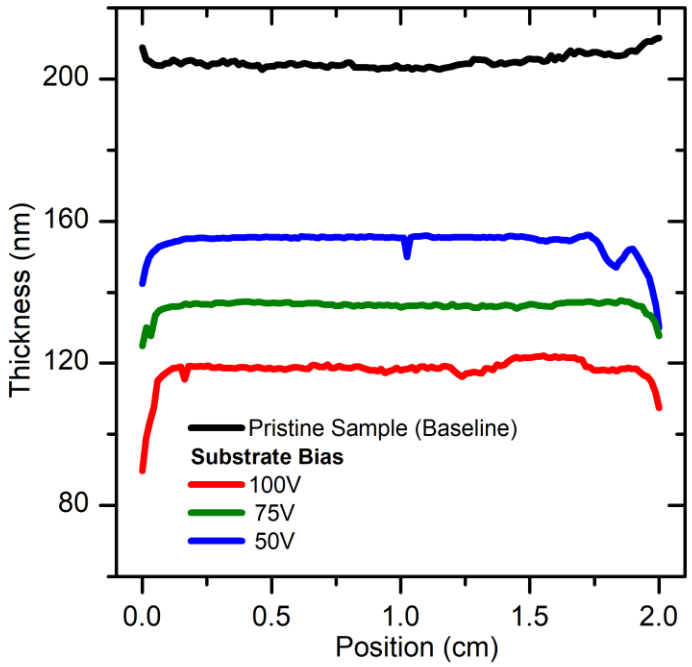

Figure 5.2. Line scans performed across the sample surface showing enhanced thickness loss under all conditions, near the sample edges, from shallower angle incident ion bombardment.

5.3.2 Surface Morphology of Ripple Features

5.3.2.1 Ripple Feature Directionality

Under the full range of tested substrate bias voltages, imaging of the sample surface via AFM observed the presence of ripple features that have an orientation that is parallel to the sample edge and perpendicular to the direction of incident ions. Figure 5.3 shows the most prominent ripple features that form at a -100 V bias, with the comparison between the parallel and perpendicular AFM scan directions, Fig. 5.3a,b, respectively, supporting the presence and directionality of the ripple features. To aid in distinguishing the ripple features in the AFM images, Fig. 5.3c,d provides complementary illustrations to Fig. 5.3a,b that depict the characteristic geometry of the ripple features.

Combined with the AFM scans of the surface, which qualitatively support the presence of the ripple features, three dimensional cross-sections across the entire two centimeter wide sample diameter in both the parallel and perpendicular directions, displayed in Fig. 5.4, also show a distinction in the characteristic wavelength of the surface morphology depending on the scan direction. The presence of a shorter characteristic wavelength in the peaks and valleys of the surface profile in the direction perpendicular to the ripple features compared to the wavelength of the surface profile in the direction parallel to the ripple features provides additional support for the spatial dependence of the directional ripple surface morphology.

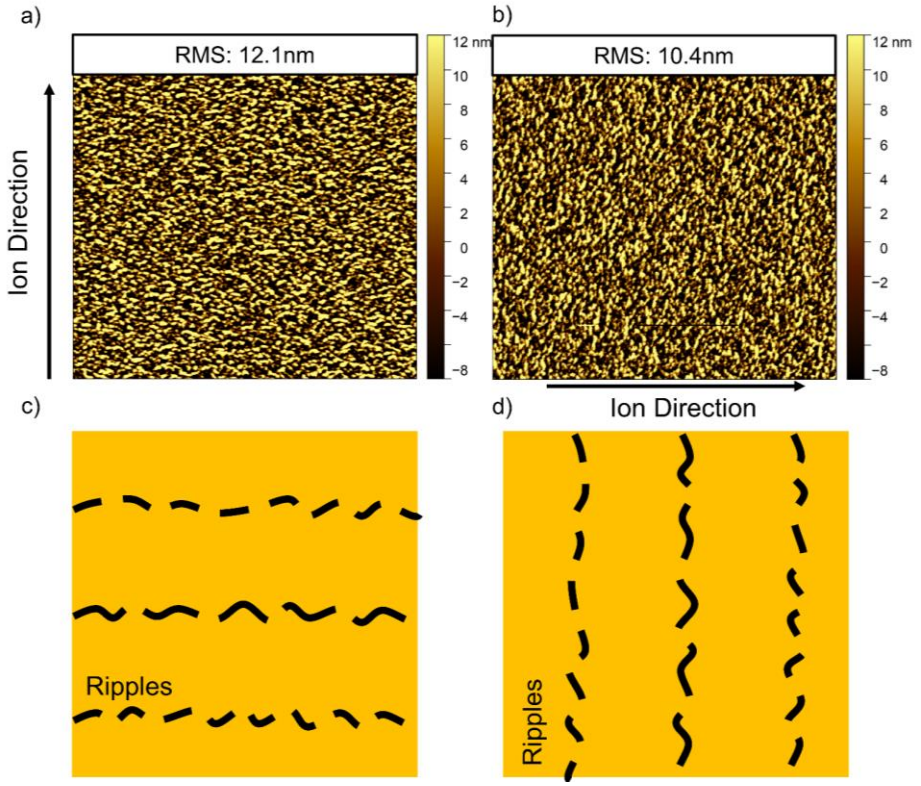

Figure 5.3. AFM images taken (a) parallel and (b) perpendicular to the sample edge for a process performed with a -100 V bias that show the prominent formation and directionality of the ripple features that are oriented perpendicular to the direction of incident ions. Simplified top-down sample illustration of the expected ripple features in the (c) parallel and (d) perpendicular scan directions relative to the sample edge.

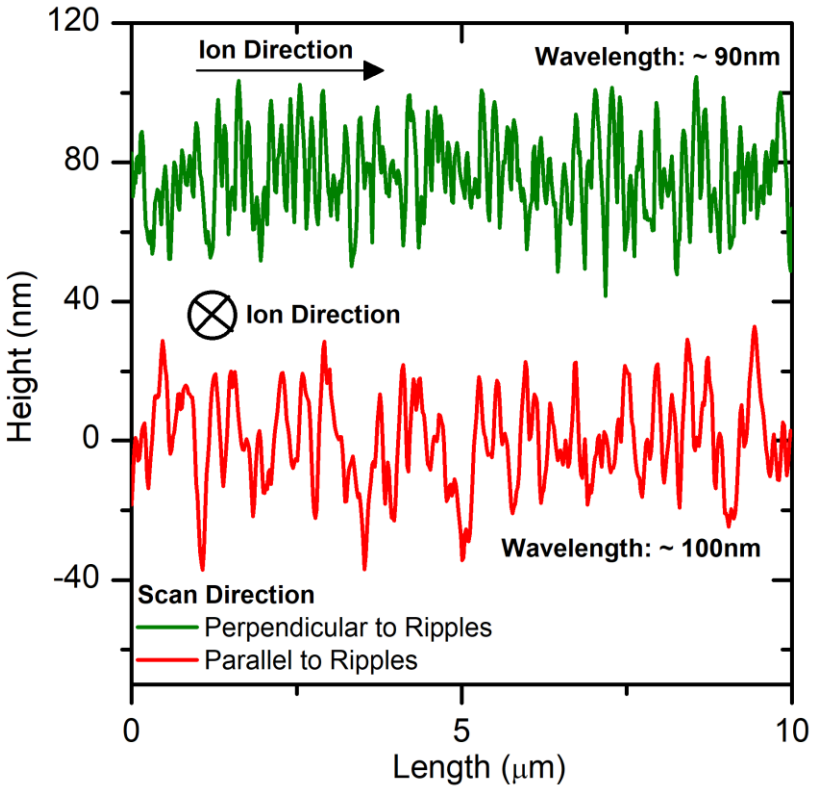

Figure 5.4. Cross-sections of the AFM scans for samples processed with a -100 V bias taken within 1 μm of the sample edge in orientations that are perpendicular and parallel to the ripple features. The relative directions of the incident ions are also indicated. The roughness profile in the direction perpendicular to the ripple features has a smaller characteristic wavelength relative to the profile in the direction that is parallel to the ripple features.

5.3.2.2 Spatial Extent of Ripple Features

To ascertain the length scale over which the variation in the incident ion angle takes place, AFM scans were performed at various distances from the sample edge, and the RMS roughness was calculated. Our hypothesis was that the magnitude of surface roughness will become constant with increasing distance from the sample edge once the electrostatic interaction of the plasma sheath diminishes sufficiently, such that the variation in incident ion angle is minimized. Correspondingly, the AFM scans displaying the spatial progression of the RMS roughness from the orientations

parallel and perpendicular to the ripple features, in Figures 5.5a and 5.6a respectively, highlight that the most significant decrease in the RMS roughness occurs within 1000 μm of the sample edge. Past a distance of 1000 μm, the decrease in the RMS roughness does not vary as significantly with distance compared to the variation in the RMS roughness in the initial 1000 μm from the sample edge. In the case of the perpendicular scans, the RMS roughness exhibits almost no variation past a distance of 1000 μm from the sample edge. The spatial variation in the RMS roughness likewise translates to the visibility of the ripple features. In both scan orientations, the ripple features are distinguishable from the background roughness near the sample edge (Fig 5.5a, Fig 5.6a), but become indistinguishable from the background roughness at the center of the sample (Fig 5.5b, Fig. 5.6b).

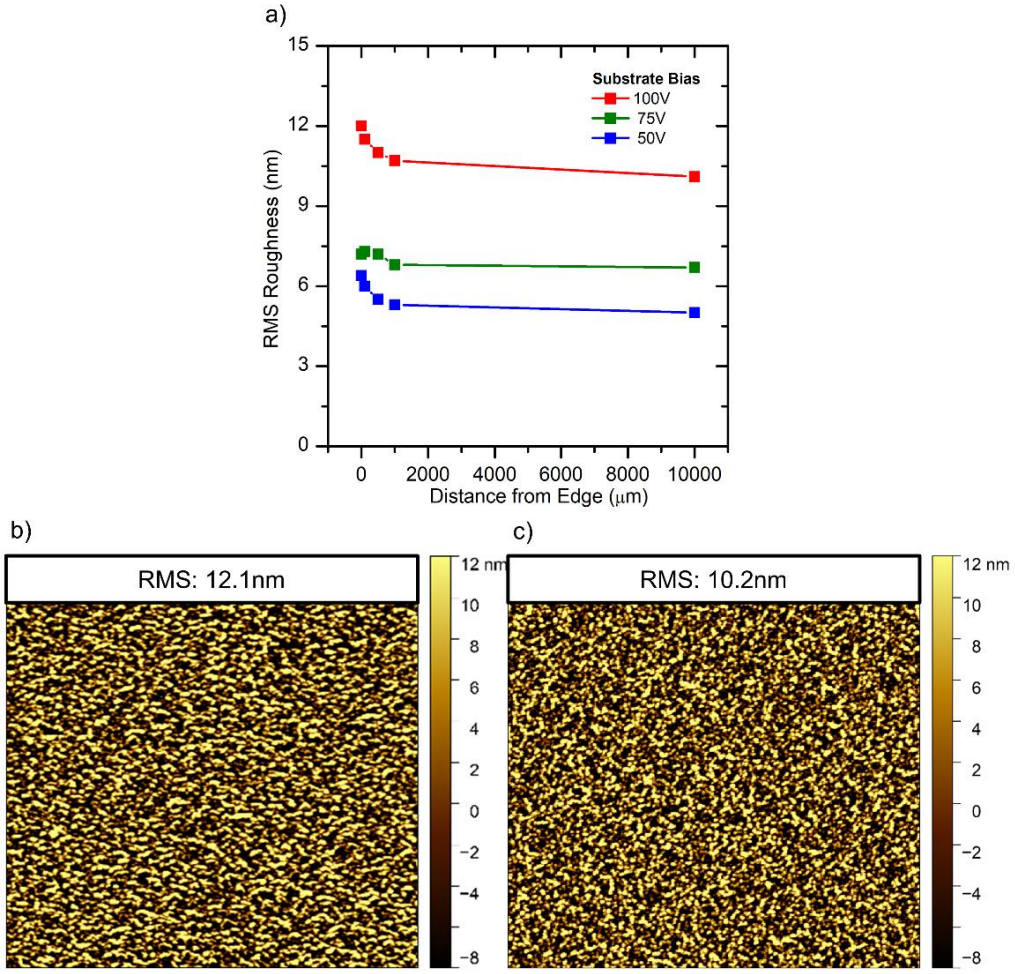

Figure 5.5. (a) Spatial dependence of the RMS roughness measured in the direction parallel to the ripple features and perpendicular to the direction of incident ions. The AFM images taken at a substrate bias of -100 V at (b) the sample edge and (c) sample center (1 cm from the sample edge) show that the ripple features are present near the sample edge, but diminish and are indistinguishable from the background roughness at the center of the sample.

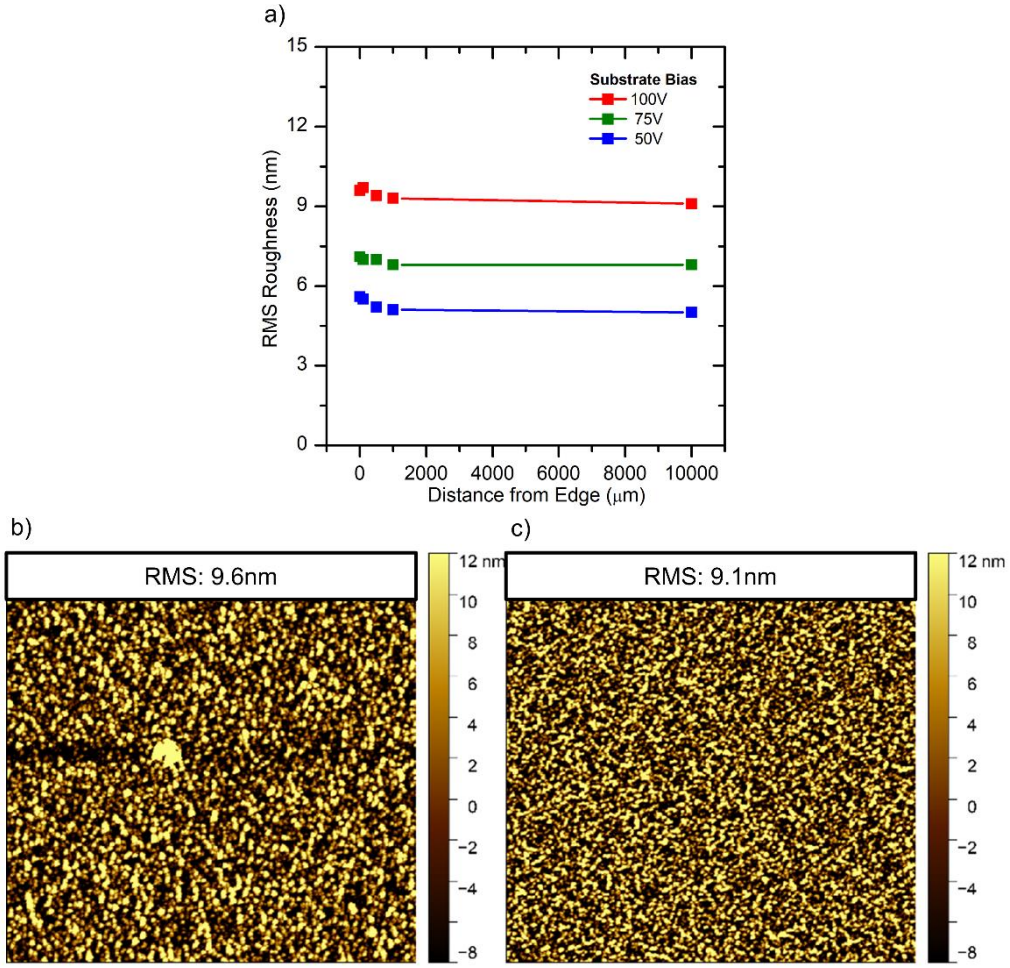

Figure 5.6. (a) Spatial dependence of the RMS roughness measured in the direction perpendicular to the ripple features and parallel to the direction of incident ions. The AFM images taken at a substrate bias of -100 V at (b) the sample edge and (c) sample center (1 cm from the sample edge) show that the ripple features are present near the sample edge, but diminish and are indistinguishable from the background roughness at the center of the sample.

5.3.3 PSD Analysis

PSD analysis provides the quantitative support to the qualitative data captured via the AFM analysis. Specifically, ripples present in the surface morphology potentially propagate at a characteristic wavelength that is distinct from the broad distribution of wavelengths that otherwise define a randomly distributed surface. Additionally, if the ripple features contribute a large amount of the sample height

variation relative to the background surface features, then the ripple features would account for a higher population of long-wavelength surface roughness. For the PSD analysis performed in the direction parallel to the sample edge and ripple feature orientation, as depicted in Fig. 5.7a, a consistently elevated population of low wavenumber (long wavelength) roughness begins to occur at points corresponding to 100 μm from the sample edge and closer for all the tested substrate biases (Fig. 5.7b-d). This observation supports the idea of prominent surface morphology being present in the region immediately adjacent to the sample edge. Conversely, though, the PSD analysis performed for the scan in the direction perpendicular to the sample edge and ripple feature orientation, as depicted in Fig. 5.8a, shows a roughness distribution that does not vary as a function of the distance from the sample edge (Fig. 5.8b-d). Combined with the findings of the AFM images and cross sections, the variation in the PSD analysis suggests that there is a distinct contribution to the population of long-wavelength roughness near the sample edge when the PSD measurement is taken parallel to the ripple features compared to the PSD measurement taken perpendicular to the ripple features, which does not exhibit a distinct contribution to the population of long-wavelength roughness near the sample edge.

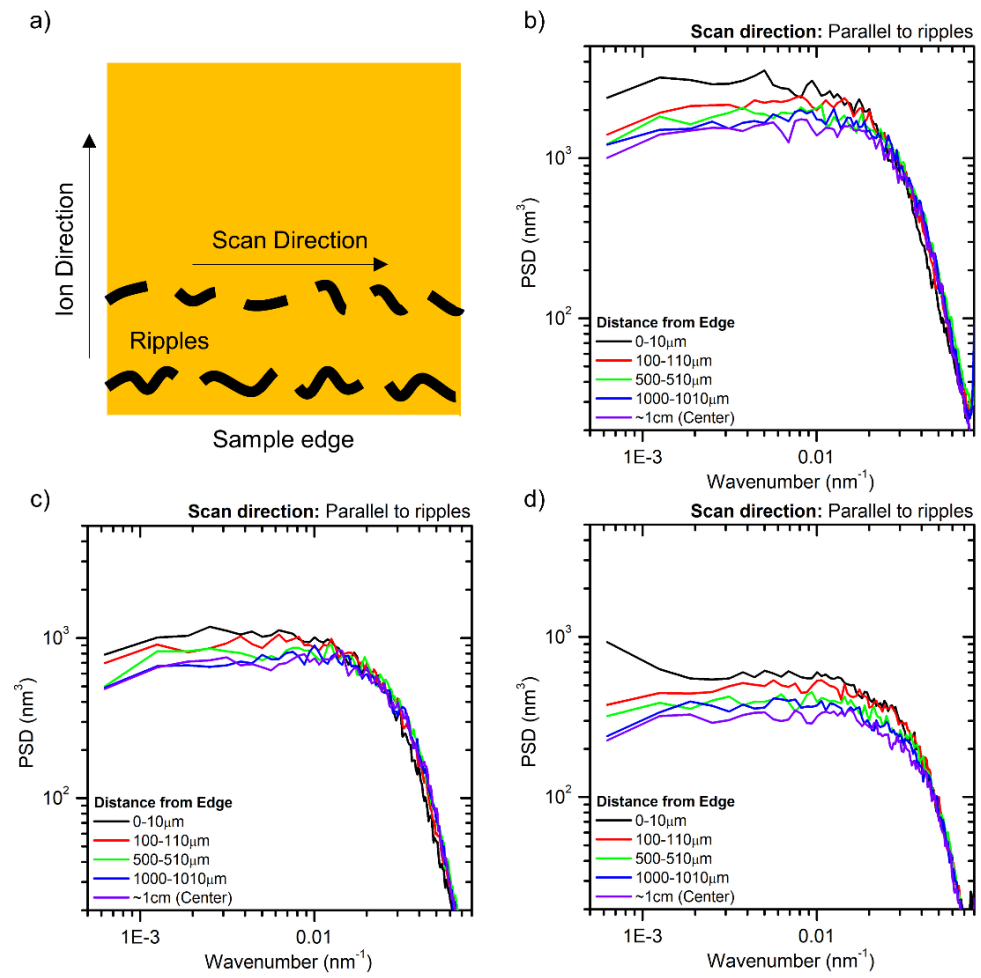

Figure 5.7. (a) Top-down view illustration of the AFM scan orientation and direction for the PSD analysis. The PSD analysis of the AFM scans performed parallel to the sample edge for samples processed at (b) -100 V, (c) -75 V, and (d) -50 V substrate biases.

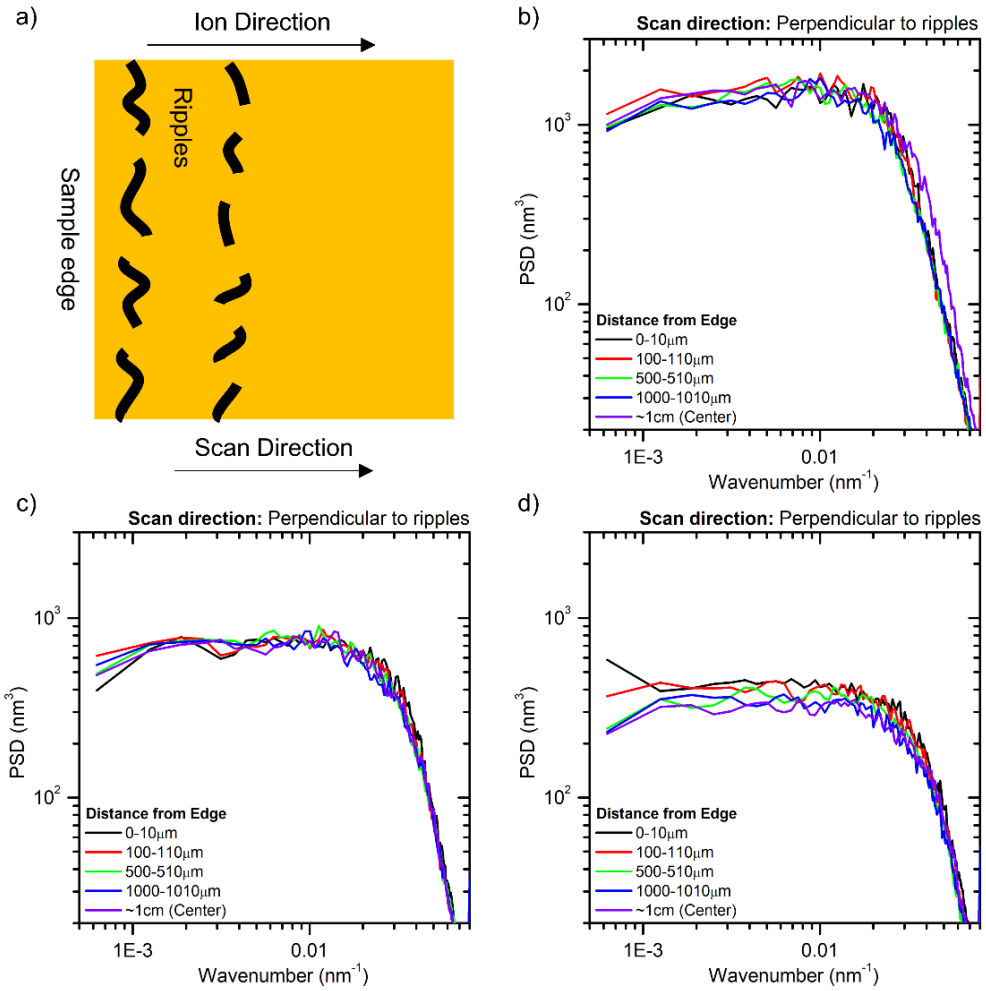

Figure 5.8. (a) Top-down view illustration of the AFM scan orientation and direction for the PSD analysis. The PSD analysis of the AFM scans performed perpendicular to the sample edge for samples processed at (b) -100 V, (c) -75 V, and (d) -50 V substrate biases.

5.4 Discussion

5.4.1 Properties of the Plasma Sheath

In the scope of plasma-based wafer processing applications, the Debye length is a critical parameter in the consideration of process uniformity and the length scale over which the conformation of the plasma sheath significantly contributes to a variation in the incident ion angle. The electrostatic plasma-surface interaction

produced by the plasma sheath near the sample edge extends on the length scale of the Debye length, and has a diminishing effect past the length scale of several Debye lengths. The magnitude of the Debye length is strongly dependent on processing parameters such as the pressure and plasma composition, because those impact the plasma density and electron temperature. Equation 5.1 shows the expression for the Debye length, λ_D, in terms of its constituent components, the electron temperature, T_e, and the electron density, n_e, along with the physical constants ε_0, the permittivity of free space, k, the Boltzmann constant, and q_e, the charge of an electron.

$$\lambda_D = \sqrt{\frac{\varepsilon_0 k T_e}{n_e q_e^2}} [meters] \tag{5.1}$$

For the experimental conditions used in this work, namely a chamber pressure of 5 mTorr, the corresponding electron temperature and electron density, as determined via Langmuir probe in a previous study in the same processing chamber, are 3.2 eV and 5×10^{10} cm^{-3}, respectively.[126] Using these parameters, the Debye length in our study is approximately 60 μm. Therefore, the expectation is that the most prominent development of surface etching and morphological effects from incident off-normal ions would occur over multiples of this length scale and begin to diminish past several Debye lengths, where the conformation of the plasma sheath becomes more parallel to the sample surface, thus reducing the amount of off-normal ions interacting with the surface. The results in Figures 5.2, 5.5, and 5.6 mostly follow this expectation, as the greatest change in the surface roughness magnitude and amount of thickness etched occurs within approximately 100 μm, or one to two Debye lengths, of the sample edge. However, past this distance, further measurable changes in the thickness profile and surface roughness magnitude are still observed,

implying that the effects of the off-normal ions extend considerably past the Debye screening length. Thus, the Debye screening length is a more useful indicator for the length scale over which the greatest changes from the impacts of the off-incident ions occur rather than as an indicator for the length scale describing the full extent of any spatial variation. Only at a distance greatly beyond the Debye length, approximately 1000 μm from the sample edge, does the variation in the roughness magnitude and amount of material etched not change significantly across the sample surface, implying that the sheath conformation is such that there is no longer a significant impact from off-normal ions.

5.4.2 Properties of the Ripple Features

Understanding the extent and the mechanisms behind the formation of the ripple features is significant for maintaining the critical dimension of patterned features in semiconductor device manufacturing.[138] The theory behind the physical phenomena that generate the ripple features was first proposed by Bradley and Harper[130], and since has been supported by numerous modeling and experimental works. This theory posits that the ripple features form from an instability as a result of the variation in the sputtering yield along the local sample surface curvature.[139,140] In the context of the 193 nm PR material, the initial perturbation of the surface that leads to nonuniformity originates from the synergistic interaction between ions and vacuum ultraviolet (VUV) photons.[8–10,19] The corresponding development of nonuniform surface roughness results in regions of nonuniform etching that in turn influence the etching impact of later arriving ions. The enhanced etch yield in these initial regions promotes additional local etching, which ultimately gives rise to the formation and

propagation of the ripple features.[141] The susceptibility of the organic PR material to morphology changes from ion-induced bond scissioning contributes to the prominence of the ripple features in the PR material compared to inorganic materials, such as SiO_2, and allows for the ripple features to be distinguished from the background surface roughness, as shown in Fig. 5.3.[142] As the incidence of off-normal ions decreases, etching becomes more uniform. This effect leads to more uniform surface morphology past a distance of 1000 μm from the sample edge, where the ripple structure becomes disordered and indistinguishable from the background roughness. The energetic ion bombardment leads to the prominence of a graphitic surface layer that, under uniform ion bombardment, eventually smoothens the ripple features via a volume diffusion mechanism.[143,144]

The PSD analysis of the surface morphology correlates the spatial extent of the characteristic roughness wavelengths to the developed ripple features. One key consideration of the PSD analysis at various distances from the sample edge is that the magnitude of the ripple wavelengths is highly dependent on the ion fluence.[134,142] Because the ion fluence in our experimental setup only depends on the processing time, and is independent of the substrate bias, the processing time was held at two minutes for processing of the samples. For the PSD analysis performed in the direction parallel to the sample edge, the roughness wavelength distribution of the surface morphology is nearly identical for all the tested substrate bias magnitudes past at a distance past 100 μm from the sample edge. This finding indicates that the presence of any ripples is not significant enough to be distinct from the background roughness distribution. Conversely, at a distance of 100 μm and closer to the sample

edge, the increase in the PSD magnitude at wavenumbers below 0.02 nm^{-1} in the parallel scan direction signifies an increased population of long-wavelength (>50 nm) roughness, which can be attributed to the presence of the ripple features. However, in the perpendicular scan direction, the roughness distribution does not change as a function of the sample edge distance. This contrast in the observed behavior relative to the parallel scan direction also lends support to the presence of a directional morphology in the form of the ripple features on the sample surface. The cross-section of the sample taken at the sample edge, Fig. 5.4, which shows the characteristic shorter wavelength of the height profile in the perpendicular scan direction compared to the longer wavelength of the height profile in the parallel scan direction, corresponds to the findings of the PSD analysis. In the PSD analysis, the scan performed perpendicular to the ripple features observed a lower population of long-wavelength roughness compared to the scan performed parallel to the ripple features, therefore the perpendicular scan orientation corresponds with the presence of a shorter characteristic wavelength relative to that of the parallel scan orientation.

5.5 Summary and Conclusions

In this work, we evaluated the extent of the local perturbation of the plasma sheath and the corresponding spatial-dependent impact on the etching and morphological evolution of a 193 nm PR material from off-normal ion impingement. A combination of ellipsometric and AFM measurements across the sample surface quantified a 10-15% enhancement in the amount of thickness etched within 1000 μm of the sample edge relative to the center of the samples along with a corresponding development of ripple features in the surface morphology. The magnitude of the

developed surface roughness, which is related to the amount of thickness etched, similarly has a maximum at the sample edge. By 1000 μm from the sample edge, the roughness is comparable to that at the center of the sample. These findings support the interpretation that under the chosen processing conditions, the conformation of the plasma sheath and the corresponding Debye length results in the most significant impacts to the thickness etched and surface morphology within the initial 100 μm from the sample edge with the majority of the impact from off-normal ion impingement extending up to 1000 μm of the sample edge. Furthermore, the AFM analysis found that the off-normal ion bombardment of the PR material produces ripple features that are directionally oriented perpendicular to the direction of incident ions and propagate towards the sample interior. As the sample etching behavior becomes more uniform near the center of the sample as off-normal ion impingement becomes less prominent, the ripple features diminish and become indistinguishable from the background surface roughness. Characterization of the surface roughness distribution via PSD analysis additionally confirms an enhanced population of >50 nm wavelength roughness, only in the direction parallel to the sample edge, that is distinguishable from the background roughness distribution at a distance within 100 μm of the sample edge. This analysis combined with the cross sections of the surface morphology identify the prominence, structure, orientation, and spatial extent of the ripple features on the PR material.

Overall, this work investigated the impacts of off-normal ion impingement on the etching and surface roughening behaviors of a 193 nm PR. The results elucidate the scope of the impact on the etching uniformity and the evolution of the surface

morphology which forms characteristic ripple features. The findings of this work provide key insights into applications such as large-scale wafer processing where the local sample geometry presents potential implications on the etching uniformity due to the plasma-surface interaction. Further work can be done to improve the understanding of the relationship between the length scale of the Debye length and the observed spatial extent of ion impacts on the sample surface.

Acknowledgments

The authors gratefully acknowledge financial support of this work by Samsung Electronics.

Chapter 6: Conclusions and Future Work

The continuous push for advancements in the field of semiconductor manufacturing, through the development of more selective processing techniques and new photoresist (PR) materials for enabling the fabrication of features with increasingly smaller dimensions and pitches, has underscored the need for understanding the fundamental mechanisms which govern the interactions between plasma-based etch processes and PR materials. This work has strived to address the challenges presented in the field by developing an approach under which the main interactions between plasma species and PR materials can be interpreted and related to key process performance parameters including the etching and surface roughening behaviors. With the fundamental understanding of the interrelationships between plasma species, PR materials, and the corresponding process behaviors towards specific industrial motivations, we have directly applied the gained knowledge to address several key industrial objectives for both improving the etching behavior of PR materials in an advanced pattern transfer process as well as determining the influences of sample layouts on the uniformity of etch processes.

In Chapter 2, we identified the dominant role of ions in an energetic inert argon-based plasma process in modifying the surface of a 193 nm PR material to form a discrete DAC layer. The formation of this layer, which originates from the scissioning of oxygen-, and hydrogen-containing bonds within the PR composition, produces a surface layer that provides a significantly greater etch resistance than the underlying native PR material. By combining *in situ* ellipsometric measurements with secondary XPS characterization, we developed a baseline ellipsometric model for

tracking and interpreting the time-dependent surface modification and thickness evolution of a 193 nm PR material during a plasma process. Through the interpretation of the raw data via ellipsometric modeling, we found that the attainment of steady-state etching behavior in the PR material is accompanied by the formation of a DAC layer with a thickness between three and four nanometers. The selective depletion of this layer via a reactive plasma chemistry does not impact the etching behavior of the underlying bulk layer until approximately more than 40% of the original thickness is depleted, at which point the etch rate of the bulk layer increases by almost a factor of ten as the DAC layer is fully depleted. This initial study highlighted the importance of the DAC layer in controlling the etching behavior of a PR material.

In Chapter 3, we expanded the scope of our characterization approach to investigate the impacts on the DAC layer and resulting PR etching behavior under a plasma composition that contains reactive FC species, a condition that is more appropriate for industrial applications involving pattern transfer processes. Using the same setup as in Chapter 2, we exposed the steady-state DAC layer on the PR surface to various durations of the FC precursor octafluorocyclobutane (C_4F_8) and utilized *in situ* ellipsometry with secondary XPS characterization to develop an improved model for interpreting the interaction between the FC species and the DAC layer and the resulting impact on the PR etching behavior. Through the XPS characterization, we found that the FC species enrich the DAC layer with fluorine content. Modifying our initial ellipsometric model with this information, we interpreted the raw data from this experiment and postulated that the interaction of the FC species with the DAC

layer depletes the layer via a mechanism where the FC species simultaneously diffuse into the DAC layer and partially react with it, reducing its thickness. The diffusion of fluorine into the DAC layer results in the remaining DAC layer to attain an optical property that is intermediate of that of a pristine DAC layer or the bulk PR material. However, as long as a sufficient thickness of the modified DAC layer remains, it still provides additional etch resistance to the PR material. The results of this study established an understanding of how FC species modify the DAC layer and the implications for a plasma etching process with PR materials that utilizes a reactive FC-based plasma composition.

In Chapter 4, we applied the understanding of the PR modification behavior towards an industrial objective that required the establishment of a high etching selectivity of a substrate material, such as SiO_2, relative to PR material. For this study, we utilized a modern model EUV PR material, due to its increasing relevance in industry for the patterning of feature sizes below ten nanometers. Since an appreciable etching of SiO_2 requires a reactive gas chemistry, we utilized both octafluorocyclobutane (C_4F_8) and trifluoromethane (CHF_3) as reactive precursor gases. To establish the required surface modification for controlled PR etching, which otherwise does not form under a continuous process with a reactive plasma chemistry, we used an ALE process that intrinsically supports a wide parameter space for controlling the ion energy, FC deposition thickness, and etch step length, for improving the relative etching behaviors of the EUV PR and SiO_2. By systematically evaluating the ALE parameters, we found that the combination of moderately energetic ion bombardment (40V) combined with an etch step length of 10 s

progressively forms a fluorine-rich modified layer on the PR surface, which after approximately six cycles results in a near cessation of any etching of the PR material. At the same time, the etching of SiO_2 continues unimpeded in a steady-state manner, thus resulting in a very high SiO_2/PR etching selectivity. Secondary characterization via XPS and AFM supported the finding of a fluorine-rich nature of the modified layer and the fact that the formation of the modified layer for etch control does not significantly increase the magnitude of surface roughness, respectively. Additionally, characterization via ATR-FTIR identified the stability of the aromatic functional groups in the PR composition under a plasma exposure as well as the enrichment of the PR composition with fluorine species. The findings of this work highlight the potential use of an ALE process with PR materials to achieve high relative etching selectivities, which are required in pattern transfer applications for the fabrication of current devices.

In Chapter 5, we investigated the impact of off-normal ions, which occur due to the variation in the local plasma sheath conformation, on the etching uniformity and surface roughness evolution of a PR material at various ion energies. By using a combination of *ex situ* ellipsometry and AFM measurements at various points across the sample surface, we concluded that for the experimental conditions used, the extent of significant off-normal ion impingement extends for a distance approximately 1000 μm from the sample edge, with the greatest changes occurring within 100 μm from the sample edge. Within 1000 μm from the sample edge, the amount of sample etching is approximately 10-15% greater and has an enhanced magnitude of surface roughness compared to that of areas near the center of the sample. Since for these

conditions the Debye length is on the order of 60 μm, the results show that the extent of the impact from off-normal ions extends significantly beyond the distance of the electrostatic effect interaction between the plasma and the sample surface. In addition, we found that the off-normal ions produce a characteristic long wavelength (>50 nm) surface morphology in the form of ripple features near the sample edges that dissipate in the regions near the center of the sample when there no longer is a significant incidence of off-normal ions. The ripple features possess a characteristic directionality that is perpendicular to the direction of the incoming ions and propagate in the direction away from the sample edge. The results of this study highlight the extent and prominence of the etching and surface morphology impacts of the off-normal ions that originate from the plasma sheath conformation around the local sample geometry.

In summary, this research has supplemented the knowledge of PR materials in plasma etching applications by identifying the relationships between plasma species and the PR-composition-dependent modifications that impact the corresponding process properties, such as the etching and surface roughening behaviors. The work done in Chapters 4 and 5 has shown the applicability of utilizing the knowledge of the plasma-photoresist interaction behaviors to address relevant etching challenges in the semiconductor processing field. Even though our research was focused on PR materials, a fundamental strength of our characterization and modeling approach is that it can applied to any subset of materials for investigating plasma-surface interactions.

Although we attempted to be as detailed as possible in our studies of the plasma-photoresist interactions, there remain several questions that arise due to both the specific scope of our work as well as some of the experimental limitations that were encountered. The first key question regards the universality of the properties that were observed for the DAC layer in Chapter 2. Because the scope of our work was focused on one PR material, a 193 nm PR, the question arises whether a DAC layer with a similar composition and etch-mediating properties would form under an organic material with a different chemical composition. Although the scissioning impact from ion bombardment is universal among polymer materials, it is possible that the degree of scissioning and the resulting density and thickness of the DAC layer may vary depending on the composition of the native material. Therefore, the magnitude of the variation in the etching behavior as a result of the change in DAC layer thickness may not be the same for different materials and presents a good motivation for a systematic study into other materials.[145] A second question pertains to the interpretation of the DAC layer modification which occurs from the FC species in Chapter 3. Because the simultaneous modification and depletion of the DAC layer from FC species is a highly dynamic process with more variables than what can be determined directly via a fit to an ellipsometric model, the construction of the model required several assumptions to be made regarding the optical properties of the modified layer. Although the XPS characterization indicated a fluorine-rich nature of the modified DAC layer, it did not provide any information on the refractive index or density of this layer. Therefore, we made an assumption of the optical properties of the modified DAC layer based on trial fits of the ellipsometric model. Improving the

accuracy of our model and resulting interpretation of the PR response can be done via additional characterization techniques, such as secondary ion mass spectroscopy (SIMS), that can determine the compositional depth profile of the fluorine species, which can then be used to solve for the optical properties of the modified layer. Another key question that arises for the application-oriented studies in Chapters 4-5 pertains to the applicability of the work to patterned samples, which is the end product relevant in industrial applications. Due to the requirement of uniform blanket samples for ellipsometric measurements to be accurate, an analysis was not performed on patterned samples. Therefore, while we expect our conclusions to hold for the overall etching behavior and morphological evolution on the top surface of any patterned features, there likely will be additional impacts that will need to be considered for the etching and profile evolution of the sidewalls of any three-dimensional structures. The orientation of the sidewall relative to the incoming ions and reactive species and the affinity of the reactive species to adhere to the sidewalls, for example, may result in uneven etching and passivation relative to the top surfaces. Therefore, expanding the scope of the work to patterned features is the logical next step for future work.

The fundamental research approach established in this dissertation for evaluating plasma-surface interactions presents numerous opportunities for expanding the scope and applicability of the work in future studies. As one of the main strengths of our approach is the ability to identify subtle trends from the combination of data from multiple characterization methods, applying this approach to a wider set of PR and other relevant materials, such as SiO_2, Ge, or Si_3N_4, can greatly increase the

understanding of the time-dependent etching behaviors of these materials under a plasma process. Another good possibility for future work is applying the application-oriented work on patterned samples. The completed work has established a broad understanding of the etching and morphological behaviors on uniform blanket samples, however relevant devices in industry involve patterned features consisting of three-dimensional structures. Broadening the scope of the work to investigate the fidelity of patterned features under the ALE process conditions outlined in Chapter 4 and the impacts on the etch uniformity of the patterned features via the approach in Chapter 5 represents the most meaningful extension of the work to encompass relevant industrial applications.

Bibliography

[1] H. Geng, *Semiconductor Manufacturing Handbook, Second Edition*, 2nd ed. (McGraw Hill Professional, 2017).
[2] C. Mack, *Fundamental Principles of Optical Lithography: The Science of Microfabrication* (John Wiley & Sons, 2007).
[3] G.S. Oehrlein, R.J. Phaneuf, and D.B. Graves, J. Vac. Sci. Technol. B **29**, 010801 (2011).
[4] S. Engelmann, R.L. Bruce, T. Kwon, R. Phaneuf, G.S. Oehrlein, Y.C. Bae, C. Andes, D. Graves, D. Nest, E.A. Hudson, P. Lazzeri, E. Iacob, and M. Anderle, J. Vac. Sci. Technol. B **25**, 1353 (2007).
[5] L. Azarnouche, E. Pargon, K. Menguelti, M. Fouchier, O. Joubert, P. Gouraud, and C. Verove, J. Vac. Sci. Technol. B **31**, 012205 (2013).
[6] J.T. Fourkas and J.S. Petersen, Phys. Chem. Chem. Phys. Phys. Chem. Chem. Phys **16**, 8731 (2014).
[7] F. Weilnboeck, N. Kumar, G.S. Oehrlein, T.-Y. Chung, D. Graves, M. Li, E. a. Hudson, and E.C. Benck, J. Vac. Sci. Technol. B **30**, 031807 (2012).
[8] D. Nest, T.-Y. Chung, D.B. Graves, S. Engelmann, R.L. Bruce, F. Weilnboeck, G.S. Oehrlein, D. Wang, C. Andes, and E.A. Hudson, Plasma Process. Polym. **6**, 649 (2009).
[9] R.L. Bruce, F. Weilnboeck, T. Lin, R.J. Phaneuf, G.S. Oehrlein, B.K. Long, C.G. Willson, and A. Alizadeh, J. Vac. Sci. Technol. B **29**, 041604 (2011).
[10] T.-Y. Chung, D.B. Graves, F. Weilnboeck, R.L. Bruce, G.S. Oehrlein, M. Li, and E.A. Hudson, Plasma Process. Polym. **8**, 1068 (2011).
[11] R.L. Bruce, S. Engelmann, T. Lin, T. Kwon, R.J. Phaneuf, G.S. Oehrlein, B.K. Long, C.G. Willson, J.J. Végh, D. Nest, D.B. Graves, and A. Alizadeh, J. Vac. Sci. Technol. B **27**, 1142 (2009).
[12] T.-Y. Chung, D. Nest, D.B. Graves, F. Weilnboeck, R.L. Bruce, G.S. Oehrlein, D. Wang, M. Li, and E.A. Hudson, J. Phys. D. Appl. Phys. **43**, 272001 (2010).
[13] T. Ohfuji, M. Endo, M. Takahashi, T. Naito, T. Tatsumi, K. Kuhara, and M. Sasago, SPIE Proc. **3333**, 595 (1998).
[14] H. Gokan, S. Esho, and Y. Ohnishi, J. Electrochem. Soc. **130**, 143 (1983).
[15] M. Sumiya, R. Bruce, S. Engelmann, F. Weilnboeck, and G.S. Oehrlein, J. Vac. Sci. Technol. B **26**, 1978 (2008).
[16] M. Sumiya, R. Bruce, S. Engelmann, F. Weilnboeck, and G.S. Oehrlein, J. Vac. Sci. Technol. B **26**, 1637 (2008).
[17] M. Sumiya, R. Bruce, S. Engelmann, F. Weilnboeck, and G.S. Oehrlein, J. Vac. Sci. Technol. B **26**, 1647 (2008).
[18] N. Vandencasteele and F. Reniers, J. Electron Spectros. Relat. Phenomena **178**–**179**, 394 (2010).
[19] R.L. Bruce, F. Weilnboeck, T. Lin, R.J. Phaneuf, G.S. Oehrlein, B.K. Long, C.G. Willson, J.J. Vegh, D. Nest, and D.B. Graves, J. Appl. Phys. **107**, 084310 (2010).
[20] D. Metzler, F. Weilnboeck, S. Engelmann, R.L. Bruce, and G.S. Oehrlein, J. Vac. Sci. Technol. B **34**, 041604 (2016).
[21] C.T. Carver, J.J. Plombon, P.E. Romero, S. Suri, T.A. Tronic, and R.B. Turkot,

ECS J. Solid State Sci. Technol. **4**, N5005 (2015).
[22] S.A. Lynn, N. MacGearailt, and J.V. Ringwood, Proc. IEEE Int. Conf. Control Appl. 1658 (2012).
[23] D. Metzler, F. Weilnboeck, S.C. Hernández, S.G. Walton, R.L. Bruce, S. Engelmann, L. Salamanca-Riba, and G.S. Oehrlein, J. Vac. Sci. Technol. B **33**, 051601 (2015).
[24] C. Li, D. Metzler, C.S. Lai, E.A. Hudson, and G.S. Oehrlein, J. Vac. Sci. Technol. A Vacuum, Surfaces, Film. **34**, 041307 (2016).
[25] X. Li, L. Ling, X. Hua, G.S. Oehrlein, Y. Wang, and H.M. Anderson, J. Vac. Sci. Technol. A **21**, 1955 (2003).
[26] X. Hua, S. Engelmann, G.S. Oehrlein, P. Jiang, P. Lazzeri, E. Iacob, and M. Anderle, J. Vac. Sci. Technol. B **24**, 1850 (2006).
[27] D. Metzler, R.L. Bruce, S. Engelmann, and E.A. Joseph, J. Vac. Sci. Technol. A **32**, 020603 (2014).
[28] K.-Y. Lin, C. Li, S. Engelmann, R.L. Bruce, E.A. Joseph, D. Metzler, and G.S. Oehrlein, J. Vac. Sci. Technol. A **36**, 040601 (2018).
[29] G.S. Oehrlein, D. Metzler, and C. Li, ECS J. Solid State Sci. Technol. **4**, N5041 (2015).
[30] F. Weilnboeck, R.L. Bruce, S. Engelmann, G.S. Oehrlein, D. Nest, T.-Y. Chung, D. Graves, M. Li, D. Wang, C. Andes, and E.A. Hudson, J. Vac. Sci. Technol. B **28**, 993 (2010).
[31] T. Schwarz-Selinger, A. von Keudell, and W. Jacob, J. Appl. Phys. **86**, 3988 (1999).
[32] R.L. Bruce, T. Lin, R.J. Phaneuf, G.S. Oehrlein, W. Bell, B. Long, and C.G. Willson, J. Vac. Sci. Technol. B **28**, 751 (2010).
[33] T.E.F.M. Standaert, M. Schaepkens, N.R. Rueger, P.G.M. Sebel, G.S. Oehrlein, and J.M. Cook, J. Vac. Sci. Technol. A **16**, 239 (1998).
[34] B. Landkammer, A. von Keudell, and W. Jacob, J. Nucl. Mater. **264**, 48 (1999).
[35] G.S. Oehrlein, T. Schwarz-Selinger, K. Schmid, M. Schlüter, and W. Jacob, J. Appl. Phys. **108**, 043307 (2010).
[36] F. Weilnboeck, N. Fox-Lyon, G.S. Oehrlein, and R.P. Doerner, Nucl. Fusion **50**, 25027 (2010).
[37] F. Weilnboeck, D. Metzler, N. Kumar, G.S. Oehrlein, R.L. Bruce, S. Engelmann, and N. Fuller, Appl. Phys. Lett. **99**, 261501 (2011).
[38] S. Engelmann, R.L. Bruce, F. Weilnboeck, G.S. Oehrlein, D. Nest, D.B. Graves, C. Andes, and E.A. Hudson, Plasma Process. Polym. **6**, 484 (2009).
[39] N. Krstulović, I. Labazan, S. Milošević, U. Cvelbar, A. Vesel, and M. Mozetič, J. Phys. D. Appl. Phys. **39**, 3799 (2006).
[40] O. Joubert, C. Fiori, J.C. Oberlin, P. Paniez, J. Pelletier, M. Pons, T. Vachette, and A. Weill, J. Appl. Phys. **69**, 1697 (1991).
[41] C. Vivensang, G. Turban, E. Anger, and A. Gicquel, Diam. Relat. Mater. **3**, 645 (1994).
[42] J.J. Vegh, D. Nest, D.B. Graves, R. Bruce, S. Engelmann, T. Kwon, R.J. Phaneuf, G.S. Oehrlein, B.K. Long, and C.G. Willson, Appl. Phys. Lett. **91**, (2007).
[43] J.F. Ziegler, M.D. Ziegler, and J.P. Biersack, Nucl. Instruments Methods Phys. Res. Sect. B Beam Interact. with Mater. Atoms **268**, 1818 (2010).

[44] A. von Keudell, W. Jacob, and W. Fukarek, Appl. Phys. Lett. **66**, 1322 (1995).
[45] J. Davenas, P. Thevenard, G. Boiteux, M. Fallavier, and X.L. Lu, Nucl. Instruments Methods Phys. Res. **46**, 317 (1990).
[46] M.N. Kawaguchi, J.S. Papanu, B. Su, M. Castle, and A. Al-Bayati, J. Vac. Sci. Technol. B **24**, 657 (2006).
[47] C. Koike, H. Hasegawa, and A. Manabe, Astrophys. Space Sci. **67**, 495 (1979).
[48] C. Hata, M. Kamo, and Y. Sato, in *Abstr. from First Int. Conf. New Diam. Sci. Technol.* (Tokyo, 1988), pp. 116–117.
[49] A. von Keudell and W. Jacob, J. Appl. Phys. **79**, 1092 (1996).
[50] W. Jacob, Thin Solid Films **326**, 1 (1998).
[51] C. Hopf, M. Schlüter, T. Schwarz-Selinger, U. von Toussaint, and W. Jacob, New J. Phys. **10**, 093022 (2008).
[52] C. Hopf, A. von Keudell, and W. Jacob, J. Appl. Phys. **94**, 2373 (2003).
[53] C. Hopf, A. von Keudell, and W. Jacob, Nucl. Fusion **42**, L27 (2002).
[54] D.Y. Yun, W.S. Choi, Y.S. Park, and B. Hong, Appl. Surf. Sci. **254**, 7925 (2008).
[55] Y. Koval, J. Vac. Sci. Technol. B **22**, 843 (2004).
[56] H.G. Tompkins, *A User's Guide to Ellipsometry* (Dover Publications, 2006).
[57] M. Massi, R.D. Mansano, H.S. Maciel, C. Otani, P. Verdonck, and L.N.B.M. Nishioka, Thin Solid Films **344**, 381 (1999).
[58] C.H. Yi, T.W. Kim, K. Suzuki, K. Ikeda, J. Fernando, D. Chubachi, S. Halder, R. Vos, S. Samukawa, R. Kaneko, and S. Oguchi, Jpn. J. Appl. Phys. **28**, 2130 (1989).
[59] J. Zekonyte, V. Zaporojtchenko, and F. Faupel, Nucl. Instruments Methods Phys. Res. Sect. B Beam Interact. with Mater. Atoms **236**, 241 (2005).
[60] C. Corbella, S. Große-Kreul, and A. von Keudell, Plasma Process. Polym. **12**, 564 (2015).
[61] J.J. Vegh, D. Nest, D.B. Graves, R. Bruce, S. Engelmann, T. Kwon, R.J. Phaneuf, G.S. Oehrlein, B.K. Long, and C.G. Willson, J. Appl. Phys. **104**, 034308 (2008).
[62] N. Fox-Lyon, G.S. Oehrlein, N. Ning, and D.B. Graves, J. Appl. Phys. **110**, 1 (2011).
[63] A. Pranda, S.A. Gutierrez Razo, Z. Tomova, J.T. Fourkas, and G.S. Oehrlein, J. Vac. Sci. Technol. A Vacuum, Surfaces, Film. **36**, 021304 (2018).
[64] M. Schvartzman, A. Mathur, Y. Kang, C. Jahnes, J. Hone, and S.J. Wind, J. Vac. Sci. Technol. B **26**, 2394 (2008).
[65] D. Metzler, C. Li, S. Engelmann, R.L. Bruce, E.A. Joseph, and G.S. Oehrlein, J. Chem. Phys. **146**, 052801 (2017).
[66] M. Wang and M.J. Kushner, J. Vac. Sci. Technol. A **29**, 051306 (2011).
[67] L. Ling, X. Hua, X. Li, G.S. Oehrlein, E.A. Hudson, P. Lazzeri, and M. Anderle, J. Vac. Sci. Technol. B **22**, 2594 (2004).
[68] N.R. Rueger, J.J. Beulens, M. Schaepkens, M.F. Doemling, J.M. Mirza, T.E.F.M. Standaert, and G.S. Oehrlein, J. Vac. Sci. Technol. A **15**, 1881 (1997).
[69] M. Schaepkens and G.S. Oehrlein, J. Electrochem. Soc. **148**, C211 (2001).
[70] K. Karahashi, H. Li, K. Yamada, T. Ito, S. Numazawa, K. Machida, K. Ishikawa, and S. Hamaguchi, Jpn. J. Appl. Phys. **56**, 06HB09 (2017).
[71] J. Tanaka, C.F. Abrams, and D.B. Graves, J. Vac. Sci. Technol. A **18**, 938 (2000).
[72] M. Schaepkens, T.E.F.M. Standaert, N.R. Rueger, P.G.M. Sebel, G.S. Oehrlein, and J.M. Cook, J. Vac. Sci. Technol. A **17**, 26 (1999).

[73] X. Li, X. Hua, L. Ling, G.S. Oehrlein, M. Barela, and H.M. Anderson, J. Vac. Sci. Technol. A **20**, 2052 (2002).
[74] D. Metzler, C. Li, S. Engelmann, R.L. Bruce, E.A. Joseph, and G.S. Oehrlein, J. Vac. Sci. Technol. A **34**, 01B101 (2016).
[75] M. Schaepkens, G.S. Oehrlein, C. Hedlund, L.B. Jonsson, and H.-O. Blom, J. Vac. Sci. Technol. A **16**, 3281 (1998).
[76] N.R. Rueger, M.F. Doemling, M. Schaepkens, J.J. Beulens, T.E.F.M. Standaert, and G.S. Oehrlein, J. Vac. Sci. Technol. A **17**, 2492 (1999).
[77] F. Gaboriau, M.C. Peignon, A. Barreau, G. Turban, C. Cardinaud, K. Pfeiffer, G. Bleidießel, and G. Grützner, Microelectron. Eng. **53**, 501 (2000).
[78] Y. Yin and H.H. Sawin, J. Vac. Sci. Technol. A **26**, 161 (2008).
[79] T.E.F.M. Standaert, C. Hedlund, E.A. Joseph, G.S. Oehrlein, and T.J. Dalton, J. Vac. Sci. Technol. A **22**, 53 (2004).
[80] C.M. Huard, S. Sriraman, A. Paterson, and M.J. Kushner, J. Vac. Sci. Technol. A **36**, 06B101 (2018).
[81] G. Cunge and J.P. Booth, J. Appl. Phys. **85**, 3952 (1999).
[82] O. Joubert, P. Czuprynski, and F.H. Bell, J. Vac. Sci. Technol. B **15**, 629 (1997).
[83] H. Shi, D. Shamiryan, J.F. de Marneffe, H. Huang, P.S. Ho, and M.R. Baklanov, Adv. Interconnects ULSI Technol. **041101**, 79 (2012).
[84] D.C. Marra and E.S. Aydil, J. Vac. Sci. Technol. A **15**, 2508 (1997).
[85] A. Ermolieff, S. Marthon, F. Bertin, F. Pierre, J.F. Daviet, and L. Peccoud, J. Vac. Sci. Technol. A **9**, 2900 (1991).
[86] P. Luan and G.S. Oehrlein, J. Phys. D. Appl. Phys. **51**, 135201 (2018).
[87] M.F. Doemling, N.R. Rueger, G.S. Oehrlein, and J.M. Cook, J. Vac. Sci. Technol. B **16**, 1998 (1998).
[88] Y.H. Ting, C.C. Liu, S.M. Park, H. Jiang, P.F. Nealey, and A.E. Wendt, Polymers (Basel). **2**, 649 (2010).
[89] B.J. Orf, S.G. Walton, D. Leonhardt, and G.S. Oehrlein, J. Vac. Sci. Technol. B **25**, 779 (2007).
[90] A. Agarwal and M.J. Kushner, J. Vac. Sci. Technol. A **27**, 37 (2009).
[91] P.J. Rae and D.M. Dattelbaum, Polymer (Guildf). **45**, 7615 (2004).
[92] DuPont, *Teflon PTFE Properties Handbook* (1996).
[93] S. Engelmann, R.L. Bruce, F. Weilnboeck, M. Sumiya, T. Kwon, R. Phaneuf, G.S. Oehrlein, C. Andes, D. Graves, D. Nest, and E.A. Hudson, J. Vac. Sci. Technol. B Microelectron. Nanom. Struct. **27**, 1165 (2009).
[94] K. Ishikawa, K. Karahashi, T. Ishijima, S. Il Cho, S. Elliott, D. Hausmann, D. Mocuta, A. Wilson, and K. Kinoshita, Jpn. J. Appl. Phys. **57**, 06JA01 (2018).
[95] N. Felix, D. Corliss, K. Petrillo, N. Saulnier, Y. Xu, L. Meli, H. Tang, A. De Silva, B. Hamieh, M. Burkhardt, Y. Mignot, R. Johnson, C. Robinson, M. Breton, I. Seshadri, D. Dunn, S. Sieg, E. Miller, G. Beique, A. Labonte, L. Sun, G. Han, E. Verduijn, E. Han, B.C. Kim, J. Kim, K. Hontake, L. Huli, C. Lemley, D. Hetzer, S. Kawakami, and K. Matsunaga, Extrem. Ultrav. Lithogr. VII **9776**, 97761O (2016).
[96] D. De Simone, A.M. Goethals, F. Van Roey, T. Zheng, P. Foubert, E. Hendrickx, G. Vandenberghe, and K. Ronse, J. Photopolym. Sci. Technol. **27**, 601 (2014).
[97] P. Naulleau, C. Anderson, W. Chao, S. Bhattarai, A. Neureuther, K. Cummings, S.H. Jen, M. Neisser, and B. Thomas, J. Photopolym. Sci. Technol. **27**, 725 (2015).

[98] L. Li, X. Liu, S. Pal, S. Wang, C.K. Ober, and E.P. Giannelis, Chem. Soc. Rev. **46**, 4855 (2017).
[99] C.K. Ober, V. Kosma, H. Xu, K. Sakai, and E.P. Giannelis, J. Photopolym. Sci. Technol. **31**, 261 (2018).
[100] C. Wagner and N. Harned, Nat. Photonics **4**, 24 (2010).
[101] P.P. Naulleau, C.N. Anderson, L.-M. Baclea-an, P. Denham, S. George, K.A. Goldberg, G. Jones, B. McClinton, R. Miyakawa, S. Rekawa, and N. Smith, in *Proc. SPIE 7972, Adv. Resist Mater. Process. Technol. XXVIII*, edited by R.D. Allen and M.H. Somervell (2011), p. 797202.
[102] A. Yen, H. Meiling, and J. Benschop, 2019 Electron Devices Technol. Manuf. Conf. EDTM 2019 475 (2019).
[103] D. Kawamura, Y. Tanaka, T. Itani, E. Soda, and N. Oda, Adv. Resist Mater. Process. Technol. XXVI **7273**, 72731O (2009).
[104] D.L. Goldfarb, R.L. Bruce, J.J. Bucchignano, D.P. Klaus, M.A. Guillorn, and C.J. Wu, Extrem. Ultrav. Lithogr. III **8322**, 832205 (2012).
[105] A. Liang, J. Hermans, T. Tran, K. Viatkina, C.-W. Liang, B. Ward, S. Chuang, J. Yu, G. Harm, J. Vandereyken, D. Rio, M. Kubis, S. Tan, R. Wise, M. Dusa, S. Reddy, A. Singhal, B. van Schravendijk, G. Dixit, and N. Shamma, Extrem. Ultrav. Lithogr. VIII **10143**, 1014319 (2017).
[106] S.D. Athavale and D.J. Economou, J. Vac. Sci. Technol. B **14**, 3702 (1996).
[107] S. Rauf, T. Sparks, P.L.G. Ventzek, V. V. Smirnov, A. V. Stengach, K.G. Gaynullin, and V.A. Pavlovsky, J. Appl. Phys. **101**, 033308 (2007).
[108] S. Salahuddin, K. Ni, and S. Datta, Nat. Electron. **1**, 442 (2018).
[109] K. Ishikawa, K. Karahashi, T. Ishijima, S. Il Cho, S. Elliott, D. Hausmann, D. Mocuta, A. Wilson, and K. Kinoshita, Jpn. J. Appl. Phys. **57**, (2018).
[110] P. Luan and G.S. Oehrlein, Langmuir **35**, 4270 (2019).
[111] A. Pranda, S.A. Gutierrez Razo, J.T. Fourkas, and G.S. Oehrlein, Plasma Process. Polym. **16**, e1900026 (2019).
[112] K.J. Kanarik, T. Lill, E.A. Hudson, S. Sriraman, S. Tan, J. Marks, V. Vahedi, and R.A. Gottscho, J. Vac. Sci. Technol. A Vacuum, Surfaces, Film. **33**, 020802 (2015).
[113] M. Kawakami, D. Metzler, C. Li, and G.S. Oehrlein, J. Vac. Sci. Technol. A Vacuum, Surfaces, Film. **34**, 040603 (2016).
[114] V. Rastogi, G. Beique, L. Sun, H. Cottle, Y. Feurprier, A. Metz, K. Kumar, C. Labelle, J. Arnold, M. Colburn, and A. Ranjan, Adv. Etch Technol. Nanopatterning V **9782**, 97820B (2016).
[115] K.J. Kanarik, S. Tan, and R.A. Gottscho, J. Phys. Chem. Lett. **9**, 4814 (2018).
[116] L.J. Bellamy, *The Infrared Spectra of Complex Molecules* (Springer, 1980).
[117] M. Fouchier, E. Pargon, L. Azarnouche, K. Menguelti, O. Joubert, T. Cardolaccia, and Y.C. Bae, Appl. Phys. A Mater. Sci. Process. **105**, 399 (2011).
[118] J. Mohammed Nasrullah, S. Raja, K. Vijayakumaran, and R. Dhamodharan, J. Polym. Sci. Part A Polym. Chem. **38**, 453 (2000).
[119] A. Doucouré, C. Guizard, J. Durand, R. Berjoan, and L. Cot, J. Memb. Sci. **117**, 143 (1996).
[120] S. Agraharam, D.W. Hess, P.A. Kohl, and S.A. Bidstrup Allen, J. Vac. Sci. Technol. A Vacuum, Surfaces, Film. **17**, 3265 (1999).
[121] B. Scheiner, S.D. Baalrud, B.T. Yee, M.M. Hopkins, and E.V. Barnat, Phys.

Plasmas **22**, 123520 (2015).
[122] R.A. Gottscho, J. Vac. Sci. Technol. B Microelectron. Nanom. Struct. **10**, 2133 (1992).
[123] D.P. Lymberopoulos and D.J. Economou, J. Vac. Sci. Technol. A Vacuum, Surfaces, Film. **12**, 1229 (1994).
[124] H.G. Hughes and M.J. Rand, *Etching for Pattern Definition: Proceedings of the Symposium, Washington, D.C., 1976* (Books on Demand, Washington D.C., 1976).
[125] S. Hwang and K.J. Kanarik, Semicond. Dig. (2016).
[126] N. Fox-Lyon, A.J. Knoll, J. Franek, V. Demidov, V. Godyak, M. Koepke, and G.S. Oehrlein, J. Phys. D. Appl. Phys. **46**, 485202 (2013).
[127] V.I. Merkulov, A. V. Melechko, M.A. Guillorn, M.L. Simpson, D.H. Lowndes, J.H. Whealton, and R.J. Raridon, Appl. Phys. Lett. **80**, 4816 (2002).
[128] S. Habenicht, W. Bolse, K.P. Lieb, K. Reimann, and U. Geyer, Phys. Rev. B - Condens. Matter Mater. Phys. **60**, R2200(R) (1999).
[129] I. Koponen, M. Hautala, and O.P. Sievänen, Phys. Rev. Lett. **78**, 2612 (1997).
[130] R.M. Bradley and J.M.E. Harper, J. Vac. Sci. Technol. A Vacuum, Surfaces, Film. **6**, 2390 (1988).
[131] J. Erlebacher, M.J. Aziz, E. Chason, M.B. Sinclair, and J.A. Floro, Phys. Rev. Lett. **82**, 2330 (1999).
[132] E. Pargon, D. Nest, and D.B. Graves, J. Vac. Sci. Technol. B Microelectron. Nanom. Struct. **25**, 1236 (2007).
[133] F. Frost, B. Ziberi, A. Schindler, and B. Rauschenbach, Appl. Phys. A Mater. Sci. Process. **91**, 551 (2008).
[134] Y.S. Katharria, S. Kumar, P.S. Lakshmy, D. Kanjilal, and A.T. Sharma, J. Appl. Phys. **102**, 044301 (2007).
[135] M. Goyal, S. Aggarwal, A. Sharma, and S. Ojha, Appl. Surf. Sci. **439**, 380 (2018).
[136] T.D.B.B. Jacobs, T. Junge, and L. Pastewka, Surf. Topogr. Metrol. Prop. **5**, 013001 (2017).
[137] D. Nečas and P. Klapetek, Cent. Eur. J. Phys. **10**, 181 (2012).
[138] Y. Zhang, M.J. Kushner, S. Sriraman, A. Marakhtanov, J. Holland, and A. Paterson, J. Vac. Sci. Technol. A Vacuum, Surfaces, Film. **33**, 031302 (2015).
[139] J. Muñoz-García, M. Castro, and R. Cuerno, Phys. Rev. Lett. **96**, 1 (2006).
[140] M. Goyal, S. Aggarwal, and A. Sharma, J. Appl. Phys. **119**, 115303 (2016).
[141] D.P. Datta, S.K. Garg, T. Basu, B. Satpati, H. Hofsäss, D. Kanjilal, and T. Som, Appl. Surf. Sci. **360**, 131 (2016).
[142] M. Omura, J. Hashimoto, T. Adachi, Y. Kondo, M. Ishikawa, J. Abe, I. Sakai, H. Hayashi, M. Sekine, and M. Hori, Jpn. J. Appl. Phys. **58**, SEEB02 (2019).
[143] R. Kumari, D. Gupta, R. Singhal, A. Sharma, and S. Aggarwal, J. Appl. Phys. **126**, 155303 (2019).
[144] M. Goyal, D. Gupta, S. Aggarwal, and A. Sharma, J. Phys. Condens. Matter **30**, 284002 (2018).
[145] T.E.F.M. Standaert, P.J. Matsuo, X. Li, G.S. Oehrlein, T.-M. Lu, R. Gutmann, C.T. Rosenmayer, J.W. Bartz, J.G. Langan, and W.R. Entley, J. Vac. Sci. Technol. A Vacuum, Surfaces, Film. **19**, 435 (2001).